

THE MICROENVIRONMENTAL IMPACT OF ROADWAYS AND  
DISTRIBUTED GENERATION ON LOCAL AIR QUALITY

A Dissertation

Presented to the Faculty of the Graduate School

of Cornell University

In Partial Fulfillment of the Requirements for the Degree of

Doctor of Philosophy

by

Zheming Tong

August 2015

© 2015 Zheming Tong

# THE MICROENVIRONMENTAL IMPACT OF ROADWAYS AND DISTRIBUTED GENERATION ON LOCAL AIR QUALITY

Zheming Tong, Ph. D.

Cornell University 2015

Microscale air quality in highly populated urban areas has gained increasing attention in recent years. Various emission sources are present, and their contributions need to be quantified for assessing human exposure and developing effective emission control strategies. This dissertation presents the effort towards establishing a better understanding of the spatial variation of multiple air pollutants in complex urban microenvironments through numerical modeling and experimental evaluation. In the first part, I investigated the transport of Black Carbon (BC) in a typical highway-building environment next to an urban high school in South Bronx, NYC. Two generalized configurations i.e., highway-building canyon and highway viaduct-building are discovered, which is critical to the spatial variation of BC. The second part focuses on roadside barrier designs with the objective to mitigate near-road air pollution. Our analysis revealed two potentially viable design options: a) wide vegetation barriers with high leaf area density which reduces downwind particle concentrations significantly, while resulting in a moderate increase in on-road concentrations, and b) vegetation-solid barrier combinations lead to the greatest reduction in downwind particle concentrations among all configurations and a large increase in on-road concentrations at the same time. The third part investigates the

near-source environmental impact of diesel backup generators that participate in demand response programs. The micro-environmental air quality simulation is improved by coupling with a meteorology processor to provide realistic boundary conditions. The study found the near-ground  $\text{PM}_{2.5}$  concentration for the worst scenarios could well exceed  $100 \mu\text{g m}^{-3}$ , posing a potential health risk to people living and working nearby. Our analysis also implies that the siting of diesel backup generators stacks should consider not only the interactions of fresh air intake and exhaust outlet, but also the dispersion of exhaust plumes in the surrounding environment. The last part studies the environmental impact of a biomass boiler with and without PM emission control. A micro-environmental model was applied to simulate the experimental conditions, and a good agreement between predicted and on-site measurement is observed. Our analysis shows that the absence of ESP could lead to an almost 7 times increase of the near-ground  $\text{PM}_{2.5}$  concentrations in the surrounding environment.

## BIOGRAPHICAL SKETCH

Zheming received his B.S. in Mechanical Engineering from University of Wisconsin-Madison in May 2010. He was a member of Pi Tau Sigma Honor Society and his undergraduate research focused on the development of computational heat transfer model for a Sub-Kelvin cryogenic cooler. He then joined the Sibley School of Mechanical and Aerospace Engineering at Cornell University in pursuit of his Ph.D. in August 2010. While there, he started working with Prof. K. Max Zhang at the Energy and the Environment Research Laboratory (EERL). Zheming's research at Cornell mainly targets on quantifying the environmental impact of various emission sources in complex urban microenvironments. In addition, Zheming completed two internships with Schlumberger-Doll Research where he developed programs to simulate proppant transport in complex fracture network and pressure wave propagation in drill pipes. After graduation, he will be a postdoctoral fellow at the Harvard University Graduate School of Design.

Dedicated to My Parents

## ACKNOWLEDGMENTS

I would like to sincerely thank my Ph.D. advisor, Prof. K. Max Zhang, whose expertise, understanding, and patience, added considerably to my graduate experience. I appreciate his vast knowledge and skill in many areas, and his constant assistance in writing technical papers. I'm also grateful for Professor Edwin Cowen, Professor Tom Whitlow, and Professor Ying Hua for their insightful suggestions and guidance to my PhD study and serving in my special committee. I appreciate my colleagues in the Energy and the Environment Research Laboratory for their help in my research: Dr. Yan Wang, Dr. Bo Yang, and Dr. Jonathan Steffens. Finally, and most importantly, I would like to thank my parents in China, for their love, encouragement and support.

## TABLE OF CONTENTS

Chapter 1: Introduction.....	1
Chapter 2: Modeling Spatial Variations of Black Carbon Particles in an Urban Highway-Building Environment .....	5
Abstract.....	5
2.1. Introduction.....	6
2.2. BC Properties, Field Measurements and Simulated Cases .....	8
2.3. Modeling Method .....	10
2.3.1 Modeling Domain .....	11
2.3.2 Boundary conditions .....	11
2.3.3 BC Emission Rate and Emission Zone Modeling.....	13
2.3.4 Background BC Concentrations.....	15
2.4. Results.....	15
2.4.1 Model Evaluation .....	15
2.4.2 Characterizations of the Highway-Building Environment.....	19
2.5. Implication .....	26
Chapter 3: Roadside Vegetation Barrier Designs to Mitigate Near-Road Air Pollution Impacts .....	28
Abstract.....	28
3.1. Introduction.....	29
3.2. Numerical Method .....	30
3.2.1 Spatial Averaging of Vegetation .....	31
3.2.2 Large Eddy Simulation (LES).....	31
3.2.3 Particle Dispersion and Deposition .....	33
3.3. Model Evaluation.....	34
3.3.1 Chapel Hill Field Experiment .....	34
3.3.2 Boundary Conditions .....	35
3.3.3 Simulation Results .....	35
3.4. Evaluation of Vegetation Barrier Design Configurations.....	36

3.4.1 Barrier Configurations .....	36
3.4.2 Boundary Conditions .....	38
3.4.3 Results and Discussion.....	39
3.4.3.1 Case 1 .....	39
3.4.3.2 Case 2, 3 and 4 .....	41
3.4.3.3 Case 5 .....	43
3.4.3.4 Sensitivity Study on Case 1.....	43
3.5. Conclusion .....	48
Chapter 4: The Near-Source Impacts of Diesel Backup Generators in Urban Environments.....	50
Abstract.....	50
4.1. Introduction.....	51
4.2. Model Description .....	55
4.2.1 Governing Equation .....	56
4.3. Model Evaluations .....	58
4.3.1 ERCOFTAC.....	58
4.3.1.1 Experiment .....	58
4.3.1.2 Simulation .....	59
4.3.1.3 Results .....	60
4.3.2 Plume Dispersion .....	61
4.3.2.1 Experiment .....	61
4.3.2.2 Simulation .....	62
4.3.2.3 Results.....	63
4.4. Diesel Backup Generator Case Studies .....	64
4.4.1 Numerical Setup.....	64
4.4.2 Stack Parameters .....	69
4.4.3 Results and Discussions .....	71
4.5. Conclusion .....	77
Chapter 5: Micro-environmental Air Quality Impacts of a Biomass Boiler With and Without PM Emission Control .....	79
Abstract.....	79

5.1. Introduction.....	80
5.2. Experimental Approach .....	81
5.2.1 Site Description .....	81
5.2.2 Instrumentation .....	82
5.2.3 Sampling Location .....	82
5.3. Numerical Setup .....	83
5.3.1 Stack Parameters .....	85
5.3.2 Fuel-based Emission Factor .....	86
5.3.3 Uncertainties .....	87
5.4. Results.....	88
5.4.1 Model Evaluation .....	88
5.4.2. With and Without Emission Control.....	91
5.4.3 Ambient Wind Speed .....	92
5.4.4 Stack Temperature .....	93
5.4.5 Removing Carrier Dome .....	94
5.5. Conclusion .....	95
Chapter 6: Major Contribution .....	97
BIBLIOGRAPHY .....	102

## LIST OF FIGURES

Figure 1.1: Schematics of a typical microenvironment with roadway, building, vegetation barrier and distributed generation .....	1
Figure 2.1: Sketch of the modeling domain. Encircled are close views of the transition portions of the highway configuration. There are two declining ramps, which are solid embankments, at both ends of I-87 in the modeling domain. The middle portion of I-87 is also elevated but with open space underneath, referred to as a highway viaduct..	8
Figure 2.2: a) Simulated Vs. Measured Wind Speed b) Simulated Vs. Measured Wind Direction c) Simulated Vs. Measured BC Concentration. ....	19
Figure 2.3: Flow field between highway and urban school (U2) varies with wind direction. <i>Highway-Building Canyon</i> conditions (a) occur mostly between solid highway embankment and U2, and <i>Highway Viaduct-Building</i> conditions (b) occur mostly between viaduct (middle section of highway shown in Figure 2.1 with open space underneath) and U2. ....	21
Figure 2.4: Simulated vertical BC Concentration as a function of distance away from the edge of the highway for a) highway-building canyon and b) highway viaduct-building conditions. Only highway emission source is considered. BC concentration is normalized by the concentration at the edge of highway, and vertical height is normalized by the elevation of the highway modeled. Wind direction is 225° for a) and 292.5° for b).....	23
Figure 2.5: Simulated normalized vertical BC profiles at the front gate of the urban school (U2) under the transitional condition with a) Increasing aspect ratio H/W (Increasing the height of U2 from a baseline of 15m to 25m, 35m, and 45m.) and b) Decreasing aspect ratio H/W (Translate U2 further horizontally from a baseline of 30 m away from highway to 40m, 50m, and 60m). All simulations are under the ambient wind direction of 270°. BC concentration is normalized by the concentration at the edge of highway, and the vertical height is normalized by the elevation of the highway modeled. ....	23
Figure 3.1: Particle size distribution (PSD) for three modeling scenarios (Morning, Peak1, Peak2). “LES Barrier” stands for simulation results by Large Eddy Simulation (LES). “No-barrier” stands for experimental result at the no-barrier site. “Exp Barrier” stands for the experimental result behind the barrier. ....	36
Figure 3.2: Schematics of six roadside barrier configurations. In the simulation, the complex geometry of the vegetation canopy is modeled as rectangular blocks. Leaf Area Density (LAD) profiles of coniferous trees are applied on each block to represent the real geometry of coniferous evergreen. ....	37
Figure 3.3: Schematics of the baseline configuration (Case 1) .....	39
Figure 3.4: a) Horizontal gradients of size-resolved particle concentrations from 15nm to 253nm. 9 particle sizes are simulated, but 6 bins are plotted for clarity. $\chi$ is the particle concentration normalized by the peak concentration from the no-barrier case at the same particle size. The vertical dash line separates the on-road and near-road domains. The green strip indicates the location and width of the vegetation barrier. b) Particle size distribution (PSD) of the baseline; dash lines represent the no-barrier	

case. ....	39
Figure 3.5: a) Illustration of Mass Balance Analysis for 180 nm particle b) Normalized concentration decline over distance. Dash line stands for the with-barrier case. Solid line indicates the no-barrier case .....	41
Figure 3.6: Horizontal gradients of size-resolved particle concentrations for Cases 2 (a), 3 (b) and 4 (c). The green strip indicates the location and width of the vegetation barrier. The grey strip indicates the location and width of the solid barrier. The strips with green on both sides designate the location and width of a “green wall” .....	42
Figure 3.7: a) Horizontal gradients size-resolved particle concentrations; b) PSD for Case 5; The green area indicates the location and width of the vegetation barrier. ....	43
Figure 3.7: PSDs with increasing LAD a) baseline LAD b) +50% LAD c) solid barrier. ....	44
Figure 3.8: Horizontal gradients of Case 1 with a) 6m b) 12m c) 18m vegetation barrier .....	44
Figure 3.9: Horizontal gradients under three atmospheric stability conditions a) unstable, b) neutral, and c) stable. A no-barrier case for the unstable condition is shown by black dash lines for comparison. 9 particle sizes are simulated, but 5 bins are plotted for clarity. ....	46
Figure 3.10: Horizontal gradients for a) 50%, b) 100%, and c) 200% of the baseline wind speed profiles. Horizontal gradients are normalized by the concentration of the no-barrier case at the same wind speed as comparison. 9 particle sizes are simulated, but 6 bins are plotted for clarity. The green strip indicates the location and width of the vegetation barrier.....	46
Figure 3.11: Horizontal gradients of three oncoming wind directions: 30, 45, 90 degrees. Wind direction of 90 degree is normal to the roadway. ....	47
Figure 4.1: a) Schematic of the numerical setup for flow field evaluation b) Schematic of numerical setup for the plume dispersion evaluation. SH1(Stack Height) =75mm, SH2=150mm, SH3=225mm, SH4=300 mm. H is defined as the height of the cube. ...	59
Figure 4.2: Time-averaged streamwise velocity profile at various x/H as indicated ...	60
Figure 4.3: Streamwise velocity profile on the symmetry plane at two heights z/H=0.5, 0.9. ....	61
Figure 4.4: Schematics of the building used in the plume dispersion experiment. Left: 15 cm building; Right: 60 cm building.....	62
Figure 4.5: a) Normalized ground-level centerline concentration ( $\chi$ ) for 15cm building at SH=75, 150, 225, 300 mm; b) Normalized ground-level centerline concentration ( $\chi$ ) for 60cm building at SH=75, 150, 225, 300 mm.....	63
Figure 4.6: a) Geometry of the diesel backup generator site, b) Cut plane that intersects the stack and parallel to xz plane. Vertical lines that are 30, 100, 300, 500m downwind from the stack are shown. ....	69
Figure 4.7: a) Vertical profiles of NOx concentration of backup diesel generator in ppmv b) Vertical profiles of PM <sup>2.5</sup> concentration of backup diesel generator in $\mu\text{g}/\text{m}^3$ at 30m, 100m, 300m, and 500m away from the stack.....	71
Figure 4.8: Schematics of 4 configurations and corresponding contour plots of primary PM <sub>2.5</sub> concentration in $\mu\text{g m}^{-3}$ . Case A is the baseline configuration. ....	72
Figure 4.9: Contour plots of PM <sub>2.5</sub> concentration in $\mu\text{g}/\text{m}^3$ for Case C.....	74

Figure 4.10: Contour plots of primary PM <sub>2.5</sub> concentration in µg/m <sup>3</sup> for three exhaust momentum ratio M (=stack exit velocity /ambient wind velocity) indicated. Stack exit velocity is kept constant for three cases. M=3.8 from Case C is employed as a new baseline for comparison. Ambient wind velocity for the M=7.6 case is 2 m s <sup>-1</sup> , and 8 m s <sup>-1</sup> for the M=1.9 case. ....	75
Figure 4.11: Primary PM <sub>2.5</sub> concentration contour plots (µg m <sup>-3</sup> ) of Case C for a) 1000 kW diesel backup generator b) 500 kW diesel backup generator .....	76
Figure 4.12: Contour plot of a) NO <sub>x</sub> concentration in ppmv and b) PM <sub>2.5</sub> concentration µg m <sup>-3</sup> based on Tier 4 standards based a 1000 kW diesel backup generator .....	77
Figure 5.1: Satellite image of the site overlaid with flow field and air quality sampling details. The position of triangles indicates the relative position of each sampling stations. ....	81
Figure 5.2: a) Satellite image of the Modeling area b) The corresponding geometry generated for simulation .....	84
Figure 5.3: a, b, c ) Synchronized spikes observed on the Illick station; d, e, f) spikes observed on the Carrier Dome station. ....	89
Figure 5.4: Comparison between simulated and measured wind speed and direction. a and b are under the boundary condition where wind is from the West to Illick Hall. c and d are under the boundary condition where the wind is from the South to the Dome. Error bars of the total measurement error are added on each data point. ....	90
Figure 5.5: Comparison between simulated and measured PM <sub>2.5</sub> concentration. Error bars (fixed error only) are applied on the measurement data. However, they may not seem visible as the error range is small. ....	91
Figure 5.6: A comparison of the PM <sub>2.5</sub> concentration [µg m <sup>-3</sup> ] contour plot (side and top views) in the surrounding environment with and without ESP .....	92
Figure 5.7: Contour plot of the PM <sub>2.5</sub> concentration in side view at three ambient wind speeds. u is the baseline wind speed at 2 m/s. ....	93
Figure 5.8: Contour plot of the PM <sub>2.5</sub> concentration [µg m <sup>-3</sup> ] at three stack temperatures. ....	94
Figure 5.9: Contour plot of the PM <sub>2.5</sub> concentration [µg m <sup>-3</sup> ] with and without Carrier Dome in side and top views.....	95

## LIST OF TABLE

Table 2.1: Summary of performance metrics for model evaluation.....	10
Table 3.1: Description of roadside barrier geometry for all configurations tested.....	38
Table 4.1: Stack, meteorology, and building parameters for a 1000 kW diesel backup generator at steady-state operation .....	70
Table 5.1: Stack Parameters .....	86
Table 5.2: Fixed and random error for different sampling instruments. The range of random error for the sonic anemometers is listed. ....	88

# Chapter 1

## Introduction

Many epidemiologic studies have shown that people who live, work, or go to school near various emission sources are at risk for a number of health problems, including respiratory and cardiovascular problems, birth and developmental defects, and cancer (HEI, 2010). Recently, microscale air quality issues in highly populated urban areas have gained increasing attention in recent years. Roadways, roadside structures, and distributed generation (DGs) are often located in highly populated areas as shown in Figure 1.1. Their environmental impact need to be quantified for assessing human exposure and developing effective emission control strategies. Therefore, identifying effective methods to reduce exposures to air pollution has become a public health priority, especially in developing countries.



Figure 1.1: Schematics of a typical microenvironment with roadway, building, vegetation barrier and distributed generation

There is a growing interest in how roadside structures impact the near-road air quality in microenvironments due to the large population who live or spend long periods of time in such environment (Baldauf et al., 2008). In the past, many near-road air quality studies have characterized open highway conditions, i.e., large roads without any major structures in the close vicinity (Wang and Zhang, 2009a; Wang et al., 2011b; Wang and Zhang, 2011). However, the presence of buildings near highways, referred to here as the highway-building environment, is common in urban areas and not investigated yet. In such environment, roadway configuration and building geometry both affect the pollutant dispersion, which differs from a street canyon environment, where buildings dominate the overall flow (Tong et al., 2012). In chapter 2, a computational fluid dynamics (CFD)-based air quality model was developed to simulate the transport of Black Carbon (BC) from Highway I-87 next to an urban school in South Bronx, NYC. The general strategy for all the following numerical studies is to evaluate the model performance with on-site measurement first. In doing so, we hope to gain confidence in our simulation approach. Then, we deepen our understanding by running a number of simulations with various physical parameters. Based on our numerical simulations, we investigated how highway configurations and buildings affect the spatial variation of BC concentrations, and discussed the implications of our study in terms of human exposure assessment and highway design.

Roadside barrier is also a prevalent roadway features. Researchers have shown its potential to reduce near-road air pollutant concentration (Bowker et al., 2007; Baldauf et al., 2008; Hagler et al., 2011; Steffens et al., 2012; Steffens et al., 2013; Steffens et al., 2014). However, the characteristics of these barriers needed to ensure

pollution reductions are not well understood. Therefore, in chapter 3, I explored the effects of eight conceptual roadside vegetation/solid barrier configurations on near-road size-resolved particle concentrations, governed by dispersion and deposition.

In addition to roadways, small distributed power generation (DG), e.g., diesel generator, biomass boiler, gas turbine, is becoming more popular due its flexibility and efficiency compared with central power generation (Pepermans et al., 2005). These units are typically located in populated urban areas with relatively short stack heights. Since they are closer to consumers, their environmental impacts have become a concern despite the benefits. Several studies have evaluated the air quality impact from distributed generation (Greene and Hammerschlag, 2000; Heath et al., 2006; Strachan and Farrell, 2006; Carreras-Sospedra et al., 2010; Jing and Venkatram, 2011). However, very few studies have examined the effects of complex urban environments such as street canyons on the near-source air quality impacts. In the next part of the dissertation, my goal is to bridge this knowledge gap by developing site-specific CFD-based models and on-site field study. In chapter 4, I focused on diesel backup generators, often referred as “standby generators” or “emergency generators”. Their primary purpose is to preserve essential facility functions in the event of a loss of grid power or for situations that threaten the facility, such as fire pump use during a fire (NESCAUM, 2012). Those generators can also operate during periods of peak electricity demand, increasing grid reliability and supporting the electricity delivery systems (Gilmore et al., 2006). The objective of this study is to first introduce an improved approach to simulate spatial variations of pollutants in a near-source urban microenvironment by employing a meteorology processor AERMET to generate site-

specific boundary layer parameters as boundary conditions (USEPA, 2004a). The second objective is to evaluate the environmental impact of diesel backup generators in near-source microenvironments. In chapter 5, I investigated the micro-environmental air quality impact of a biomass-fueled combined heat and power system equipped with an electrostatic precipitator (ESP) in Syracuse, NY. This study combines both field experiment and numerical simulation. The model performance was evaluated against on-site aerodynamic and air quality measurement. We then applied the model to assess the nearby air quality with and without ESP, and the siting of the exhaust stack.

## Chapter 2

### **Modeling spatial variations of black carbon particles in an urban highway-building environment**

#### **Abstract**

Highway-building environments are prevalent in metropolitan areas. This paper presents our findings in investigating pollutant transport in a highway-building environment by combining field measurement and numerical simulations. We employ and improve the Comprehensive Turbulent Aerosol Dynamics and Gas Chemistry (CTAG) model to simulate the spatial variations of black carbon (BC) concentrations near highway I-87 and an urban school in the South Bronx, New York. The results of CTAG simulations are evaluated against and agree adequately with the measurements of wind speed, wind directions and BC concentrations. Our analysis suggests that the BC concentration at the measurement point of the urban school could decrease by 43-54% if roadside buildings were absent. Furthermore, we characterize two generalized conditions in a highway-building environment, i.e., *highway-building canyon* and *highway viaduct-building*. The former refers to the canyon between solid highway embankment and roadside buildings, where the spatial profiles of BC depend on the equivalent canyon aspect ratio and flow recirculation. The latter refers to the area between a highway viaduct (i.e., elevated highway with open space underneath) and roadside buildings, where strong flow recirculation is absent and the spatial profiles of

BC are determined by the relative heights of the highway and buildings. The two configurations may occur at different locations or in the same location with different wind directions when highway geometry is complex. Our study demonstrates the importance of incorporating highway-building interaction into the assessment of human exposure to near-road air pollution. It also calls for active roles of building and highway designs in mitigating near-road exposure of urban population.

## **2.1. Introduction**

In recent years, epidemiological and toxicological studies worldwide have suggested an association between human exposure to traffic-related air pollutants and a range of adverse respiratory and cardiovascular health effects (HEI, 2010). Many near-road air quality studies have characterized open highway conditions, i.e., large roads without any major structures in the close vicinity (Wang and Zhang, 2009a; Wang et al., 2011b; Wang and Zhang, 2011). Nevertheless, the presence of buildings near highways, referred to here as the highway-building environment, is common in urban areas. In a highway-building environment, roadway configuration and building geometry both affect the flow, which differs from a street canyon environment, where buildings dominate the overall flow.

Thus, in order to accurately assess human exposure to traffic-related air pollutants in the highway-building environments, we need to address the following two questions: 1) How do buildings affect the transport and transformation of traffic-related air pollutants near roadways? And 2) What are the horizontal and vertical profiles of traffic-related air pollutants near building surfaces? This paper represents

the first effort to answer those two questions. We applied and improved the Comprehensive Turbulent Aerosol Dynamics and Gas Chemistry (CTAG) model to simulate the spatial variation of near-road black carbon (BC) concentration in a highway-building environment near highway I-87 in the South Bronx, NY, and compared the modeling results with the measurements conducted by Patel and coworkers in 2004 (Patel et al., 2009).

Among the five boroughs of NYC, the Bronx has ranked highest in both asthma hospitalizations and deaths in recent years. Between 1990 and 2000, the asthma rates decreased only 3% in the Bronx, as compared to 39% and 35% reduction in Brooklyn and Manhattan during the same period according to New York City Department of Health and Mental Hygiene (Garg et al., 2003). Although the origin of asthma is multi-factorial, recent studies link asthma to exposure to diesel particulate matter from heavy-duty diesel traffic in the area (Patel et al., 2010; Spira-Cohen et al., 2010; Spira-Cohen et al., 2011). It is estimated that 66% of the population in the Bronx is living within 150m of major roads, including interstate, state, and county highways, access ramps, and arterials, and 91% within 300m (NYSERDA, 2008). BC particles are not only a tracer of diesel traffic, but are also associated with cardiopulmonary health effects (Jansen et al., 2005; Mordukhovich et al., 2009; Wang et al., 2009; Westerdahl et al., 2009). As BC particles cause a direct positive radiative acting as a short lived climate forcer, control measures of particulate matter (PM) emissions that lead to reduction of the BC component will likely have a positive impact on human health, resulting in a co-benefit of PM reductions.

This paper is organized as follows. We start with a description of our numerical

modeling approach, followed by a brief introduction of the field measurement. Then, we compare the predicted and measured wind speed, wind direction, and BC concentrations at the sampling site. Next, we elaborate on how highway configurations and buildings affect the spatial variation of BC concentrations based on our numerical simulations. Finally, we discuss the implications of our study in terms of human exposure assessment and highway design.

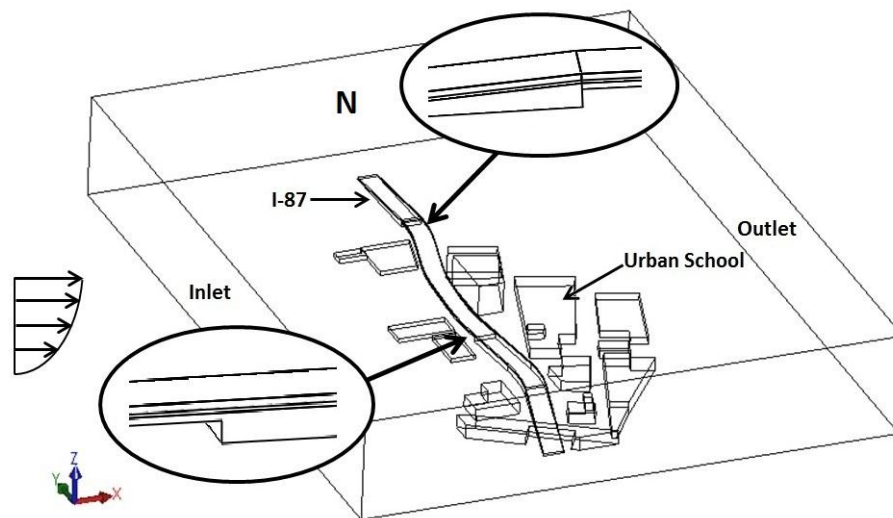


Figure 2.1: Sketch of the modeling domain. Encircled are close views of the transition portions of the highway configuration. There are two declining ramps, which are solid embankments, at both ends of I-87 in the modeling domain. The middle portion of I-87 is also elevated but with open space underneath, referred to as a highway viaduct.

## 2.2. BC Properties, Field Measurements and Simulated Cases

In this study, black carbon is defined as the primary constituent of  $PM_{2.5}$  that is responsible for light absorption of particles in the atmosphere (Horvath, 1993). We model BC particles as inert species, which experiences no chemical transformation within the timescale of concern (seconds to minutes). Because most BC occurs as sub-

micron particles, they are expected to adopt the flow velocity very quickly (i.e., with small Stokes number), it is reasonable to assume that they will disperse like gaseous species. Due to their relatively low concentrations, we further assume that BC particles do not affect the turbulent flow in the atmosphere (Gerashchenko et al., 2011).

A detailed description of the field measurements was provided by Patel and coworkers (Patel et al., 2009). A brief summary is presented here. The field measurements were conducted in an urban school, referred as U2, in the South Bronx, from February to March, 2004. U2 is located approximately 30m east of I-87, a highway with annual average daily traffic of 85,000 vehicles. BC concentrations were collected using a dual-beam Aethalometer (Model AE-21, Magee Scientific, Berkeley, CA) operated at 4 LPM and using a size selective cyclone for PM<sub>2.5</sub> (KTL cyclone, BGI, Waltham, MA). The unit was placed in an empty classroom with the sampling inlet located 0.9 m outside from the school wall, and the sampling inlet was protected from rain with a stainless steel rainhat. Thus the BC concentrations were measured at a fixed height and a fixed distance from I-87. A weather station (Vantage Pro Model 6150C, Davis Instrument Corp., Hayward, CA) was installed on the school rooftop to monitor and record temperature, relative humidity, barometric pressure, wind speed and direction, and precipitation. At U2, traffic data were collected using a video camera adjacent to highway. Vehicles counts were obtained manually by watching daytime videos. Two categories of vehicles are counted: Category I, mostly gasoline powered vehicles including passenger cars, vans, sport utility vehicles, pick-up trucks, and small double-axle trucks; and Category II, primarily diesel powered vehicles including large trucks with more than two axles, and buses.

As we are primarily interested in the effects of highway pollution on the nearby environment, we focus only on conditions with wind blowing from I-87 to the U2 site, i.e., with wind direction varying from south southwest (SSW or 202.5°) to north northwest (NNW or 337.5°), which accounts for 53% of the wind directions over the sampling month. For the I-87 segment next to U2, some portion is elevated with solid embankment, while the other portion is elevated with open space (Figure 2.1). This complex geometry, combined with different wind directions, leads to distinctly different spatial distributions of BC in this highway-building environment (discussed in Section 4.2). As the measured BC concentrations are only available as hourly-averaged data, we selected 34 cases with stable wind and traffic conditions, modeled using steady-state simulations. These 34 cases represent different hours from 6 am to 4 pm between March 12<sup>th</sup> and 22<sup>nd</sup>, 2004, among which 14 cases were during morning rush hours.

Table 2.1: Summary of performance metrics for model evaluation

Statistical Methods	Highway viaduct-building <sup>a</sup>			Highway-building canyon <sup>b</sup>			Transitional condition <sup>c</sup>		
	Wind Speed	Wind Direction	BC	Wind Speed	Wind Direction	BC	Wind Speed	Wind Direction	BC
Mean Normalized Error (MNE)	9.99%	4.12%	21.24%	9.79%	4.30%	16.83%	7.42%	4.90%	16.44%
Mean Normalized Bias (MNB)	8.19%	1.54%	-16.44%	3.09%	3.53%	-8.20%	-4.72%	1.24%	-12.25%
Mean Fraction Error (MFE)	7.62%	2.65%	15.87%	6.80%	2.77%	11.77%	5.40%	3.17%	12.08%
Mean Fraction (MFB)	6.47%	0.90%	-14.08%	2.70%	2.24%	-6.46%	-3.66%	0.67%	-9.38%

<sup>a</sup>: 15 cases; <sup>b</sup>: 13 cases; <sup>c</sup>: 6 cases out of total 34 cases.

### 2.3. Modeling Method

The CTAG model simulates the transport and transformation of exhaust particles from points of emissions to ambient background (Wang and Zhang, 2009a;

Wang et al., 2011b; Wang and Zhang, 2011). The transport portion of the CTAG model is called CFD-VIT-RIT, which has been applied to study the effects of highway configuration on near-road air quality under the open highway conditions. VIT stands for vehicle induced turbulence, and RIT stands for road induced turbulence (Wang and Zhang, 2009a). In this study, we expand the capability of CFD-VIT-RIT to simulate near-road air quality in highway-building environments. *ANSYS FLUENT 12.1* is employed as a turbulence solver for the CTAG model. We compared several turbulence models including standard k-epsilon, RNG k-epsilon, and realizable k-epsilon models, which shows that three models yield similar results. We selected the steady standard k-epsilon turbulence model as it has been demonstrated more computationally stable and less intensive for isothermal flow (Finlayson et al., 2004). Several user-defined functions (UDF) are created to simulate the highway-buildings environment.

### **2.3.1 Modeling Domain**

The modeling domain for our study was chosen as an approximate 800m×800m×150m block in the South Bronx (Figure 2.1). It consists of highway I-87, a surface street, U2, several low-rise buildings, and a high-rise building about 45m tall.

### **2.3.2 Boundary conditions**

The ambient wind and turbulence profiles representing the urban lower atmospheric boundary are created using surface meteorological measurement data recorded at La

Guardia Airport (6.4 km from the U2 site) and upper air data provided by the National Oceanic and Atmospheric Administration's Radiosonde Database.

Since the basic logarithmic velocity profile is not applicable for non-adiabatic conditions and the atmosphere is not adiabatic most of the time, we employ the *Monin-Obukhov similarity* for the non-adiabatic cases (Monin and Obukhov, 1954) in which the wind velocity profile is described by a power law function:

$$\bar{u}_x(z) = \bar{u}_x(h_r) \left(\frac{z}{h_r}\right)^p \quad (1)$$

where  $h_r$  is the reference height of the measurements;  $p$  is determined from the atmospheric stability and surface roughness;  $z$  is the position normal to the ground.  $p$  is determined from the atmospheric stability and surface roughness;  $z$  is the position normal to the ground. The method to estimate  $p$  as a function of surface roughness  $z_0$  and *Monin-Obukhov length*  $L$  is provided by Huang (1979). *Monin-Obukhov length*  $L$  is the height at the point where the turbulence caused by buoyancy equals that caused by mechanical forces. It represents the stability of the atmospheric surface layer. The degree of stability or instability of the atmosphere generally influences the vertical movement of air, which plays a significant role in pollutant transport in urban areas. The power law index  $p$  is calculated as a function of  $L$  and  $z_0$  as described in Huang (2013). The stability conditions for most hours fall into the unstable category which account for 42% of the entire stability condition in March of 2004.

The inlet k-epsilon turbulence parameters are defined by the following equations (Launder and Spalding, 1974):

$$k = \frac{u'^2}{0.3} \left(1 - \frac{z}{\delta}\right)^2 \quad (2)$$

$$\epsilon = \frac{C_\mu^{\frac{3}{4}} k^{\frac{3}{2}}}{K z} \quad (3)$$

where  $u'^2$  is the variance of wind speed;  $\delta$  is the estimated atmospheric boundary layer thickness;  $z$  is the position normal to the ground; and  $K$  is the Karman constant.

At the outlet of the modeling domain, diffusion fluxes for all flow variables in the direction normal to the exit plane are assumed to be zero. Outflow velocity and pressure are consistent with fully developed flow assumption. The top of the domain is set as a symmetry boundary, where there is zero flux for all quantities. A standard wall function that includes the momentum, energy, species transport, and turbulence equations near the wall is employed for the highway and building surfaces in the domain (Launder and Spalding, 1974). The ground surface is set as "wall" as well but with a surface roughness length of 2 m.

### **2.3.3 BC Emission Rate and Emission Zone Modeling**

The BC emission rates are estimated by the following procedures. First, the PM<sub>2.5</sub> emission factors reflecting the vehicle conditions in New York are obtained from the New York State Department of Transportation (NYSDOT). These emission

factor were generated using the MOBILE6.2 and are required for microscale air quality analyses in NYSDOT projects (2008). Second,  $PM_{2.5}$  emission factor for each vehicle type is multiplied by its corresponding traffic volumes. The two vehicle types, Categories I and II (defined in Section 2), are further classified by vehicle type distribution from NYSDOT (2008). Next, the relative fractions of BC in  $PM_{2.5}$  emissions from mobile sources were obtained from SPECIATE (Version 4.0), USEPA's repository of particulate matter (PM) speciation profiles of air pollution sources. SPECIATE reports elemental carbon (EC) measurements rather than BC. EC is typically defined as refractory carbon by thermal/optical method, while BC is defined as light-absorbing carbon by optical methods. Typically, BC optical and EC thermo-optical methods are highly correlated. (Lioussse et al., 1993; Chow et al., 2009) A recent study by Yan et al showed a strong correlation between the two methods in New York City (Yan et al.). As there is no simple conversion factor between BC and EC, many studies assumed that BC and EC are equivalent, the same assumption adopted in this study (Jeong et al., 2004; Watson, 2005; Chow et al., 2009). The average BC/ $PM_{2.5}$  fraction is 20% for Category I, and 65% for Category II, which are consistent with the findings from a number of experimental studies (Lena et al., 2002; Kim Oanh et al., 2010).

A uniformly mixed traffic emission zone was created by merging the turbulence zone on the surface of I-87. The height of the emission zone was estimated by the ratio of recorded traffic volume of Category I to Category II (Wang et al., 2011b). VIT is generated by modeling real-shaped vehicles in a traffic stream based on the traffic volumes and the ratio of Category I to Category II. To estimate RIT,

appropriate surface roughness lengths are selected for the highway surface and estimated temperature differences between highway surface and air is applied based on the weather data in New York (Wang and Zhang, 2009a). Values of turbulent kinetic energy are then calculated due to velocity gradients.

### **2.3.4 Background BC Concentrations**

The background BC concentrations for the modeling period are taken as the values of elemental carbon (EC) concentrations at the ambient air monitoring station operated by New York State Department of Environmental Conservation (NYSDEC), located at a New York City Intermediate School (IS 52), 681 Kelly Street off Prospect Avenue in the South Bronx.(Rattigan et al., 2010) With our assumption that EC and BC are equivalent, the daytime average BC concentration is estimated to be  $0.64 \mu\text{g m}^{-3}$  for the corresponding period of the simulation.

## **2.4. Results**

### **2.4.1 Model Evaluation**

Our model is evaluated against measured wind speeds, wind directions and BC concentrations under three types of highway-building environments (i.e., highway-building canyon, highway viaduct-building and transitional condition, which will be elaborated in Section 4.2), respectively. The performance metrics include Mean Normalized Error (MNE), Mean Normalized Bias (MNB), Mean Fraction Error (MFE), and Mean Fraction Bias (MFB). Unlike MNB and MNE, MFE and MFB do not assume that the field measurement is absolutely truth as the error and bias are normalized by the average of the model and observation. It is considered as a more

appropriate way to judge the performance of the model.(Boylan and Russell, 2006)  
Table 1 summarizes the performance metrics for predictions of wind speeds, wind directions, and BC concentrations. To the best of knowledge, our study is the first one that has introduced MFE and MFB into local-scale air quality modeling.

### **Wind Speed and Directions**

Figure 2.2 a and b compare the simulated and measured wind speed and directions, which shows a good agreement. Listed on Table 1, the MFE's and MFB's for the wind speed prediction are 5.40-7.62% and -3.66-6.47%, respectively. For direction prediction, MFE's and MFB's are 2.65-3.17% and 0.67-2.24%, respectively. This suggests that the CTAG model is capable of capturing the flow fields in the highway-building environment. It should be noted that the resolution of the measured wind direction is  $22.5^\circ$ , which results in multiple predicted wind directions corresponding to the same measured values (Figure 2.2b). The discrepancies between the simulated results and measurements are due to factors such as idealized building and roadway geometries, estimated ambient wind profiles of the lower atmospheric boundary layer and the turbulence model. The capability of capturing the flow fields is critical to our study. Modeled as an inert species, BC's transport is solely governed by turbulence mixing and meteorology. In other words, the absolute values of BC concentrations vary with BC emission factors, but the shapes of horizontal and vertical BC profiles are determined by the flow fields, which are the emphasis of this paper.

### **BC Concentrations**

Figure 2.2c compares the simulated and measured BC concentrations. The

MFE's and MFB's for the CTAG model are -6.46 to 11.77% and -6.46 to -14.08%, respectively. The relative narrow ranges of the two metrics suggest the model performances for the three types of conditions are similar. Boylan and Russell proposed the criteria for acceptable performance for regional-scale air quality modeling as that both the MFE is less than or equal to +75% and the MFB is less than or equal to  $\pm 60\%$  for major components of  $PM_{2.5}$ . (Boylan and Russell, 2006) In addition, the MNE's (from 16.44 to 21.24%) and MNB's (from -8.20 to -16.44%) in BC concentrations are comparable to those reported by Stein and coworkers in modeling local-scale benzene concentrations (MNE's from 46.37 to 79.87%; MNB's from 9.18 to 34.07%)(Stein et al., 2007). It should be noted that both BC and benzene were modeled as inert species. Therefore, the simulated BC concentrations are in an adequate agreement with the measurements. The further analysis of our modeling results suggests that BC concentrations are systematically underpredicted for a majority (11 out of 14) of the morning rush hours cases shown as solid circles in Figure 2c. A likely contributing factor to the difference between the real-world and modeled data is rooted from our adoption of NYC-regionally average vehicle type distribution in our emission estimates. The traffic videos indicate a large fraction of heavy-duty diesel vehicles in the Category II vehicles during the morning rush hours compared to the assumed average vehicle type distribution. However, the quality of the traffic videos due to the poor viewing angle makes it very difficult to further classify the vehicle size classes. In addition, morning rush hours may lead to transient driving conditions, which can result in higher emissions than cruising conditions. But their effects are expected to be minor because the periods we selected had mostly

cruise conditions.

In summary, the CTAG model is adequate to resolve the flow fields and BC concentrations in the highway-building environment under steady-state conditions in spite of the uncertainties in BC emissions. To generalize the results, the BC concentrations in the following sections are normalized by the concentrations on the edge the highway, which to a large extent eliminates the effects of uncertainties in emission estimates.

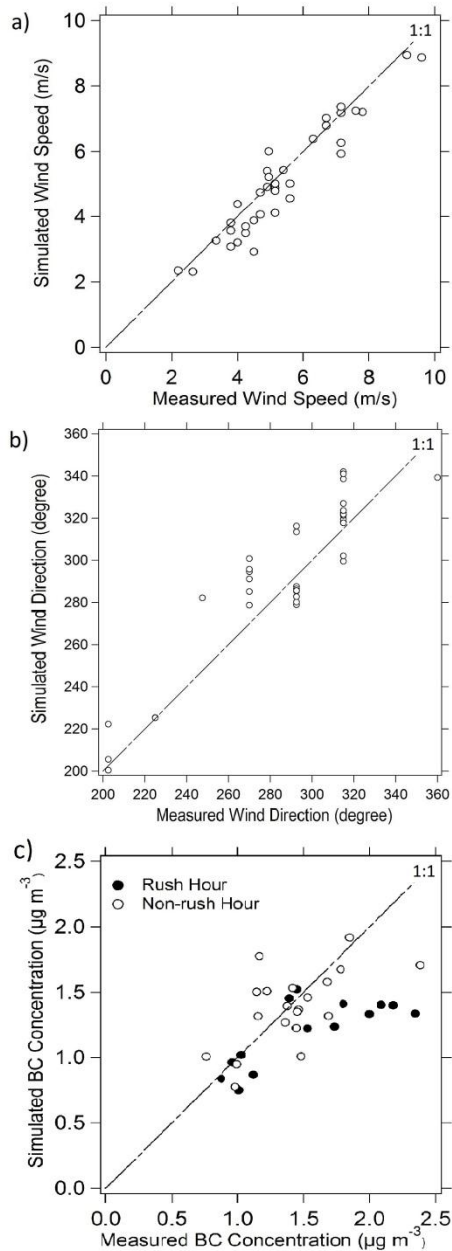


Figure 2.2: a) Simulated Vs. Measured Wind Speed b) Simulated Vs. Measured Wind Direction c) Simulated Vs. Measured BC Concentration.

## 2.4.2 Characterizations of the Highway-Building Environment

The evaluated CTAG model provides a valuable numerical tool for characterizing the highway-buildings environment, which we categorize into two main

conditions: 1) *highway-building canyon*, and 2) *highway viaduct-building*. *Highway-building canyon* describes the canyon between solid, elevated highway embankment and roadside buildings, where prevailing airflow is forced to flow over the highway (Figure 2.3a). *Highway viaduct-building*, on the other hand, refers to the space between an elevated highway supported by columns (i.e., a highway viaduct) and roadside buildings, where wind can stream from the space underneath the highway (Figure 2.3b). Both conditions occur at the U2 site due to the evolving highway geometry of I-87 combined with different wind directions.

### **Street Canyon**

*Highway-building canyon* is analogous to the familiar *street canyon* terminology. There are two aspect ratios associated with a street canyon,  $H/W$  and  $L/H$ , where  $H$  is the average height of building,  $W$  is the canyon width, and  $L$  is length of the building. Based on  $H/W$  and  $L/H$ , the characteristics of the flow field and pollutant transport over street canyon can be classified into three categories: isolated roughness flow, wake interference flow, and skimming flow. (Oke, 1988) Typically, for canyons where  $H/W < 0.3$ , only the wakes are disturbed (isolated roughness flow). For narrower canyons where  $H/W \approx 0.5$ , there is a strong interaction between the leeward vortex and windward vortex. Thus, the downward flow of the leeward eddy is reinforced by the windward vortex. In the case of  $H/W \approx 1$ , where isolated roughness flow transitions to skimming flow (most of the flow does not enter the canyon, and it is similar to simple driven cavity flow where a single vortex is developed) (Vardoulakis et al., 2003). In terms of pollutant dispersion, field studies have shown the pollutant concentration is directly linked to the flow field in the canyon.

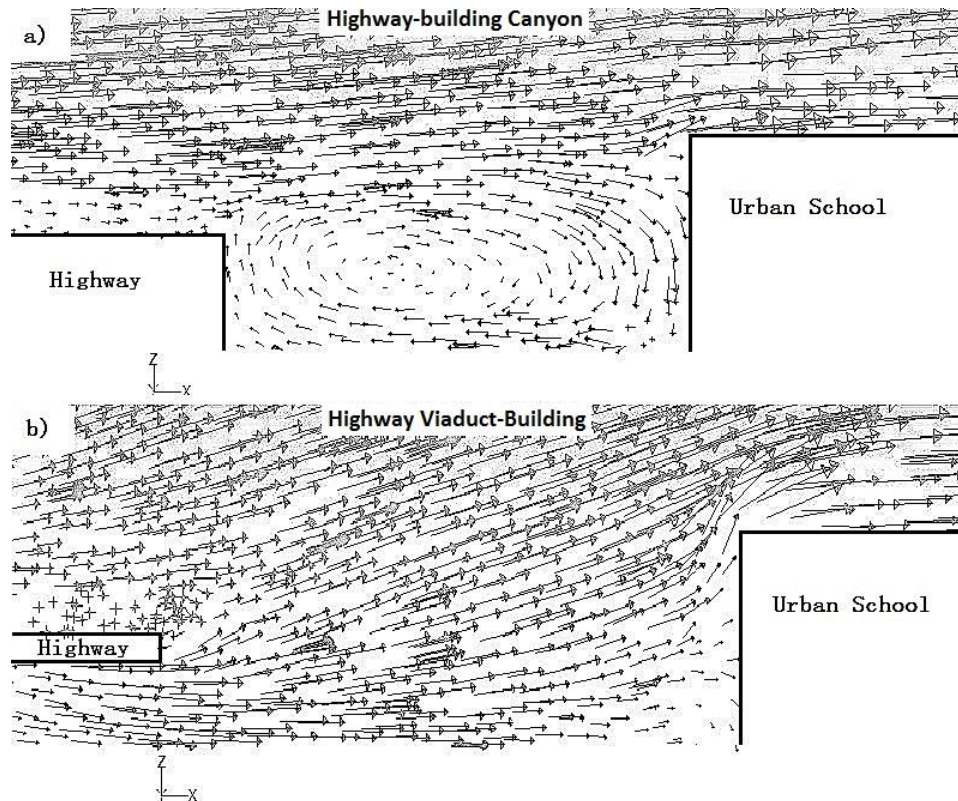


Figure 2.3: Flow field between highway and urban school (U2) varies with wind direction. *Highway-Building Canyon* conditions (a) occur mostly between solid highway embankment and U2, and *Highway Viaduct-Building* conditions (b) occur mostly between viaduct (middle section of highway shown in Figure 2.1 with open space underneath) and U2.

### Highway-building canyon

The *highway-building canyon* configuration modeled resembles a step-up condition of the street canyon in which the height of urban school U2 is greater than the elevation of the highway embankment (Hoydysh and Dabberdt, 1988). Since H and L are not equal on the upwind and downwind sides, we estimate  $H/W \approx 0.65$  by using the average height of highway and U2, and  $L/H > 6$  based on the geometry of U2 alone. Thus, the highway-building canyon can be classified somewhere between wake

interference flow and skimming flow (Oke, 1988). Figure 2.3a illustrates the vortex circulation due to flow separation inside the *highway-building canyon* between the highway and the urban school (U2) at an ambient wind direction of  $225^\circ$  (Figure 2.3b will be described in the Highway Viaduct-Building discussion). The flow field is comparable to previous studies on skimming flow over a street canyon (Xie et al., 2007). Figure 2.4a depicts the vertical profiles of BC concentration inside the *highway-building canyon* between the highway and the front gate of U2. The height is normalized by the elevation of the highway, and the BC concentration is normalized by the concentration at the edge of the highway. On the leeward wall (2m from the highway), the peak concentration occurs at the level slightly greater than the emission zone. This small rise can be explained by the buoyancy of exhaust produced by the greater temperature on the road surface, and the barrier at the edges of highway. This vertical profile is consistent with the finding in Wang and Zhang (2009a). The vertical BC concentration gradient at the core of vortex circulation ( $\sim 10\text{m}$  from the edge of the highway) is nearly zero below the highway elevation, indicating a well-mixed region. At the windward wall (the front gate of U2), the maximum concentration occurs at the ground level. The vertical profile of BC concentration can be approximated as a simple exponential function.

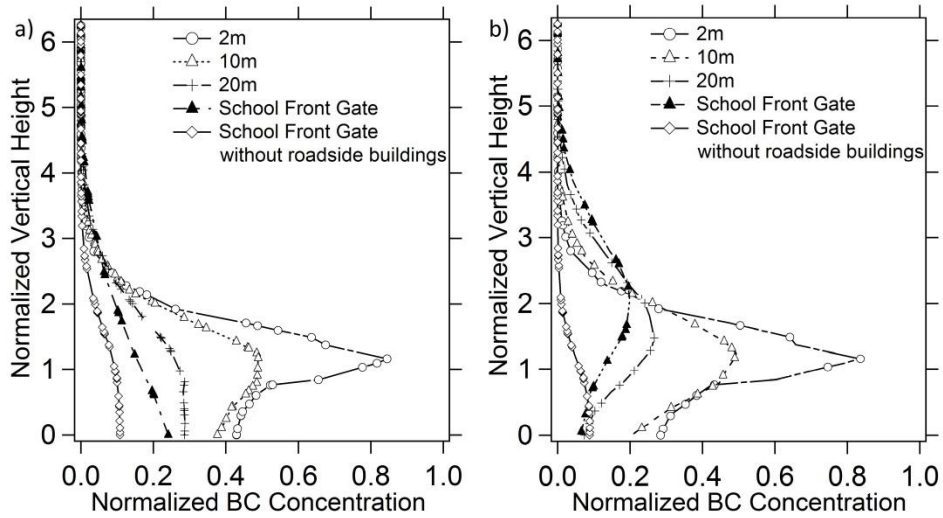


Figure 2.4: Simulated vertical BC Concentration as a function of distance away from the edge of the highway for a) highway-building canyon and b) highway viaduct-building conditions. Only highway emission source is considered. BC concentration is normalized by the concentration at the edge of highway, and vertical height is normalized by the elevation of the highway modeled. Wind direction is  $225^\circ$  for a) and  $292.5^\circ$  for b).

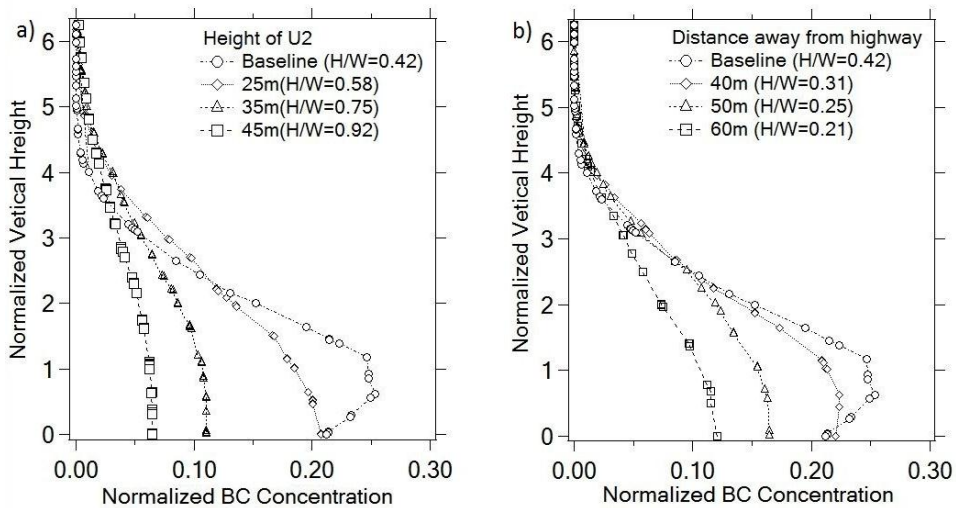


Figure 2.5: Simulated normalized vertical BC profiles at the front gate of the urban school (U2) under the transitional condition with a) Increasing aspect ratio  $H/W$  (Increasing the height of U2 from a baseline of 15m to 25m, 35m, and 45m.) and b) Decreasing aspect ratio

H/W (Translate U2 further horizontally from a baseline of 30 m away from highway to 40m, 50m, and 60m). All simulations are under the ambient wind direction of 270°. BC concentration is normalized by the concentration at the edge of highway, and the vertical height is normalized by the elevation of the highway modeled.

### **Highway Viaduct-Building**

Illustrated in Figure 2.3b, the flow field for the *highway viaduct-building* condition is very different from the *highway-building canyon* condition. There is no primary circulation vortex as shown in Figure 2.3a. The bulk of the flow from the bottom of highway is deflected upward once it hits the windward wall of U2, and a small windward eddy is formed (Figure 2.3b). Figure 2.4b depicts the normalized vertical BC concentration as a function of distance from the highway. The deflected airflow results in the maximum BC concentration slightly above the top of U2 ( “School Front Gate” in Figure 2.4b). However, the vertical profile of the BC concentration is comparable to *highway-building canyon* near the edge of highway.

### **Transitional condition**

At ambient wind direction around 270°, the highway-building environment is characterized by a transitional condition between the highway-building canyon and highway viaduct-building conditions (Figure 1.1). Illustrated as “Baseline” in Figure 2.5, the vertical profile at the front gate of U2 shows that maximum BC concentration occurs around the same height of the highway (~8 m), between the ground level, where the maximum concentration occurs in the highway-building canyon condition, and the height of U2, where the maximum concentration occurs in the highway

viaduct-building condition. For this transitional condition, the aspect ratio of a highway-building canyon significantly affects pollutant dispersion. We varied the aspect ratios ( $H/W$ ) to further explore its impact. The first set of simulations vary the height of U2 from 15 m to 25m, 35m, and 45m, corresponding to aspect ratios of 0.58, 0.75, and 0.92 respectively, which redefines the flow regime to skimming flow. Figure 2.5a shows the vertical profiles of BC concentration at the windward wall (i.e., the front gate of U2). As illustrated, BC concentration at the windward wall decreases as height increases, and maximum concentration of all the profiles occurs at the ground level due to circulation vortex. Similar to a step-up canyon, this occurs because the strength of eddies in the canyon grows as windward height increases. Growing eddies increases the dilution and ventilation rate, thus reduces the pollutant concentration. (Hoydysh and Dabberdt, 1988) It should be noted that this trend is different from that observed in the case of even street canyons (buildings with similar heights on both sides of the streets), where large aspect ratios ( $H/W$ ) typically hinder the entrainment of ambient air, resulting in elevated pollutant concentrations. (Chan et al., 2002; Boarnet et al., 2011)

The second set of simulations increase the distance between the urban school and highway to 40m, 50m, and 60m, effectively reducing  $H/W$  from 0.42 to 0.31, 0.25, and 0.21 correspondingly. The flow field evolves toward isolated roughness flow while the interaction of the leeward and windward vortex weakens. At  $H/W=0.21$ , the flow field resides in the regime where there are co-rotative vortices, a leeward eddy near highway embankment due to cavity of low pressure, and a smaller windward eddy in front of U2. The maximum normalized BC concentration at the school front

gate declines from 0.24 to 0.10 as H/W decreases to 0.21. Further decreasing H/W would result in independent wake flow, which substantially reduces BC concentration.

### **Open highway**

In order to estimate how different the BC concentrations are with buildings relative to a situation without airflow obstructions, we conducted simulations of the 34 cases discussed in Section 2 by removing all the roadside structures in our modeling domain while keeping everything else intact, referred to as *open highway* environments. As shown in Figure 2.4, the vertical BC profiles in the *open highway* environments are distinctly different than those in the highway-building environments (for both *highway-building canyon* and *highway viaduct-building*). It needs to be emphasized that all concentrations presented in Figure 2.4a and 4b are normalized by the same concentration (i.e., at the edge of the highway). For the 34 cases, the reduction in BC concentrations at the measurement point resulting from building removal varies from 43 to 54%, indicating a significant effect of roadside buildings on near-road air quality.

### **2.5. Implication**

The CTAG simulations combined with field measurements indicate that flow fields and pollutant transport can vary dramatically in highway-building environments. The CTAG model demonstrates adequate agreement with measurements at U2, and it is able to predict the flow field and spatial gradient of traffic-related air pollutants in complex highway-building environments under steady-state conditions. Under unsteady-state conditions such as those with intermittent wind speed, direction or

rapid changing traffics, steady-state profiles may not be achieved. The capability of the CTAG model in capturing the unsteady-state conditions has not been tested yet due to the limitation in the field datasets.

We show that the spatial variation of roadside pollutant concentration in the highway-building environment is dominated by the configuration of the highway, buildings, the relative distances between them, and the prevailing wind conditions. We evaluated two main configurations in a highway-buildings environment: *highway-building canyon* and *highway viaduct-building*, which lead to distinctly different spatial variations of air pollutants, vertically and horizontally. The two configurations may occur at different locations or even in the same location with different wind directions when highway geometry is complex. Furthermore, our simulation results suggest that BC concentration reaches its background level at height about 5 times the height of the highway regardless of types of highway-building conditions.

Our study implies that human exposure to traffic-related air pollutants in a highway-buildings environment, prevalent in urban areas, is governed by both highway and building configurations. Disregarding roadside buildings or highway configurations in a highway-building environment to assess near-road exposure may lead to significant discrepancies. The findings from this study demonstrate the need for a close collaboration between urban and transportation planners to tackle the near-road air pollution problems in highway-building environments. This collaboration will help towards creating a healthy environment for urban population.

## Chapter 3

# Roadside Vegetation Barrier Designs to Mitigate Near-Road Air Pollution Impacts

### Abstract

With increasing evidence that exposure to air pollution near large roadways increases risks of a number of adverse human health effects, identifying methods to reduce these exposures has become a public health priority. Roadside vegetation barriers have shown the potential to reduce near-road air pollution concentrations; however, the characteristics of these barriers needed to ensure pollution reductions are not well understood. Designing vegetation barriers to mitigate near-road air pollution requires a mechanistic understanding of how barrier configurations affect the transport of traffic-related air pollutants. We first evaluated the performance of the Comprehensive Turbulent Aerosol Dynamics and Gas Chemistry (CTAG) model with Large Eddy Simulation (LES) to capture the effects of vegetation barriers on near-road air quality, compared against field data. Next, CTAG with LES was employed to explore the effects of eight conceptual roadside vegetation/solid barrier configurations on near-road size-resolved particle concentrations, governed by dispersion and deposition. Our analysis indicated that the effects of vegetation barriers can be categorized into three general regimes: on-road, immediate barrier vicinity and near-road. For each of these regimes, the impacts on particle concentrations are also size-dependent. Our analysis further revealed two potentially viable design options: a) a wide vegetation barrier

with high leaf area density which reduces downwind particle concentrations significantly, while resulting in a moderate increase in on-road concentrations, and b) vegetation-solid barrier combinations, i.e., planting trees next to a solid barrier, leads to the greatest reduction in downwind particle concentrations among all configurations and a large increase in on-road concentrations at the same time. The findings presented in the study will assist urban planning and forestry organizations with evaluating different green infrastructure design options.

### **3.1. Introduction**

Roadside vegetation barriers have been evaluated as a potential mitigation strategy for near-road air pollution in several field, wind tunnel, and numerical studies (Bowker et al., 2007; Baldauf et al., 2008; Heist et al., 2009; Finn et al., 2010; Hagler et al., 2012; Steffens et al., 2012; Steffens et al., 2013; Al-Dabbous and Kumar, 2014; Brantley et al., 2014; Steffens et al., 2014). Those studies revealed that the effects of vegetation barriers on near-road air quality are primarily governed by two physical mechanisms, i.e., dispersion and deposition (Steffens et al., 2012; 2013; 2014). The impact of dispersion is demonstrated by upward deflection and deceleration of the approaching flow on the highway, as well as flow recirculation on both sides of the barrier. Deposition, on the other hand, removes particulate matter (PM) by Brownian diffusion, impaction, interception and gravitational settling. The deposition velocity,  $V_d$ , varies considerably depending on the particle size, for example, from  $\sim 3\text{cm s}^{-1}$  for 20 nm particles to  $\sim 0.3\text{cm s}^{-1}$  for particles approximately 100 nm (Zhang et al., 2001). Steffens et al. (2012) simulated the effects of vegetation barriers on near-road particle

size distributions characterized by a field experiment, and examined the knowledge gaps in capturing the impacts of dispersion and deposition, as well as proposed several recommendations on how to bridge those gaps.

The main objective of this study is to advance our understanding of the effectiveness of vegetation barriers as a potential mitigation strategy by quantitatively assessing the spatial variation of PM under various road-canopy configurations commonly present in the real world. We first incorporated the Large Eddy Simulation (LES) turbulence model, as recommended by Steffens et al. (2012) into the Comprehensive Turbulent Aerosol Dynamics and Gas Chemistry (CTAG) model, and evaluated the model performance against the same experimental dataset adopted by Steffens et al. (2012), which employed a Reynolds Averaged Navier-Stokes (RANS) turbulence model. Next, we compared six common near-road vegetation barrier configurations in terms of their impact to on-road and near-road particle concentrations. Finally, we provided design recommendations based on the results of our analysis.

### **3.2. Numerical Method**

The CTAG model was designed to resolve the flow field, including turbulent reacting flows, aerosol dynamics, and gas chemistry in complex environments (Wang and Zhang, 2009b; Wang et al., 2011b; Tong et al., 2012; Wang and Zhang, 2012; Steffens et al., 2013; Wang et al., 2013b; Steffens et al., 2014; Tong and Zhang, 2015). In this study, Large Eddy Simulation (LES) is applied to resolve the large-scale dominant unsteady motion within the vegetation canopy and requires modeling only small-scale, unresolvable turbulent motions. Previous studies demonstrated that LES is

capable of reproducing many observed features of turbulent flow within vegetation canopies by comparing with field and wind tunnel observations (Shaw and Schumann, 1992; Su et al., 1998; Dupont and Brunet, 2008). Steffens et al. (2013) compared the performances of LES and RANS models in predicting the spatial variations of tracer species behind a solid barrier, which demonstrated LES' advantages in resolving the flow recirculation patterns that commonly exist in the presence of a barrier.

### **3.2.1 Spatial Averaging of Vegetation**

Vegetation consists of numerous irregular small leaf and branch structures that inhibit the motion of incoming air flow. This complex structure within plant canopies makes it computationally prohibitive for explicit numerical modeling. In order to overcome this obstacle, the vegetation is spatially averaged to generate average flow speed and turbulence statistics within the canopy (Wilson and Shaw, 1977). The canopy is represented by a region of fluid only, where branches and leaves are not physically modeled. Their effects are modeled as sink terms in the governing equations (Sections 2.2 and 2.3). Detailed assumptions on spatial averaging practice are described in Steffens et al. (2012).

### **3.2.2 Large Eddy Simulation (LES)**

LES with a dynamic subgrid model is modified to include the aerodynamic effects of the drag element due to leaf and branch structures that impede the motion of incoming flow (Shaw and Schumann, 1992; Dupont and Brunet, 2008). In LES, filtered continuity and momentum equations are shown below:

$$\frac{\partial \rho}{\partial t} + \frac{\partial \rho \tilde{u}_j}{\partial x_j} = 0 \quad (4)$$

$$\frac{\partial \rho \tilde{u}_i}{\partial t} + \frac{\partial \rho \tilde{u}_i \tilde{u}_j}{\partial x_j} = -\frac{\partial \tilde{p}}{\partial x_i} + \frac{\partial \tau_{ij}}{\partial x_j} + \frac{\partial \sigma_{ij}}{\partial x_j} + S_u \quad (5)$$

$S_u$  is the a drag term imposed by the vegetation, which is proportional to the Leaf Area Density (LAD) and the plant drag coefficient shown in Eqn 6 (Thom, 1972).

$$S_u = -\rho C_D LAD u^2 \quad (6)$$

$\tau_{ij}$  is the filtered stress tensor, and  $\sigma_{ij}$  is the subgrid-scale Reynolds stress, which is modeled by the Boussinesq hypothesis in Eqn 7:

$$\sigma_{ij} - \frac{1}{3} \delta_{ij} \sigma_{kk} = -2\mu_t \overline{S}_{ij} \quad (7)$$

$\overline{S}_{ij}$  is the rate of strain tensor of the resolved scale under the presence of the vegetation drag term. A well-established dynamic Smagorinsky model is employed to model the subgrid viscosity  $\mu_t$  in Eqn 8 (Germano et al., 1991). The dynamic model removes some problems associated with the constant coefficient Smagorinsky model by eliminating the need to prescribe a length scale and near-wall correction (Pope, 2000).

$$\mu_t = \rho (L_S)^2 |\overline{S}| \quad (8)$$

$L_s$  is the mixing length scale that depends on the size of the computational cell and the dynamically computed Smagorinsky constant.

Researchers in the past either modeled the subgrid viscosity by solving an additional kinetic energy transport equation with a source term to represent the creation of turbulent kinetic energy (TKE) by vegetation, or directly employed dynamic Smagorinsky model (Shaw and Zhang, 1992; Watanabe, 2004; Cassiani et al., 2008). In this study, we compared the two subgrid modeling approaches. The flow fields simulated by the two approaches are very similar, which is likely due to the fact that the majority of the TKE is explicitly resolved, and only a small portion is modeled. We therefore choose the dynamic Smagorinsky model for purpose of lower computational cost.

### 3.2.3 Particle Dispersion and Deposition

Only dispersion and deposition are considered in the model. Any process that leads to particle transformation is not explicitly simulated as a model limitation. However, by constraining the emission factors against the data at the no-barrier site, we already incorporated part of the aerosol dynamics. More details are provided in Section 3.2. Scalar transport equation is employed to model particle dispersion and deposition from on and near roadways:

$$\frac{\partial \overline{N_p(D_p)}}{\partial t} + \frac{d\tilde{u}_j \overline{N_p(D_p)}}{dx_j} = \frac{\partial}{\partial x_j} \left[ (D_t + D_m) \frac{\partial \overline{N_p(D_p)}}{\partial x_j} \right] + S_d(D_p) \quad (9)$$

$\overline{N_p(D_p)}$  is the average particle concentration for each particle size.  $D_t$  is the turbulent

diffusivity, and  $D_m$  is the molecular diffusivity.  $S_d$  is the sink term to represent the effect of deposition, which is the function of particle size  $D_p$ .

$$S_d(D_p) = N_p \widetilde{(D_p)} V_d(D_p) LAD \quad (10)$$

$V_d(D_p)$  is the particle deposition velocity derived from the dry deposition model from Zhang et al. (2001). The aerodynamics resistance  $r_a$  (part of the total resistance to compute deposition velocity) is not included since the aerodynamic effect is already explicitly resolved by LES.

### 3.3. Model Evaluation

#### 3.3.1 Chapel Hill Field Experiment

The CTAG/LES model for vegetation barriers is evaluated against the experimental data collected in Chapel Hill, North Carolina, USA as reported by Hagler et al. (2012). For this study, the near-road vegetation barrier consisted of a mix of 6-8m tall coniferous trees with full cover from the ground to the top of the canopy. A section along the same stretch of limited-access roadway contained the roadside vegetation barrier as well as an area with no barrier or other obstructions to air flow from the road. Wind speed and direction measurements were collected using a 3-D ultrasonic anemometer with a sampling frequency of 1 Hz. Particle size distributions were obtained using scanning mobility particle sizers (SMPS), which captured 88 size channels ranging from 12.6nm to 289 nm both at the no-barrier site and behind the barrier at two heights.

### **3.3.2 Boundary Conditions**

In the Chapel Hill simulation, the computational domain and boundary condition are identical to those in our previous study (Steffens et al., 2012). The inlet profile and vehicle-induced turbulence (VIT) are constrained in the way that modeled wind velocity matches the measured values at the no-barrier site. The traffic emission factor cannot be determined experimentally; therefore, the road level size-resolved emission factors (Zhang et al., 2005) were derived based on particle size distribution (PSD) measurement at the no-barrier site using inverse modeling. The road-level emission factor, which describes the emission profiles on or near the roadway curb, takes into account any changes in PSD due to particle transformation in the “tailpipe-to-road” process (Zhang and Wexler, 2002). The friction velocity is estimated by matching the velocity profile at the top of the canopy (Stull, 1988; Steffens et al., 2012). The particle size distribution of vehicular emissions released from the road is set such that PSD simulated at the no-barrier site matches that of the experiment. Additional details can be found in Steffens et al. (2012).

### **3.3.3 Simulation Results**

Three periods were selected according to the description in Steffens et al (2012), namely Morning, Peak 1, and Peak 2, as the wind speed and direction are relatively constant among the three periods (Steffens et al., 2012). In this model, nine discrete bins were employed to represent the particle size distribution from 12.6nm to 289 nm. LAD profiles of the vegetation barrier is set the same as Steffens et al. (2012). Figure 3.1 demonstrates the simulation results for the three selected scenarios.

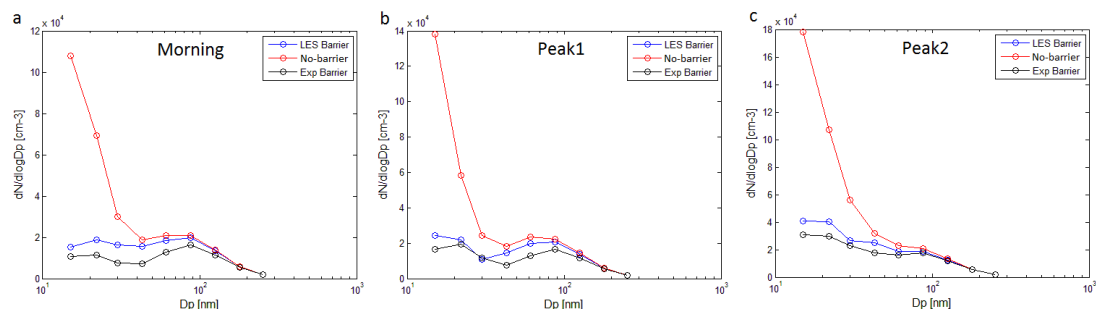


Figure 3.1: Particle size distribution (PSD) for three modeling scenarios (Morning, Peak1, Peak2). “LES Barrier” stands for simulation results by Large Eddy Simulation (LES). “No-barrier” stands for experimental result at the no-barrier site. “Exp Barrier” stands for the experimental result behind the barrier.

As shown in Figure 3.1, although discrepancies are present, the LES model adequately captures the trend observed in the experiment. The model prediction shows close agreement with on-site measurements behind the vegetation barrier. The differences are likely due to spatial averaging of modeled vegetation and uncertainties in data collection, which cannot fully simulate branches and leaves in reality.

### 3.4. Evaluation of Vegetation Barrier Design Configurations

#### 3.4.1 Barrier Configurations

Six common near-road configurations as well as a series of sensitivity studies on several physical parameters are investigated in this section (Figure 3.2). The evaluated LES model is employed to simulate near-road particle size distributions. Table 3.1 shows the physical parameters of the barrier and boundary conditions studied. Leaf Area Density profiles for all configurations are obtained from Steffens et al. (2012) representing coniferous evergreens, which are usually preferable in air pollution mitigation because of their high surface areas, low VOC emission rates,

limited seasonal changes, and long lives (Lovett, 1994; McDonald et al., 2007; Fuller et al., 2009). The inlet wind profile for the baseline case is also taken from Steffens et al. (2012), representing unstable conditions.

Case 0 stands for a no-barrier scenario, which serves as a comparison for the other configurations. Case 1 is the configuration with a wide vegetation barrier located next to the road. Case 2 represents a solid barrier, and Case 3 represents a “green wall”, which is a combination of solid barrier and vegetation cover. Leaf area index (LAI=2) of the vegetation cover is taken from the literature (Litschke and Kuttler, 2008). Case 4 represents a scenario where a tall vegetation barrier is behind a solid wall, referred to as “vegetation-solid barrier combination”. Case 5 represents a condition where both upwind and downwind vegetation barriers are present. The dimensions of each of these configurations are shown in Table 2.

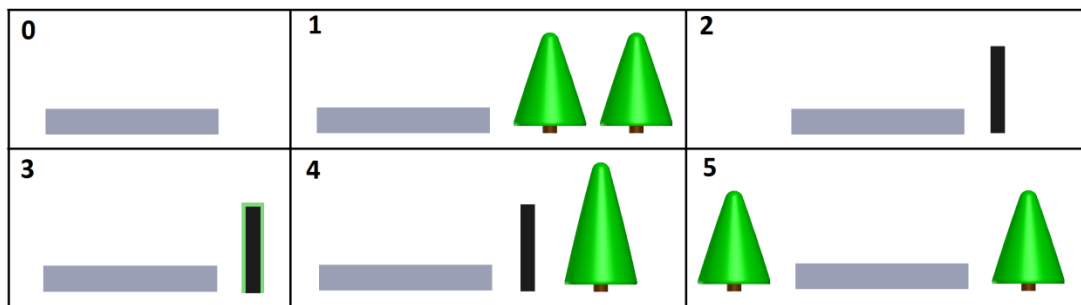


Figure 3.2: Schematics of six roadside barrier configurations. In the simulation, the complex geometry of the vegetation canopy is modeled as rectangular blocks. Leaf Area Density (LAD) profiles of coniferous trees are applied on each block to represent the real geometry of coniferous evergreen.

Table 3.1: Description of roadside barrier geometry for all configurations tested

Case #	0	1	2	3 <sup>a</sup>	4		5	
					Solid barrier	Vegetation barrier	Upwind vegetation barrier	Downwind vegetation barrier
Height	N/A	6 m	6 m	6 m	6 m	10 m	6 m	6m
Width	N/A	6m,12 m,18m	1 m	1m+0.25 m	1 m	6 m	6 m	12m
LAD <sup>b</sup>	1	1,1.5	1	0.33 <sup>c</sup>	N/A	1, 0.25	1	1
U	2 m/s	1, 2, 4 m/s	2 m/s	2 m/s	2 m/s		2 m/s	
Stability <sup>d</sup>	Unstable	Stable, Unstable, Neutral	Unstable	Unstable	Unstable		Unstable	

<sup>a</sup>: Case 3 represents a solid barrier with vegetation cover. The thickness of the cover is 25 cm.

<sup>b</sup>: LAD in the unit of  $m^2m^{-3}$ . “1” stands for the baseline LAD profile of conifer trees, “0.5” means 50% less of the baseline LAD, and “1.5” is 50% more than the baseline LAD.

### 3.4.2 Boundary Conditions

For the six tested configurations, the computational domain has a dimension of 250m x 200m x 30-50m divided into 3.5 to 5 million elements. The average element size of the vegetation barrier is about 0.3m. The height of the domain is about 5 times the height of the barrier, which avoids blocking effect and unphysical flow acceleration (Tominaga et al., 2008). A grid independency study was conducted to ensure the results are independent of domain size and mesh resolution. The schematic drawing of the baseline configuration is shown in Figure 3.3. The ground surface and solid barrier surfaces are defined as a no-slip wall. The top and two sides of the computational domain are set as symmetry conditions with zero shear. Outflow boundary condition is specified at the outlet of the domain. The average inlet wind velocity  $u$  is 2 m/s for the baseline. Wind direction is chosen to be normal to the barrier as the impact of barrier on local air quality is greatest. In case 4, we explored the effect of wind direction on on-road and near-road air quality. The vehicular size-

resolved emission factor and VIT are set the same as the Chapel Hill case.

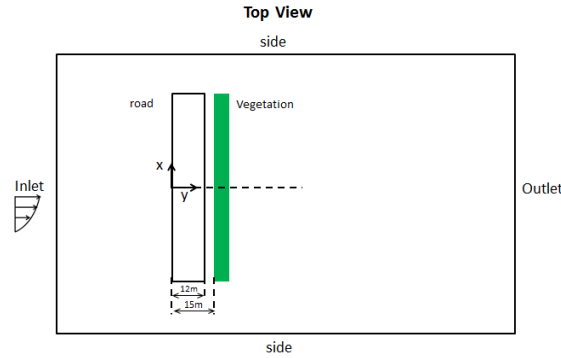


Figure 3.3: Schematics of the baseline configuration (Case 1)

### 3.4.3 Results and Discussion

#### 3.4.3.1 Case 1

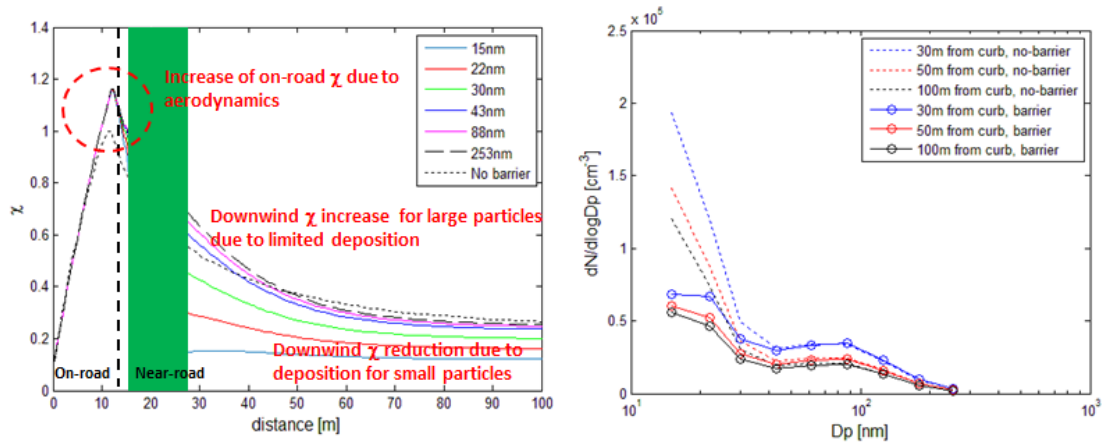


Figure 3.4: a) Horizontal gradients of size-resolved particle concentrations from 15nm to 253nm. 9 particle sizes are simulated, but 6 bins are plotted for clarity.  $\chi$  is the particle concentration normalized by the peak concentration from the no-barrier case at the same particle size. The vertical dash line separates the on-road and near-road domains. The green strip indicates the location and width of the vegetation barrier. b) Particle size distribution (PSD) of the baseline; dash lines represent the no-barrier case.

Figure 3.4a shows the normalized horizontal gradients of particle concentration

$\chi$  of diameters varying from 15nm to 253nm.  $\chi$  is the particle concentration normalized by the peak concentration from the no-barrier case at the same particle size. The effects of the vegetation barriers are evident in three regimes: On-road, the immediate vicinity behind the vegetation barrier, and near-road. For the on-road regime, the presence of a vegetation barrier elevates the on-road concentration due to the deceleration of approaching flow and on-road particle accumulation upwind to the barrier. Based on this particular configuration, a roughly 15% increase over the no-barrier case is observed (Figure 3.4a, b). This phenomenon is similar to that often observed in the presence of solid barriers (Finn et al., 2010; Baldauf et al., 2011; Hagler et al., 2011). For the regime of the immediate vicinity behind the vegetation barrier (~20 m downwind of the barrier for this particular case), reduced dispersion within the vegetation canopy, and the behind-barrier wake zone result in greater concentration for relatively large particles (small deposition velocity) than that of the no barrier case, as the effects of dispersion in the no barrier section overwhelm the deposition for those particles within the vegetation. In contrast, a sharp drop in concentrations was observed in the vegetation for relatively small particles with high deposition velocity.

A cross-over point is observed at around 45m (or ~20m downwind of the barrier) for relatively large particles (>43nm in this case). Beyond that point, a lower concentration than that for the no-barrier case was found for all particle sizes. A mass balance analysis is conducted for the 180nm particles (with low deposition velocity). It is shown that the increase of the total particle number with vegetation over the no-barrier case is almost equivalent to the decrease of the total particle number over the

same case. A better illustration is shown in Figure 3.5. A-B is the increase of the total number of particles over that of the no-barrier case. D-C is the decrease of the total number of particles over that of the no-barrier case. It is demonstrated that the increase of the total particle number (by integrating the number concentration over the computational volume before the cross-over point) over the same volume of the no-barrier case is almost equivalent to the decrease of the total particle number over the volume of the no-barrier case. This implies that the on-road particle accumulation leads to near-road pollutant reduction when deposition is absent.

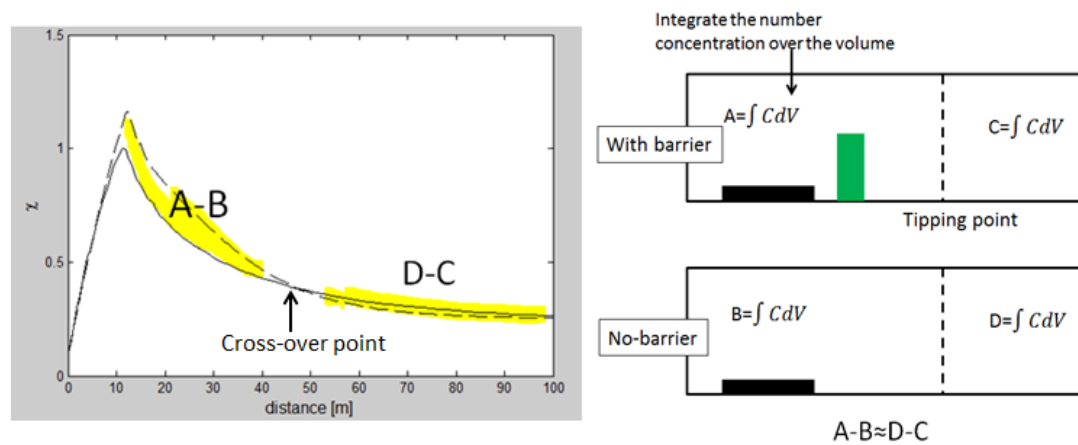


Figure 3.5: a) Illustration of Mass Balance Analysis for 180 nm particle b) Normalized concentration decline over distance. Dash line stands for the with-barrier case. Solid line indicates the no-barrier case

### 3.4.3.2 Case 2, 3 and 4

For the scenario with a roadside solid barrier (Case 2), a significant reduction behind the barrier is observed for all particle sizes as the plume is forced to deflect upward when approaching the barrier. Consistent with the findings from Steffens et al. (2013 and 2014), the presence of a solid barrier creates an upward deflection of incoming airflow and a recirculation cavity behind, which increases the on-road

particle concentrations by almost 85% but results in a sudden concentration deficit across it (Figure 3.6a). Figure 6b shows that the horizontal gradients behind a solid barrier with vegetation cover (Case 3) are very similar to that behind a solid barrier (Case 2), which suggests that the additional particle reduction by having vegetation cover on solid barriers is insignificant because the total leaf surface area of vegetation cover is small in contrast with the tree stands and the boundary layer formed along the solid barrier surface likely inhibits air flow through the vegetation. Case 4, i.e., “vegetation-solid barrier combination”, sees the largest reduction in particle concentrations downwind of the barrier due to the synergistic effect between the solid barrier and vegetation canopy (Figure 3.6c). Relative to Cases 2 and 3, the concentrations of all particle sizes are lower than for both the no-barrier case (Case 0) and the solid barrier case (Case 2) downwind of the barrier.

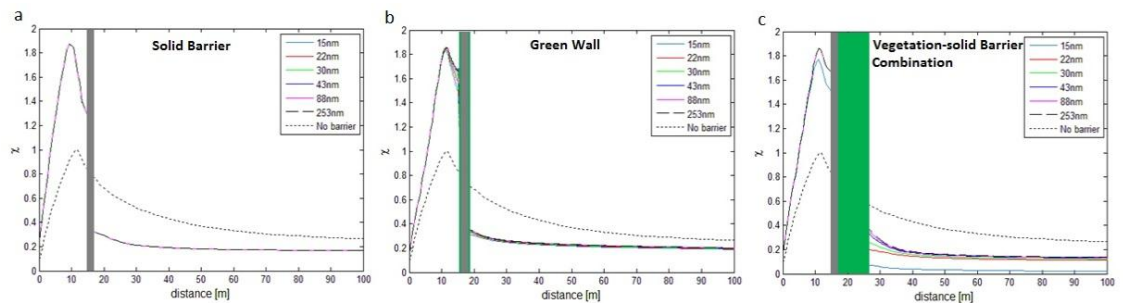


Figure 3.6: Horizontal gradients of size-resolved particle concentrations for Cases 2 (a), 3 (b) and 4 (c). The green strip indicates the location and width of the vegetation barrier. The grey strip indicates the location and width of the solid barrier. The strips with green on both sides designate the location and width of a “green wall”.

### 3.4.3.3 Case 5

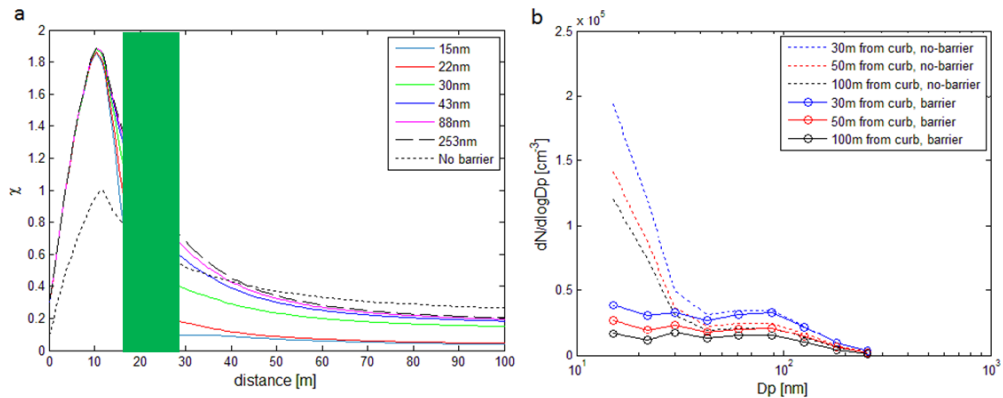


Figure 3.7: a) Horizontal gradients size-resolved particle concentrations; b) PSD for Case 5; The green area indicates the location and width of the vegetation barrier.

The upwind vegetation barrier in Case 5 substantially elevates the on-road concentration by 85% over the no-barrier case since it slows down the on-road dispersion (Figure 3.7). This effect is similar to that of the solid barrier case (Figure 3.6a). However, a steeper concentration decline along the wind direction is found for all particle sizes compared with the no-barrier case. This ultimately results in lower concentration further downwind in the far field compared with those at the same distances downwind of the no-barrier case.

### 3.4.3.4 Sensitivity Study on Case 1

#### *Leaf Area Density*

LAD is an important parameter for determining the amount of deposition that takes place within the canopy as well as the reduction in air flow turbulence (Petroff et al., 2009). To test the effect of LAD, a sensitivity study is performed by increasing the baseline LAD by 50% while fixing the rest of the parameters. It is found that increasing LAD leads to a greater on-road concentration and substantially lower

concentration behind the barrier than those from the baseline case, especially for particles  $\leq 50\text{nm}$  (Figure 3.8 a, b). However, this effect is non-linear suggesting that simply doubling the LAD would not double the reduction of the particle concentration. A noteworthy finding is illustrated in Figure 3.8 where the PSD from the solid barrier case (Figure 3.8c) is placed on the right end. For relatively large particles, increasing LAD leads to more concentration reduction beyond 30m downwind of the canopy. However, the largest reduction is observed for the solid barrier scenario, where the overlapping PSD curves (Figure 3.8c) result from absence of deposition for the solid barrier (Figure 3.8c). This trend indicates that increasing the LAD of the vegetation barrier would ultimately lead to a pollutant reduction effect similar to a solid barrier for large particles with relatively small deposition velocity.

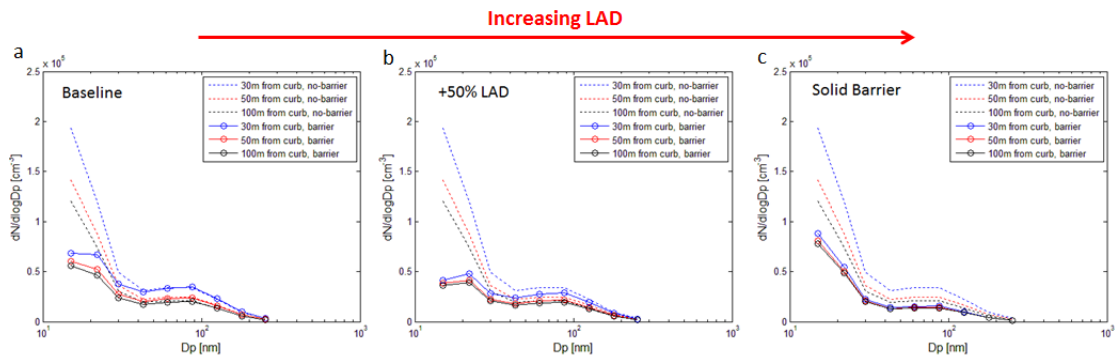


Figure 3.8: PSDs with increasing LAD a) baseline LAD b) +50% LAD c) solid barrier.

### Vegetation Barrier Width

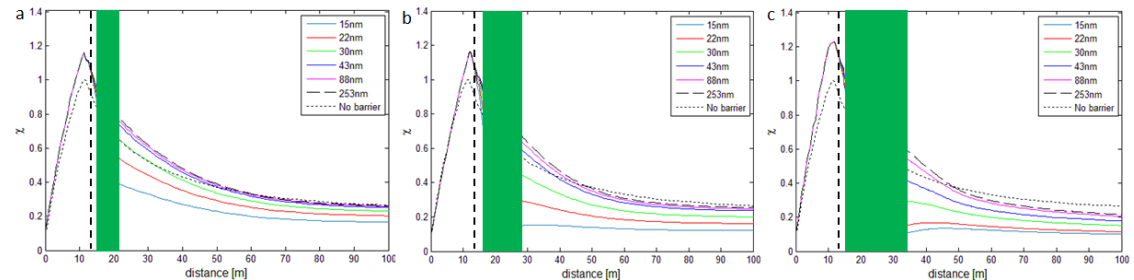


Figure 3.9: Horizontal gradients of Case 1 with a) 6m b) 12m c) 18m vegetation barrier

The width of vegetation barrier is another important factor for roadside dispersion and deposition (Brantley et al., 2014). The barrier width of Case 1 is varied by  $\pm 50\%$  to test its sensitivity. Increasing the width of the vegetation barrier results in a greater concentration reduction behind the barrier for all particle sizes due to enhanced deposition effect of vegetation. In addition, increasing the width of the vegetation barrier also likely raises on-road concentrations due to weakened on-road dispersion, but to a lesser extent than the cases with solid barriers. In addition, this increase in on-road concentrations may not occur in real-world situations since VIT may increase mixing and dilution of the traffic plume, a condition that cannot be simulated by this modeling.

### *Stability*

Our previous study showed that near-road dispersion over a solid barrier is strongly affected by atmospheric stability (Steffens et al., 2013). A variety of atmospheric stability conditions are evaluated to explore the impact on vegetation barriers. The horizontal gradient is normalized by the peak concentration of the no-barrier case under unstable conditions. As presented in Figure 3.10, a stable condition leads to the greatest on-road concentration elevation. In contrast, an unstable condition results in the least on-road concentration increase due to enhanced vertical mixing. A neutral condition remains in the middle between stable and unstable. The finding here also reveals that atmospheric stability has more impact on particle dispersion than on deposition.

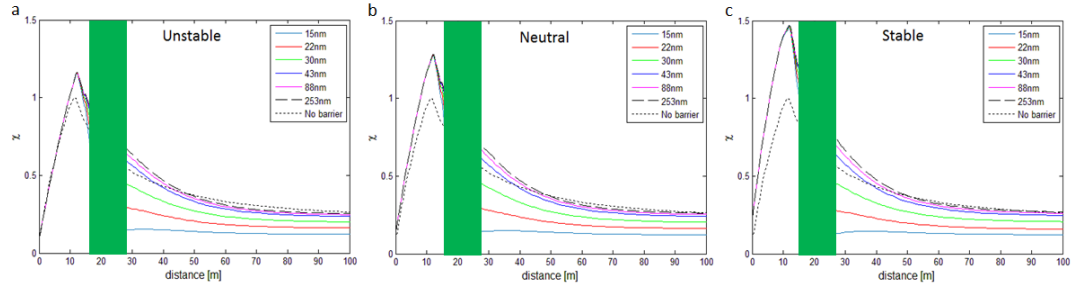


Figure 3.10: Horizontal gradients under three atmospheric stability conditions a) unstable, b) neutral, and c) stable. A no-barrier case for the unstable condition is shown by black dash lines for comparison. 9 particle sizes are simulated, but 5 bins are plotted for clarity.

### Wind speed

The influence of oncoming wind speed is explored by varying the baseline wind speed from 50% to 200% of the baseline. In this comparison, the difference due to wind speed is eliminated by normalizing the horizontal gradient of the same wind speed of the no-barrier case in order to better present its effect on deposition. As presented in Figure 3.11, it is shown that fewer particles are removed by deposition, with increasing wind speed since particle residence time through the canopy is shortened.

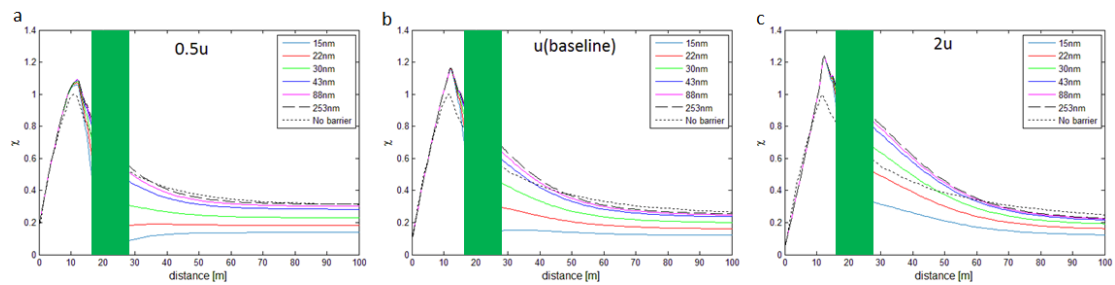


Figure 3.11: Horizontal gradients for a) 50%, b) 100%, and c) 200% of the baseline wind speed ( $u$ ) profiles. Horizontal gradients are normalized by the concentration of the no-barrier case at the same wind speed as comparison. 9 particle sizes are simulated, but 6 bins are plotted for clarity. The green strip indicates the location and width of the vegetation barrier.

*Oblique Wind Direction*

An increase of on-road concentration upwind to roadside barriers is often observed in the literature as a result of blocking on-road dispersion (Baldauf et al., 2008; Heist et al., 2009; Hagler et al., 2011; Steffens et al., 2013). Case 4 is chosen as the baseline due to the largest on-road concentration elevation. A translational periodic boundary condition is applied on sides as we only modeled a section of roadway with finite length. Our simulation indicated that the degree of on-road increase is contingent on oncoming wind direction (

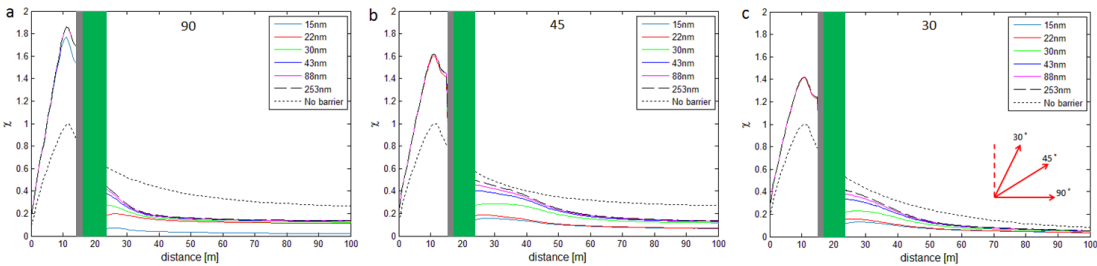


Figure 3.12). The on-road concentration decreases with more parallel wind to the road due to reduced blocking of on-road dispersion. Furthermore, oblique wind directions lead to relatively greater near-road concentration in the wind direction as a tradeoff of the decrease in on-road concentration.

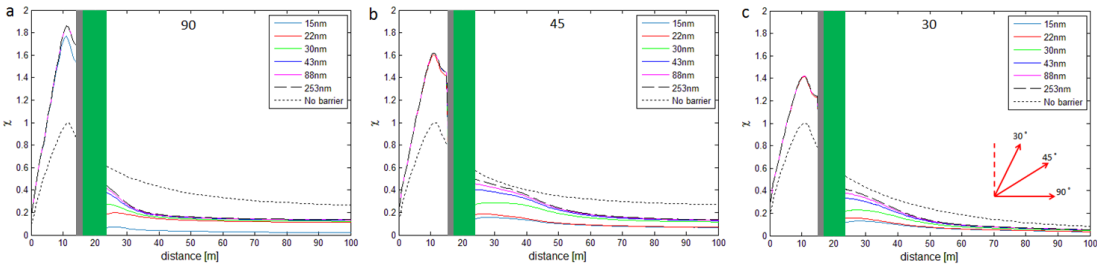


Figure 3.12: Horizontal gradients of three oncoming wind directions (30, 45, 90 degrees). The test scenario is based on Case 4, vegetation-solid barrier combination. Wind direction of 90 degree is normal to the roadway.

### 3.5. Conclusion

The primary objective of this study is to provide design recommendations to assist urban planners in evaluating different green infrastructure designs. The near-road air quality is primarily driven by two physical mechanisms, i.e., dispersion and deposition, and deposition only occurs in the presence of vegetation. Our analysis demonstrates that the impacts on roadside air quality are particle size-dependent. For regulation purpose, it is important to differentiate fine and ultrafine particles as their physical behavior are different in the roadside environment. And currently, there is no air quality standard for ultrafine particles.

Based on our analysis, two potentially viable design options are revealed: a) a wide vegetation barrier with high leaf area density (Case 1 with high LAD and width, Figure 9c), and b) vegetation-solid barrier combinations, i.e., planting trees next to a solid barrier. A solid barrier (Case 2, Figure 3.6a) creates an upward deflection of incoming airflow and deceleration of the approaching flow, which increases the on-road particle number concentration by almost 85% but results in a large concentration drop across it. In this process, deposition due to vegetation is absent and reductions are driven by dispersion only. A solid barrier with vegetation cover (Case 3, Figure 3.6b) is found to be very similar to an only solid barrier case. The additional particle reduction by having vegetation cover on a solid barrier is insignificant because the total leaf surface area of the cover is small compared to tree stands. A vegetation-solid barrier combination (Case 4, Figure 3.6c) results in the highest reduction in downwind particle concentrations among the six configurations evaluated, although modeling suggests a large elevation in on-road concentrations occurs. Similar to Case 2, the

upwind vegetation barrier in Case 5 (Figure 3.7) substantially elevates the on-road concentration by slowing down the on-road wind speed and reducing the dispersion. Based on our analysis of all barrier configurations, a wide vegetation barrier with high leaf area density barrier (Case 1 with high LAD and width) and a vegetation-solid barrier combination (Case 4) are found to be potentially viable with regard to roadside mitigation of near-road PM, especially UFPs.

This study has some limitations for roadside design. First, no other structures which may have complicated the near-road dispersion besides the roadside barriers are considered in the model. Second, the results are based on coniferous evergreens and may not be applicable to broad-leaved trees. Third, there are uncertainties associated with parameters such as LAD profiles, dry deposition models, and drag coefficient. Therefore, specific results in the simulation, such as the percentage of concentration reduction and size of the different regimes may not be generalized. While the general trends and design recommendations presented in this study provide insights for vegetation barrier designs, future implementations need to take into account site-specific characteristics, given the complexity of urban landscapes.

## Chapter 4

# The Near-Source Impacts of Diesel Backup Generators in Urban Environments

### Abstract

Distributed power generation, located close to consumers, plays an important role in the current and future power systems. However, its near-source impacts in complex urban environments are not well understood. In this paper, we focused on diesel backup generators that participate in demand response (DR) programs. We first improved the micro-environmental air quality simulations by employing a meteorology processor, AERMET, to generate site-specific boundary layer parameters for the Large Eddy Simulation (LES) modeling. The modeling structure was then incorporated into the CTAG model to evaluate the environmental impacts of diesel backup generators in near-source microenvironments. We found that the presence of either tall upwind or downwind building can deteriorate the air quality in the near-stack street canyons, largely due to the recirculation zones generated by the tall buildings, reducing the near-stack dispersion. Decreasing exhaust momentum ratio (stack exit velocity/ambient wind velocity) draws more exhaust into the recirculation zone, and reduces the effective stack height, which results in elevated near-ground concentrations inside downwind street canyons. The near-ground  $PM_{2.5}$  concentration for the worst scenarios could well exceed  $100 \mu\text{g m}^{-3}$ , posing potential health risk to

people living and working nearby. In general, older diesel backup generators (i.e., Tier 1, 2 or older) without the up-to-date emission control may significantly increase the pollutant concentration in the near-source street canyons if participating in DR programs. Even generators that comply with Tier-4 standards could lead to PM hotspots if their stacks are next to tall buildings. Our study implies that the siting of diesel backup generators stacks should consider not only the interactions of fresh air intake and exhaust outlet for the building housing the backup generators, but also the dispersion of exhaust plumes in the surrounding environment.

#### **4.1. Introduction**

Small distributed power generation is becoming more popular due its flexibility and efficiency compared with central power generation (Pepermans et al., 2005). These units are typically located in populated urban areas with relatively short stack heights. Since they are closer to consumers, their environmental impacts have become a concern despite the benefits. Several studies have evaluated the air quality impact from distributed generation (Greene and Hammerschlag, 2000; Heath et al., 2006; Strachan and Farrell, 2006; Carreras-Sospedra et al., 2010; Jing and Venkatram, 2011). However, very few studies have examined the effects of complex urban environments such as street canyons on the near-source air quality impacts. This paper aims to bridge this gap.

Diesel backup generators, often referred as “standby generators” or “emergency generators”, are one type of distributed generation. Their primary purpose is to preserve essential facility functions in the event of a loss of grid power or for situations that threaten the facility, such as fire pump use during a fire(NESCAUM,

2012). Those generators can also operate during periods of peak electricity demand, increasing grid reliability and supporting the electricity delivery systems (Gilmore et al., 2006). For example, it is estimated that over 1,000 MW of backup generation capacity has been installed in New York City (NESCAUM, 2003), and the New York Independent System Operators (NYISO) allows backup generators to participate in its demand response (DR) programs (Gilmore et al., 2010). Although there are several benefits of using diesel backup generators for DR, many of them have non-trivial air emissions (Gilmore et al., 2006; Shah et al., 2006). The U.S. Environmental Protection Agency (USEPA) first introduced Tier 1 emission regulation for non-road diesel generators in 1996, and the permitted levels of nitrogen oxides (NO<sub>x</sub>) and particulate matter (PM), the two main pollutants from diesel engines, have gone down significantly since then (USEPA, 2014). However, a large percentage of diesel backup generators that are in use are Tier 1, Tier 2 or older, which have considerably higher emission rates than those of the latest models (Zhang and Zhang, 2015). Due to the short operating time, the annual emissions of NO<sub>x</sub> and PM from those generators are small. However, DR programs usually take place during hazy, hot and humid summer days. As a consequence, the emissions of diesel backup generators participating in DR programs may contribute to regional ozone pollution and local PM hotspots (Zhang and Zhang, 2015).

To evaluate the local air quality impact of distributed generation in urban neighborhoods, it is necessary to accurately simulate plume dispersion in microenvironments where exhaust momentum/buoyancy, surrounding structures and micrometeorology play significant roles. Gaussian plume models are commonly used

to evaluate local air quality. However, these models cannot explicitly resolve the complex flow field generated by near-source structures such as street canyons (Gilmore et al., 2006; Blocken et al., 2008), which can significantly modify plume dispersion (Robins and Castro, 1977). Computational fluid dynamics (CFD) models, on the other hand, are more capable of capturing the complex unsteady fluid dynamics and dispersion, but at a higher computing cost. Large Eddy Simulation (LES) is employed for modeling turbulent flow and dispersion in this study. It is an appropriate model for the purpose of our study as it resolves the large-scale unsteady motions and requires modeling only the small-scale, unresolvable turbulent motion, which is less influenced by the physical boundary conditions (Xie and Castro, 2006). Several LES studies were conducted on real urban geometry, and general modeling guidelines were developed (Tseng et al., 2006; Tamura, 2008; Gousseau et al., 2011). It is found that thermal stratification resulted from atmospheric stability critically affects near-surface concentrations of pollutants (Sini et al., 1996; Wood and Jarvl, 2012). Therefore, site-specific boundary layer parameters such as friction velocity, stability length, and sensible heat flux need to be assessed for micro-environmental plume dispersion studies.

To evaluate the local air quality impact of distributed generation in urban neighborhoods, it is necessary to accurately simulate plume dispersion in microenvironments where exhaust momentum/buoyancy, surrounding structures and micrometeorology play significant roles. Gaussian plume models are commonly used to evaluate local air quality. However, these models cannot explicitly resolve the complex flow field generated by near-source structures such as street canyon (Gilmore

et al., 2006; Blocken et al., 2008a). The plume dispersion can be significantly modified by the presence of structures in the vicinity of the source (Robins and Castro, 1977). Computational fluid dynamics (CFD) models, on the other hand, are more capable of capturing the complex unsteady fluid dynamics and dispersion, but at a higher computing cost. Large Eddy Simulation (LES) is employed for modeling turbulent flow and dispersion in this study. It is an appropriate model for the purpose of our study as it resolves the large-scale unsteady motions and requires modeling only the small-scale, unresolvable turbulent motion, which is less influenced by the physical boundary conditions (Xie and Castro, 2006). Several LES studies were conducted on real urban geometry, and general modeling guidelines are given (Tseng et al., 2006; Tamura, 2008; Xie and Castro, 2009; Gousseau et al., 2011). In addition to flow and dispersion, it is found in the literature that thermal stratification resulted from atmospheric stability condition critically affects near-surface concentration of pollutants (Sini et al., 1996; Wood and Jarvi, 2012). Therefore, site-specific boundary layer parameters such as friction velocity, stability length, and sensible heat flux need to be assessed for micro-environmental plume dispersion studies.

The first objective of this study is to introduce an improved approach to simulate spatial variations of pollutants in a near-source urban microenvironment by employing a meteorology processor AERMET to generate site-specific boundary layer parameters as boundary conditions (USEPA, 2004a). This enhances the modeling capability in resolving micro-scale air quality at urban neighborhood-scale (Steffens et al., 2012; Tong et al., 2012; Wang et al., 2013a). The second objective is to evaluate the environmental impact of diesel backup generators in near-source

microenvironments. The first part of the paper focuses on evaluating the interactions of plume dispersion and building downwash against existing wind tunnel experiments. The second part presents case studies to quantitatively evaluate the local impacts of NO<sub>x</sub> and PM<sub>2.5</sub> emissions from diesel backup generators. A series of LES simulations are conducted under various atmospheric stability conditions and urban configurations.

## 4.2. Model Description

The Comprehensive Turbulent Aerosol Dynamics and Gas Chemistry (CTAG) model contains the functionality to resolve the flow field including turbulent reacting flows, aerosol dynamics, and gas chemistry in complex urban environments. In this paper, we expand the existing CTAG model by incorporating the micrometeorology component in order to simulate thermal stratification and buoyancy effect that strongly influence the plume dispersion in microenvironments (Section 4.1). A full description of the model's theoretical background and implementation is presented in our previous work (Wang and Zhang, 2009a; Wang et al., 2011b; Steffens et al., 2012; Tong et al., 2012; Wang et al., 2012b; Wang and Zhang, 2012; Steffens et al., 2013; Steffens et al., 2014). A short description is presented here. LES is employed to resolve the unsteady turbulent flow field. In LES, a low-pass filtering operation is performed so that the resulting velocity field  $\tilde{u}_i$  can be resolved on a relatively coarse grid. A dynamic subgrid model is chosen, which allows the Smagorinsky constant to vary in space and time (Germano et al., 1991). The constant is dynamically computed based on the information provided by the resolved scales of motion. Logarithmic wall function is

applied to the near-wall region as it is computationally impractical to resolve every viscous sublayer in the domain of this size(Launer and Spalding, 1974). Turbulence at urban environment is dominated by large-scale motion generated by scales comparable to the size of buildings and street canyons(Xie et al., 2008; Xie and Castro, 2009). Capturing the precise surface drag of each building surface is exceedingly expensive.

#### 4.2.1 Governing Equation

In this chapter, the momentum, energy, and species transport equations employed in the CTAG model are described. In Large Eddy Simulation (LES), the filtered continuity and momentum equation are shown below.

$$\frac{\partial \rho}{\partial t} + \frac{\partial \rho \tilde{u}_j}{\partial x_j} = 0 \quad (11)$$

$$\frac{\partial \rho \tilde{u}_i}{\partial t} + \frac{\partial \rho \tilde{u}_i \tilde{u}_j}{\partial x_j} = -\frac{\partial \tilde{p}}{\partial x_i} + \frac{\partial \tau_{ij}}{\partial x_j} + \frac{\partial \sigma_{ij}}{\partial x_j} \quad (12)$$

SGS Reynolds stress are modeled by Boussinesq hypothesis:

$$\sigma_{ij} - \frac{1}{3} \delta_{ij} \sigma_{kk} = -2\mu_t S_{ij} \quad (13)$$

Eddy viscosity is modeled by,

$$\mu_{sgs} = \rho(L_S)^2 |\bar{S}| \quad (14)$$

where  $L_S$  is the Smagorinsky(mixing length )scale and  $|\bar{S}| = \sqrt{2\bar{S}_{ij}\bar{S}_{ij}}$ .

$$L_S = C_s \Delta \quad (15)$$

$\Delta$  is the filtered width determined by the volume of the cell.  $C_s$  is the Smagorinsky constant.

$$\Delta = (Volume)^{\frac{1}{3}} \quad (16)$$

The energy equation is described below,

$$\frac{\partial \tilde{T}}{\partial t} + \frac{d\tilde{u}_j \tilde{T}}{dx_j} = \frac{\partial}{\partial x_j} \left[ (k_{eff}) \frac{\partial \tilde{T}}{\partial x_j} \right] \quad (17)$$

where  $\tilde{T}$  is the mean temperature,  $k_{eff}$  is the effective thermal diffusivity. For the size of the domain in this study, the pressure variation with elevation is insignificant. So the potential temperature is assumed to be the same as the absolute temperature.

Species transport equation is described below,

$$\frac{\partial \tilde{C}}{\partial t} + \frac{d\tilde{u}_j \tilde{C}}{dx_j} = \frac{\partial}{\partial x_j} \left[ \left( D_m + \frac{\mu_t}{Sc_t} \right) \frac{\partial \tilde{C}}{\partial x_j} \right] + S \quad (18)$$

where  $\tilde{C}$  is the mean concentration,  $Sc_t = \frac{\mu_t}{\rho D_t}$  is the turbulent Schmidt number,  $D_t$  is

the turbulent diffusivity, and  $D_m$  is the molecular diffusivity.  $S$  is the source or sink term.

### **4.3. Model Evaluations**

We evaluated the LES model against two wind tunnel datasets on turbulence flow and plume around surface-mounted cubes, respectively. The former is from ERCOFTAC (European Research Community on Flow, Turbulence and Combustion), and the latter is from EPA (Martinuzzi and Tropea, 1993; Thompson, 1993). The evaluations serve as a solid base for simulating plume dispersion in realistic urban environments.

#### **4.3.1 ERCOFTAC**

##### **4.3.1.1 Experiment**

For the flow field experiment from ERCOFTAC, the Reynolds number based on the cube height is  $\sim 40,000$ . The turbulent flow field around surface-mounted prismatic obstacles was characterized using the crystal violet, oil-film and laser-sheet visualization techniques. The experiment was performed in an open, blower-type air channel. The dimensions of the channel are 390 cm x 60cm x 5cm. The boundary layer was tripped at the inlet in order to obtain fully developed flow condition.

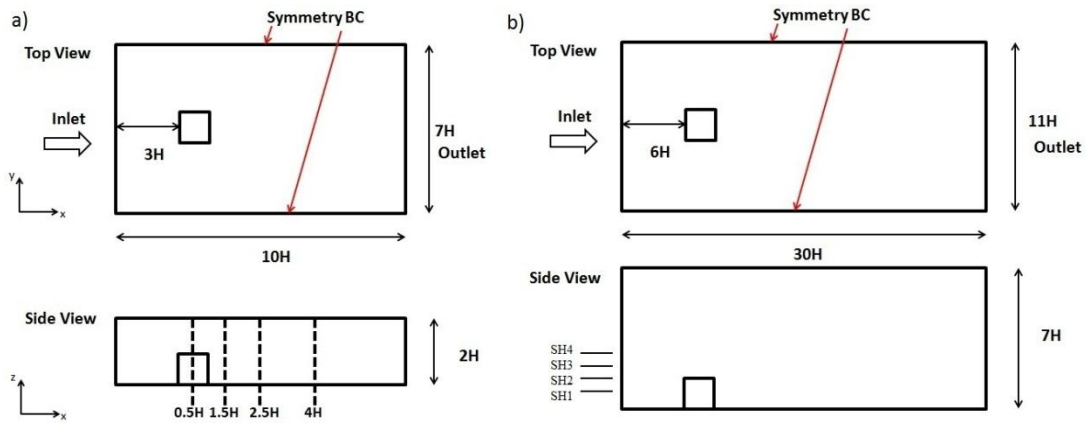


Figure 4.1: a) Schematic of the numerical setup for flow field evaluation b) Schematic of numerical setup for the plume dispersion evaluation. SH1(Stack Height) =75mm, SH2=150mm, SH3=225mm, SH4=300 mm. H is defined as the height of the cube.

#### 4.3.1.2 Simulation

The schematic drawing for the flow experiment is shown in Fig. 1a. The inlet boundary condition is obtained from the experimental measurement including mean flow and fluctuation components. The time-dependent feature of the inlet turbulence profile is simulated by the vortex method, where random vortices in the inlet flow plane for the wall-normal components are generated giving a spatial correlation (Mathey et al., 2006). Symmetry boundary conditions are applied for the two sides as slip walls with zero shear. Outflow boundary condition is specified at the end of the domain. The computational domain contains about 1.7 million cells. The grids are more refined near the solid cube and stack. Prism layer mesh is applied near the wall in order to reduce numerical diffusion.

### 4.3.1.3 Results

Figure 4.2 exhibits a comparison of the time-averaged streamwise flow velocity. In general, the LES model is adequate in capturing the flow field by comparing with experimental data. Slight discrepancies are observed at the cube wall ( $z/H=1$ ) and floor ( $z/H=0$ ) due to semi-empirical wall function employed.  $H$  is defined as the height of the cube. Figure 4.3 demonstrates a satisfactory agreement between the time-averaged velocity component in the streamwise direction in the symmetry plane at two different  $z/H$ , and the experimental results. The LES model generally captures the trend that the mean flow velocity decreases to zero at the building wall due to no-slip condition and gradually recovers to upstream velocity at about  $x/H=8$ . However, it is observed that the model overpredicts the negative mean velocity near the cube leeward face between  $x/H=4$  and 5.

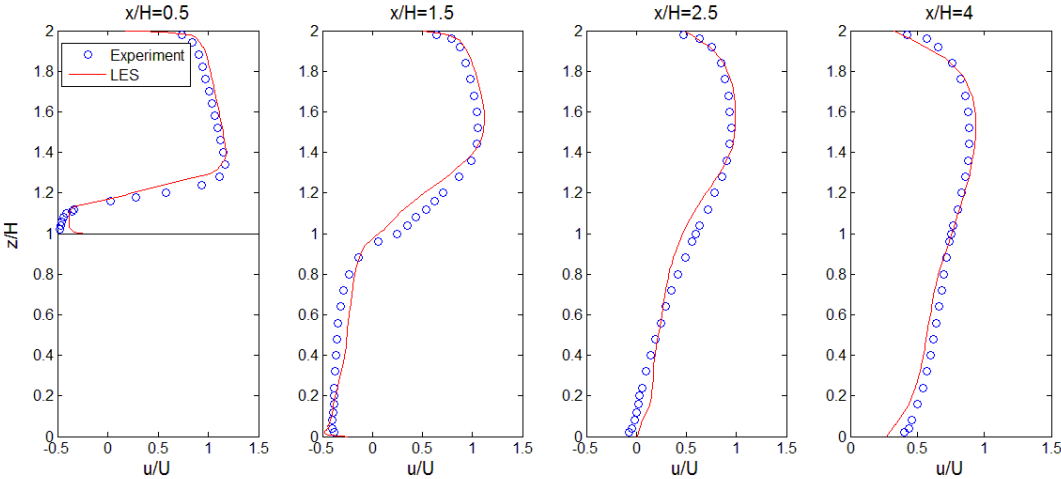


Figure 4.2: Time-averaged streamwise velocity profile at various  $x/H$  as indicated

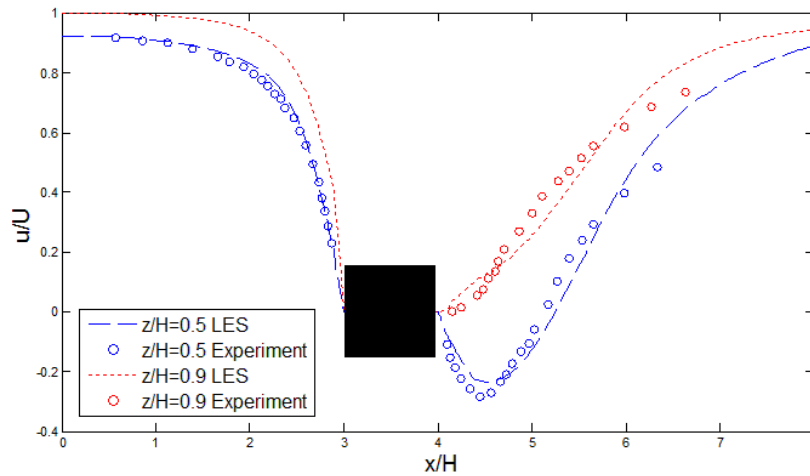


Figure 4.3: Streamwise velocity profile on the symmetry plane at two heights  $z/H=0.5, 0.9$ .

## 4.3.2 Plume Dispersion

### 4.3.2.1 Experiment

The plume dispersion data are obtained from a separate experiment from USEPA, which investigated how the aerodynamics around buildings with different stack heights (SH) influence the dispersion of pollutants. Two scaled building widths (15 cm and 60 cm) are chosen for evaluation as shown in Fig. 4. The experiment was conducted in the USEPA meteorological wind tunnel with a test section of 3.7 m (W)  $\times$  2.1 m (H)  $\times$  18 m (L). A neutral boundary layer was generated by tripping the flow with a high fence at the entrance. The Reynolds number based on the building height and the approaching flow velocity at the same height is  $\sim 32,400$ , which is well above the critical Reynolds number (Thompson, 1993). Tracers were released at different SHs both above and below the building height, and the ground-level concentrations along the tunnel centerline parallel to the flow direction were measured. However, the flow fields were not characterized. Concentrations and distances in the experiment

have been normalized in order to make appropriate comparisons between the scale model created in the wind tunnel and full scale, real-world scenarios. Distances have been normalized by the building height. Concentrations have been normalized according to the following formula,

$$\chi = \frac{CU_H H^2}{Q} \quad (19)$$

where  $H$  is the building height,  $U_H$  is the approach flow wind speed at the building height, and  $Q$  is the source emission rate.

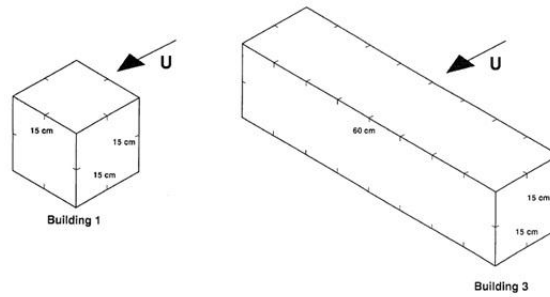


Figure 4.4: Schematics of the building used in the plume dispersion experiment. Left: 15 cm building; Right: 60 cm building

#### 4.3.2.2 Simulation

The schematic drawing for the plume dispersion experiment is shown in Figure 4.4b. The locations of inlet, outlet and symmetry boundary conditions are the similar to the ERCOFTAC simulation except the 4 SHs (75, 150, 225, 300mm above the floor) at the inlet wall where the plume was released. Zero diffusive flux is applied to every other solid wall. The size of the computational domain for each case range contains 2.2 million cells. The grids are more refined near the solid cube and stack.

Prism layer mesh is applied near the wall in order to reduce numerical diffusion.

### 4.3.2.3 Results

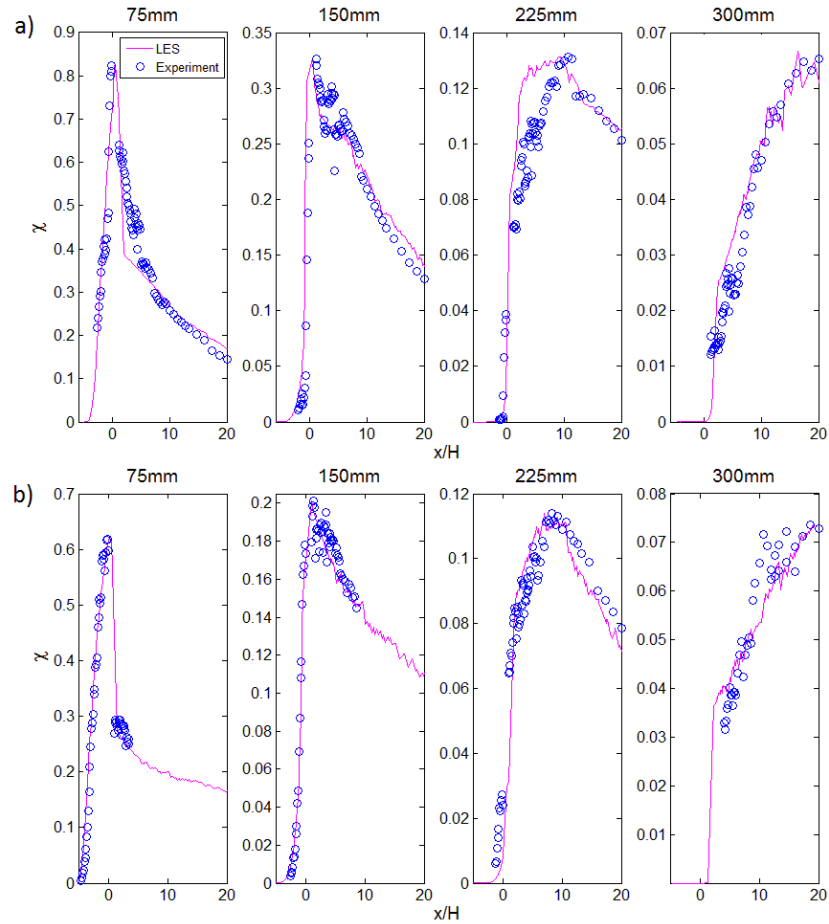


Figure 4.5: a) Normalized ground-level centerline concentration ( $\chi$ ) for 15cm building at SH=75, 150, 225, 300 mm; b) Normalized ground-level centerline concentration ( $\chi$ ) for 60cm building at SH=75, 150, 225, 300 mm

Figure 4.5 compares the predicted and simulated tracer concentration with measurement for 15cm and 60cm buildings along the centerline of the domain.  $x/H=0$  is at the windward face of the cube. Overall, the LES model adequately captures the general trends and peak concentrations. The performance of LES is satisfactory at 4 SHs, although the model overpredicts the centerline concentration prior to the peak

location for the 15cm building for the SH=225mm case.

#### **4.4. Diesel Backup Generator Case Studies**

##### **4.4.1 Numerical Setup**

To evaluate local air quality impacts due to emissions from diesel backup generators, the size of the modeling domain needs to be sufficiently large to include nearby buildings and other structures. The height of the domain should be tall enough to account for plume rise, and avoid any blocking effect and unphysical flow acceleration (Tominaga et al., 2008). Fig. 6 shows the modeling domains. The baseline building (i.e., where the backup generator is housed) and stack parameters are based on a realistic urban area in New York City. The size of the domain is about  $1,200 \times 1,000 \times 150$  m. It is meshed with 4.5 million unstructured elements with prism layers near the wall. Grid independency study is conducted to ensure the results are independent of the mesh resolution.

Vertical wind and temperature profiles ( $>100$  m) are usually unavailable for most cities. On the other hand, the quality of microscale simulation relies on those profiles specified at the boundaries (Tominaga et al., 2008). Therefore, a realistic estimation of inflow profiles becomes critical for LES simulations at this scale. Domain of this size locates in the surface layer of planetary boundary layer, which is amenable to Monin-Obukhov similarity theory employed in this study (Monin and Obukhov, 1954). Thus, a semi-empirical approach is introduced here based on local weather station and Monin-Obukhov similarity theory. A meteorological processor, AERMET, developed by EPA is employed in our study (USEPA, 2004b; Cimorelli et al., 2005). The friction velocity ( $u^*$ ) and Monin-Obukhov length ( $L$ ) are computed

from the quadratic solution for stable condition, and iterative method for unstable condition (Perry, 1992; Hanna and Chang, 1993). Sensible heat flux ( $H$ ) is estimated based on energy balance approach developed by Oke (1988). Hourly surface data are obtained from the weather station at LaGuardia Airport, and upper air data from Brookhaven, NY. Surface characteristics at a resolution of 1 km including surface roughness length  $z_0$ , albedo, and Bowen ratio are computed using AERSURFACE developed by USEPA, which extracts data from U. S. Geological Survey (USGS) National Land Cover Data archives (USEPA, 2008). An in-house script is developed to generate inflow profiles for LES simulations based on Monin-Obukhov similarity theory, and boundary layer parameters from AERMET ( $u^*$ ,  $L$ ,  $H$ , and  $z_0$ ). The details is described as following.

The wind velocity and temperature profiles are determined based on Monin-Obukhov similarity theory shown in Eqn 20 and 21,

$$\frac{U}{u^*} = \frac{1}{k} \left[ \ln \left( \frac{z}{z_0} \right) - \psi_m \left( \frac{z}{L} \right) \right] \quad (20)$$

$$\frac{T - T_0}{T_*} = \frac{1}{k} \left[ \ln \frac{z}{z_0} - \psi_h \left( \frac{z}{L} \right) \right] \quad (21)$$

where  $\frac{z}{L}$  is the non-dimensional height.  $\psi_m$  and  $\psi_h$  are similarity functions.  $T_*$  is the temperature scale that is determined in Eqn 26.  $T_0$  is the reference temperature at measurement height.

The similarity function  $\psi_m$  and  $\psi_h$  in Eqn 20 and 21 can be determined from the well-

known *Businger-Dyer* relationships, which is recommended for most practical application (Businger et al., 1971; Arya, 2001).

Stable condition:

$$\psi_m = \psi_h = -5 \frac{z}{L} \quad \text{for } \frac{z}{L} \geq 0 \quad (22)$$

Unstable condition:

$$\psi_m = \ln \left[ \left( \frac{1+x^2}{2} \right) \left( \frac{1+x}{2} \right)^2 \right] - \tan^{-1} x + \frac{\pi}{2} \quad \text{for } \frac{z}{L} < 0 \quad (23)$$

$$\psi_h = 2 \ln \frac{1+x^2}{2} \quad \text{for } \frac{z}{L} < 0 \quad (24)$$

where

$$x = (1 - 15 z/L)^{0.25}.$$

Neutral condition:

$$\psi_m = \psi_h = 0 \quad (25)$$

The temperature scale in Eqn 21 can be determined from sensible heat flux  $H$  and friction velocity as following,

$$T_* = - \frac{H}{\rho c_p u_*} \quad (26)$$

where  $c_p$  is the specific heat at given pressure, and  $\rho$  is the density of air. In order to estimate of  $H$ , simple parameterizations are made based on energy balance approach (Oke, 1978).

$$H = \frac{0.9R_n}{1 + 1/B_0} \quad (27)$$

where  $R_n$  is the net radiation, and  $B_0$  is the Bowen ratio, which are determined from the USGS National Land Cover Data archives .

Large Eddy Simulation of spatially developing flows usually requires the specification of time dependent inflow conditions. The mean turbulence profile, turbulent kinetic energy (TKE) and its dissipation rate, in atmospheric surface layer, are approximated by

$$TKE = \frac{(u^*)^2}{\sqrt{C_\mu}} \quad (28)$$

$$\epsilon = \frac{(u^*)^3}{k(z_0 + z)} \quad (29)$$

where  $k = 0.42$  , and  $C_\mu = 0.013$ ,  $z_0$  is surface roughness height (Richards and Hoxey, 1993). The time-dependent feature is simulated, where random vortices in the inlet flow plane for the wall-normal components are generated giving a spatial correlation (Mathey et al., 2006).

The fully developed wind velocity and temperature profiles are applied at the

west boundary as inlet, which is the dominant wind direction and there are multiple street canyons downwind of the stack. Symmetry boundary condition is applied on the north and south side boundaries as slip walls with zero shear. At the flow outlet (east boundary), zero diffusion flux of all flow variables is specified. Directly simulating heat transfer from ground and buildings with LES requires resolving the thermal layer at every building surface, which is very expensive, and there is no thermal-wall model available yet (Xie et al., 2013). Thus, an alternative approach is employed. AERMET is used to compute thermally stratified approaching flow for the entire site. The computed profiles are then applied at the inlet boundary of the modeling domain. At the building and ground surfaces, adiabatic and no-slip condition are applied.

Exhaust particles in diesel backup generator emissions mostly constitute of those less than  $1\ \mu\text{m}$  (USEPA, 2006). The volume fraction of the particulate phase is low, and submicron particles have small relaxation time, which are able to closely follow the fluid streamline. Therefore, the flow falls into the dilute gas-solid flow regime. In addition, we treat primary  $\text{PM}_{2.5}$  as a tracer species, i.e., assuming that gas/particle partitioning near stacks will not significant change the primary  $\text{PM}_{2.5}$  mass near the sources. This assumption is subject to future investigation. Thereby, both  $\text{NO}_x$  and  $\text{PM}_{2.5}$  concentration field are solved by convection-diffusion equation. Surface deposition of  $\text{PM}_{2.5}$  at building surface is accounted for by imposing a mass flux based on mass-weighted deposition velocity from the literature (Petroff and Zhang, 2010). Deposition flux is applied on the every building surface as shown Equation 30. This is implemented as customized boundary condition.

$$J = V_d C \tag{30}$$

C is the particle concentration at the cell adjacent to the surface. The deposition velocity  $V_d$  for smooth surface is taken from the model by Petroff and Zhang (2010). A typical diesel mass-based particle size distribution is assumed to derive the mass-weighted deposition velocity for  $PM_{2.5}$  (Abdul-Khalek et al., 1999). In this study, the mass-weighted deposition velocity for  $PM_{2.5}$  (Abdul-Khalek et al., 1999). In this study, the mass-weighted deposition velocity  $V_d$  is equal to 0.0036 cm/s. In the modeling domain, diesel backup generator is treated as the only source, and no background concentration is considered.

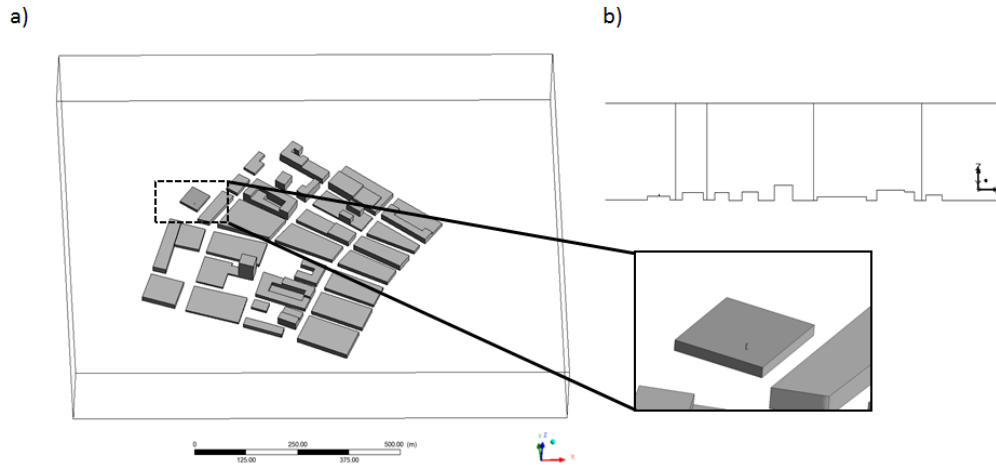


Figure 4.6: a) Geometry of the diesel backup generator site, b) Cut plane that intersects the stack and parallel to  $xz$  plane. Vertical lines that are 30, 100, 300, 500m downwind from the stack are shown.

#### 4.4.2 Stack Parameters

The diesel backup generators are typically installed in the basements, and their exhaust stacks are located on the rooftops. The exhaust stack is designed to be

sufficiently far from the fresh air intake of the same building housing the diesel backup generator. The rooftop stacks of diesel backup generators are typically much shorter than the ones installed for power plants due to aesthetics and local building code (Carter et al., 2005; Porter; Lomas, 2007). We create a baseline case, where a 3.1m rooftop stack is located on a two-story building upwind of several street canyons. The stack height is above the roof recirculation zone estimated by ASHRAE in order to avoid plume entrainment on the rooftop (ASHRAE, 2003). The parameters for a typical rooftop diesel backup generator stack are shown in Figure 4.1. Diesel backup generators are able to reach full load within 10 seconds (Wroblewska, 2011). Thus only steady-state stack parameters are considered. Both NO<sub>x</sub> and primary PM<sub>2.5</sub> emission factor are estimated from the mix of Tier 1, Tier 2, and Pre-Tier diesel generators. Two generator sizes (500 kW and 1,000 kW) are tested in this study.

Table 4.1: Stack, meteorology, and building parameters for a 1000 kW diesel backup generator at steady-state operation

<b>Parameters</b>	<b>Values</b>	<b>References</b>
Exhaust velocity	15 m/s	Petersen et al. (2002)
Exhaust temperature	650 K	Caterpillar
Stack Height	3.1m from rooftop	Petersen et al. (2002)
Stack Inside Diameter	0.77 m	Petersen et al. (2002)
NO <sub>x</sub> Emission	10.6 g/kWh	Zhang and Zhang (2015)
PM <sub>2.5</sub> Emission	0.5 g/kWh	Greene and Hammerschlag, 2000, Gilmore et al., 2006 and USEPA, 2004b
Emission Standard	Mix of Tier 1,2 and Pre-Tier	Zhang and Zhang (2015)
Stability	Unstable, neutral, stable	N/A
Building Configuration	4 cases shown in Fig. 8	N/A

### 4.4.3 Results and Discussions

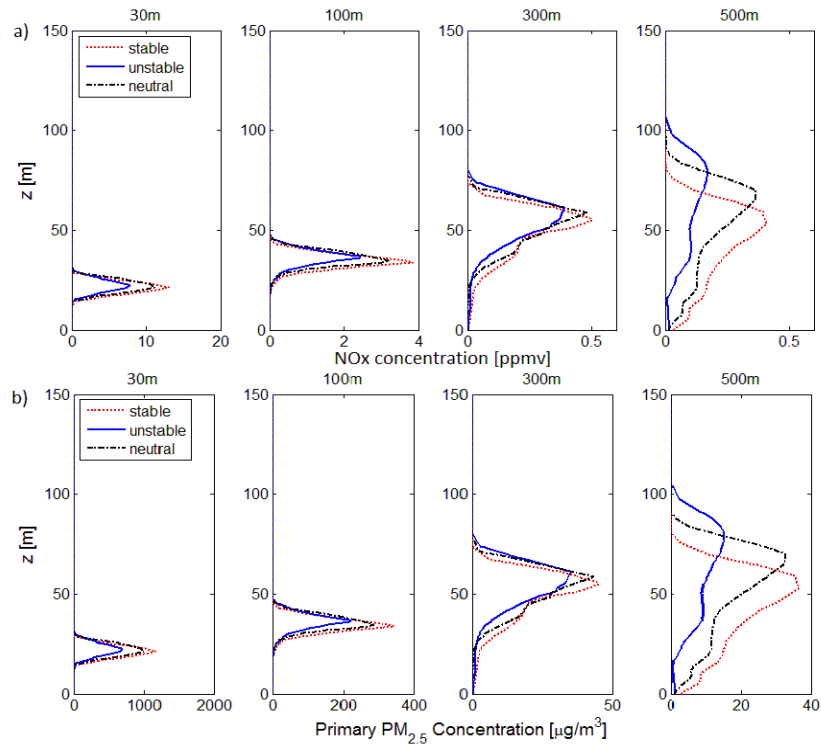


Figure 4.7: a) Vertical profiles of NOx concentration of backup diesel generator in ppmv b) Vertical profiles of PM<sup>2.5</sup> concentration of backup diesel generator in μg/m<sup>3</sup> at 30m, 100m, 300m, and 500m away from the stack

The vertical profiles of NOx concentration (ppmv) are shown in Figure 4.7a. The corresponding weather data are chosen from hours under different stability classes in July, 2013. The concentration profiles give a general idea of the plume trajectory as a function of distance and stability. The atmospheric stability plays an important role in plume dispersion. The unstable condition results in the highest plume trajectory and effective stack height because of the vertical movement of air parcels, and the additional buoyance created by thermal stratification. In comparison, the stable

condition leads to significantly lower plume trajectory and buoyance because it resists vertical mixing. The trajectory of neutral condition stays in between stable and unstable conditions.

At 30m from the stack, peak concentrations of NO<sub>x</sub> for three stability classes are in the range from 7 to 10 ppmv, and decrease below 0.5 ppmv at 500m downwind. The peak primary PM<sub>2.5</sub> concentrations of the three stability classes reaches the range between 600 and 1,100 μg m<sup>-3</sup> at 30m downwind (z~18 m) of the stack, and dilute to 15~40 μg m<sup>-3</sup> range at 500m. More vertical dispersion and near-ground impacts are observed at x=300, 500m as the plume travels downwind shown in Figure 4.7b.

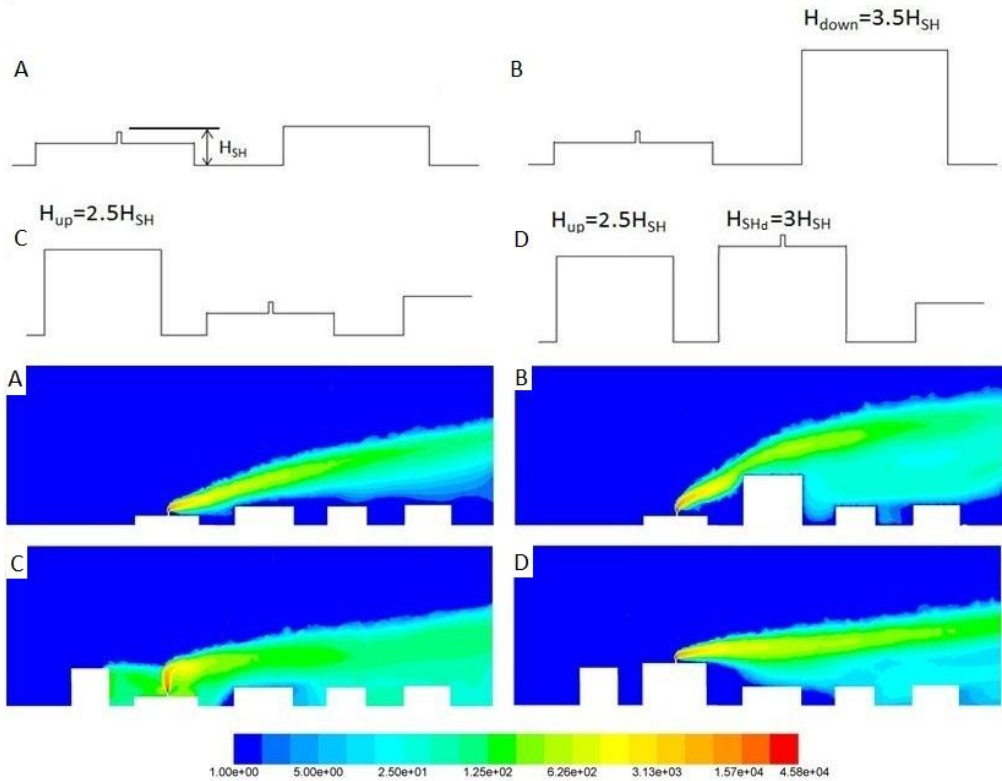


Figure 4.8: Schematics of 4 configurations and corresponding contour plots of primary PM<sub>2.5</sub> concentration in μg m<sup>-3</sup>. Case A is the baseline configuration.

Surrounding street canyon configurations play an important role on near-stack plume dispersion. For further investigations, three additional configurations are created to compare against the baseline (Case A). Case B represents the condition where the adjacent downwind building is significantly taller ( $3.5H_{SH}$ ) than the backup generator building, where  $H_{SH}$  is the sum of height of the baseline backup generator building and stack height. Case C is the condition with a tall building upwind of the stack ( $2.5H_{SH}$ ), which creates a recirculation zone between the upwind and downwind building of the stack. Case D presents a scenario where the upwind and downwind buildings are the same as Case C, but the new backup generator building is taller than the upwind building and outside the recirculation zone ( $3xH_{SH}$ ). The rest of the stack parameters are the same for all four cases.

We have evaluated the hours (typically in the afternoons) when NYISO emergency-based DR programs were called from 2011 to 2013 (NYISO, 2013). Unstable atmospheric conditions are found to persist for every DR event hour during this period. The specific boundary meteorological conditions used in our simulations are determined based on a particular hour representing the median temperature (i.e., 34 °C) of all DR event hours on July 18, 2013. The wind velocity at the reference height was about  $4 \text{ m s}^{-1}$ . Figure 4.8 displays the contour plots of primary  $\text{PM}_{2.5}$  concentration for each configuration within 200m from the stack. A contour plot of the entire domain for Case C is shown in Figure 4.9.

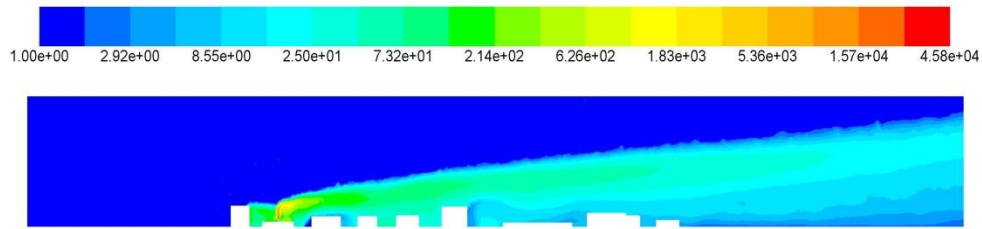


Figure 4.9: Contour plots of  $PM_{2.5}$  concentration in  $\mu\text{g}/\text{m}^3$  for Case C

At the baseline configuration (Case A), no near-ground concentration in the adjacent street canyons is observed due to sufficient  $H_{SH}$  and the unstable atmosphere that enhances vertical dispersion. The plume rises higher above the ground as it travels downwind. In Case B, the plume trajectory is pushed higher than the baseline case due to the upward flow deflection near the windward wall. The tall downwind building creates a large recirculation zone behind it. The resulting wake zone behind the building slows down the mean flow and creates a well-mixed region, which elevates the near-ground concentration. For Case C, the stack is located inside the recirculation zone generated by the tall upwind building. In this wake zone, the stack plume is drawn downward and sideways, which considerably reduces near-stack dilution. This building downwash effect of the plume significantly raises the primary  $PM_{2.5}$  concentration above  $200 \mu\text{g m}^{-3}$  inside the canyon between the upwind and downwind building. In Case D, the building downwash of the plume between the upwind and downwind building is substantially reduced by locating the stack outside the recirculation zone. However, the primary  $PM_{2.5}$  concentration in the street canyons further downwind of the stack is still around  $20 \mu\text{g m}^{-3}$  due to the large wake zone created by the tall diesel backup generator building.

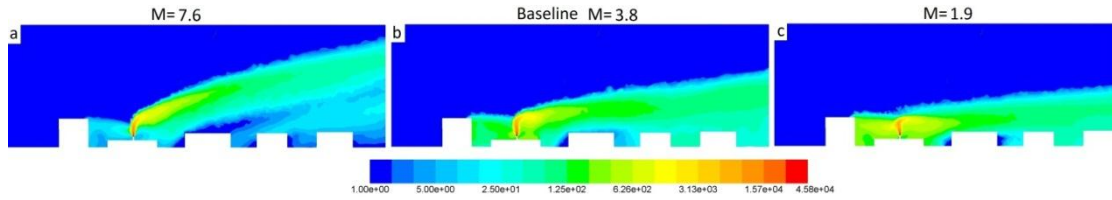


Figure 4.10: Contour plots of primary  $\text{PM}_{2.5}$  concentration in  $\mu\text{g}/\text{m}^3$  for three exhaust momentum ratio  $M$  (=stack exit velocity /ambient wind velocity) indicated. Stack exit velocity is kept constant for three cases.  $M=3.8$  from Case C is employed as a new baseline for comparison. Ambient wind velocity for the  $M=7.6$  case is  $2 \text{ m s}^{-1}$ , and  $8 \text{ m s}^{-1}$  for the  $M=1.9$  case.

In order to understand the effects of ambient wind velocity on plume dispersion, we conduct a sensitivity study on the upcoming wind speed using the configuration in Case C, as it creates the most downwash effect among the four configurations illustrated in Figure 9. The exhaust momentum ratio  $M$  (=stack exit velocity /ambient wind velocity) is employed here for the three test cases shown in Figure 4.10 (Petersen et al., 2002; Blocken et al., 2008).  $M=3.8$  from Case C is chosen as a new baseline for comparison. Comparing the three ratios, it is evident that decreasing  $M$  reduces the downwind vertical mixing of the plume, and causes the plume to travel closer to the ground level. As a result, it leads to lower effective stack height and elevated pollutant concentrations in the downwind street canyons. When  $M$  is increased to 7.6, the primary  $\text{PM}_{2.5}$  concentration inside the street canyon ranges from 0 to  $30 \mu\text{g m}^{-3}$ . When  $M$  decreases to 1.9, the bulk  $\text{PM}_{2.5}$  concentration inside the street canyon increases significantly to over  $200 \mu\text{g m}^{-3}$  as the plume is pulled more downward into the recirculation zone. Since the stack is located inside the wake zone created by the upwind building, increasing ambient wind velocity does not enhance

the near-stack dilution.

The environmental impact of a smaller 500 kW diesel backup generator is also evaluated for Case C. The same emission factor for PM<sub>2.5</sub> presented in Table 4.1 is used. All other stack parameters are the same except slightly greater exhaust temperature (Caterpillar). The contour plot of the primary PM<sub>2.5</sub> concentration for the 500 kW backup generator is shown in Figure 4.11. The plume dispersion patterns are similar to 1000 kW case. Lower near-ground concentration in the downwind street canyons is observed.

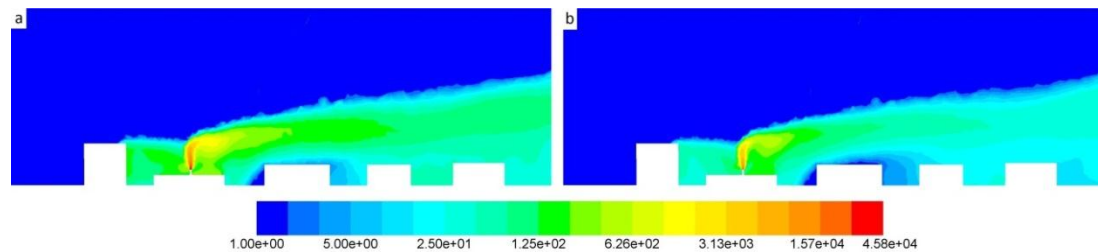


Figure 4.11: Primary PM<sub>2.5</sub> concentration contour plots ( $\mu\text{g m}^{-3}$ ) of Case C for a) 1000 kW diesel backup generator b) 500 kW diesel backup generator

The latest USEPA Tier 4 emission standards for stationary diesel engine were implemented in 2014(USEPA, 2004a). The emission rates are significantly reduced than the ones in Table 4.1. NO<sub>x</sub> emission factor is  $2.16 \text{ g kWh}^{-1}$ , and PM<sub>2.5</sub> emission factor is  $0.04 \text{ g kWh}^{-1}$ , which are almost 5 and 12 times less than the ones from Tier 1 and older, respectively (Zhang and Zhang, 2015). Based on these emission factors, Case C is re-simulated shown in Figure 4.12. Reduced NO<sub>x</sub> concentration in the street canyon between upwind and downwind building is around 30 ppbv. Primary PM<sub>2.5</sub> concentration is decreased below  $30 \mu\text{g m}^{-3}$  inside the street canyon. Although the

reduction is significant, the near-source impact is still not negligible during operation hours.

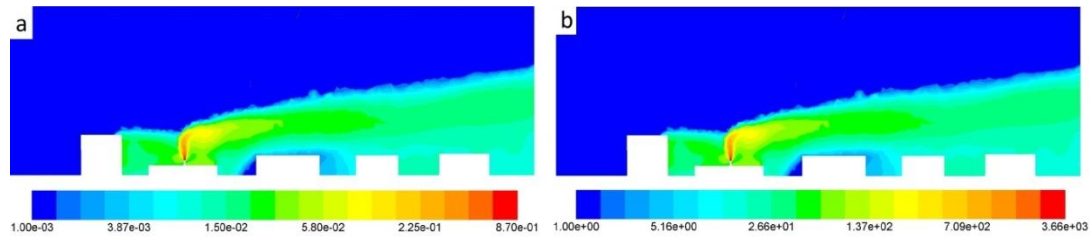


Figure 4.12: Contour plot of a) NO<sub>x</sub> concentration in ppmv and b) PM<sub>2.5</sub> concentration  $\mu\text{g m}^{-3}$  based on Tier 4 standards based a 1000 kW diesel backup generator

#### 4.5. Conclusion

Backup diesel generators are often allowed to participate in demand response (DR) programs during peak demand periods. In this study, we investigate the spatial variations of air pollutants near a diesel backup generator stack by employing an improved approach for micro environmental simulations, in which a meteorology processor AERMET is adopted to generate site-specific boundary layer parameters. According to our analysis, the near-source air quality impacts of diesel backup generator emissions depend strongly on urban configurations and meteorological conditions. We analyze four street canyon configurations. The worst-case scenario is identified (Case C in Fig. 9) where the stack is located inside the recirculation zone created by a tall upwind building. In this case, the plume is drawn downward and sideways, reducing the near-stack dispersion and leading to elevated concentration inside adjacent street canyon. The near-source PM<sub>2.5</sub> concentration could well exceed  $100 \mu\text{g m}^{-3}$  even under unstable atmospheric conditions (i.e., the conditions when DR events are called). In Case B (with a tall downwind building) and Case D (with the

backup generator building taller than surrounding buildings), the concentrations in the street canyon immediately adjacent to the stack are small, but elevated primary PM<sub>2.5</sub> concentrations appear in street canyons further downwind. Decreasing the exhaust momentum ratio (i.e., stack exit velocity/ambient wind velocity) draws more plumes into the recirculation zone, and reduces the effective stack height, which results in an elevated near-ground concentration inside downwind street canyons. Based on our study, the stack location should be carefully selected based on the surrounding environment for backup generators participating in DR programs. Otherwise, the environmental impact could potentially become an unintended consequence of DR programs, as they are traditionally perceived as clean resources for power systems.

## Chapter 5

### **Microenvironmental Air Quality Impact of a Biomass Boiler With and Without PM Emission Control**

#### **Abstract**

Initiatives to displace petroleum and climate change mitigation have driven a recent increase in space heating with biomass combustion in New York State and elsewhere in the Northeast. However, there is ample evidence that biomass combustion emits significant quantities of known health damaging pollutants. We investigated the micro-environmental air quality impact of a biomass-fueled combined heat and power system equipped with an electrostatic precipitator (ESP) in Syracuse, NY. Emission factors are derived based on in-stack measurement both upstream and downstream of ESP with EPA Method 5/202. In tandem with the stack testing, two rooftop stations with PM<sub>2.5</sub> and CO<sub>2</sub> analyzers were set up in the way that one can capture the plume while the other one serves as the background in comparison depending on the wind direction. Four sonic anemometers were deployed around the stack to quantify highly spatially and temporally resolved local wind pattern. A computational fluid dynamic-based micro-environmental model was applied to simulate the experimental conditions, and a good agreement between predicted and on-site measurement is observed for both flow fields and plume dispersion. Our analysis shows that the absence of ESP could lead to an almost 7 times increase in near-ground PM<sub>2.5</sub>

concentrations with a maximum concentration  $>50 \mu\text{g m}^{-3}$  in the surrounding environment. This result demonstrates the critical role of air pollution controls for biomass combustion systems. In addition, we explored various physical parameters including stack temperature/height, ambient wind, and surrounding structures to provide recommendations for siting biomass-fueled heating equipment in order to minimize local air pollution.

## **5.1. Introduction**

Of all the renewable energy resources, biomass is plentiful and prominent. Recently, initiatives to displace petroleum and climate change mitigation have driven a recent increase in space heating with biomass combustion in New York State and elsewhere in the Northeast. However, biomass combustion is a major source of primary  $\text{PM}_{2.5}$  emission, and many studies have shown elevated exposure to particulate matter is associated with many adverse health diseases (Dockery et al., 1993). Many researchers have investigated various environmental aspects of biomass burning (Ndiema et al., 1998; Boman et al., 2003; Wang et al., 2011a). Fewer studies have looked at the local air quality impact which is strongly linked with human health. The objective of this study is to quantify the micro-environmental impact of biomass combustion in a complex urban area. We first evaluated our model performance against on-site aerodynamic and air quality measurement. Second, we applied the model to evaluate the nearby air quality with and without ESP. Third, we explored various physical parameters including stack temperature/height, ambient wind, and surrounding structures to provide recommendations for siting biomass-fueled heating equipment in order to minimize local air pollution.

## 5.2. Experimental Approach

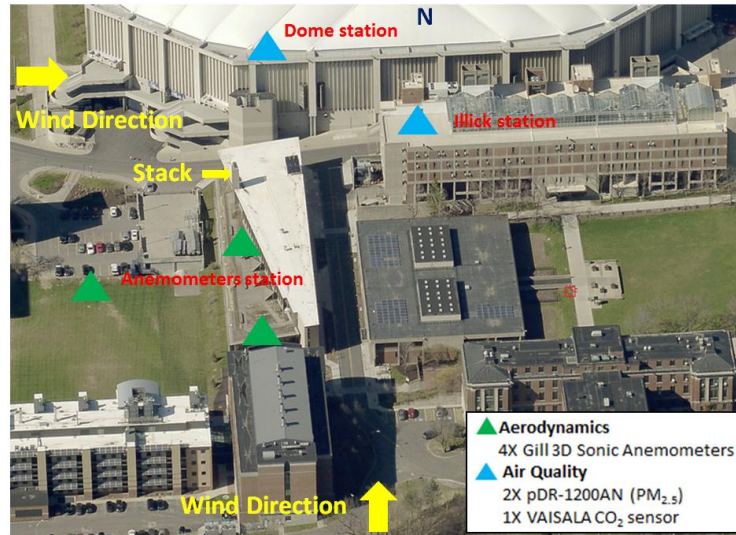


Figure 5.1: Satellite image of the site overlaid with flow field and air quality sampling details. The position of triangles indicates the relative position of each sampling stations.

### 5.2.1 Site Description

The Combined Heat and Power (CHP) facility with a wood pellet-fired boiler and an electrostatic precipitator (ESP) is located in the Gateway Building on the campus of SUNY College of Environmental Science and Forestry (ESF) in Syracuse, NY. Even though the Gateway Building is located in an academic setting, the nearby structures including the Carrier Dome and Illick Hall make the surrounding area a good representation of an urban environment (Figure 5.1). The exhaust stack is on the rooftop of Gateway building about 16m from the ground level, which is surrounded by Carrier Dome (42m) and Illick Hall (26m). The presence of the two tall buildings with accessible rooftop area allows us to set up measurement stations that are able to capture the near-source stack plume. Other buildings are located further from the stack with lower heights as shown in Figure 5.1.

### **5.2.2 Instrumentation**

Two personal DataRam (pDR-1200, Thermo Scientific, Boston, MA, USA) were used in combination with a PM<sub>2.5</sub> size-selective cyclone to continuously collect data every 6 second. One CO<sub>2</sub> sensor (MI70, VAISALA, Finland) and one CO sensor (IAQ-CALC, TSI Model 7545) were employed at 30 second sampling interval in combination with PM<sub>2.5</sub> measurement to detect concurring concentration spikes at the Illick station. Three 3-D Gill sonic anemometers were strategically deployed to measure the instantaneous wind speed and direction at 1 Hz. Before the field trip, two pDRs were cross-calibrated by co-locating them next to a traffic source to rectify any systematic differences between them. Three anemometers were cross-calibrated in an environmental wind tunnel to ensure consistency among them.

### **5.2.3 Sampling Location**

Two rooftop sampling stations (Carrier Dome and Illick station) were set up in the way that one can capture the plume while the other one serves as the background in comparison depending on the wind direction. At the Carrier Dome station, the pDR was placed on south edge facing the biomass stack (Figure 5.1). At the Illick station, pDR and CO/CO<sub>2</sub> sensor were placed near the west edge of the roof facing the stack (Figure 5.1). All instruments were raised vertically away from the floor by a table in order to avoid boundary layer effect. The placement of the three anemometers designed according to the prevailing wind direction (West). One was installed upwind of the Gateway building 4.3m from the ground level. The second one was installed at the green roof level of the Gateway building 2.5m from the floor. The third one is

placed outside the south exit of the Gateway building 2.6m from the floor. The field trip was conducted at the same time with the scheduled stack testing (EPA Method 5/202) on Mar 18 and 19 2015, lasting two days, ca. 10 hours each day during the daytime.

### **5.3. Numerical Setup**

The Comprehensive Turbulent Aerosol Dynamics and Gas Chemistry (CTAG) model is designed to resolve the flow field including turbulent reacting flows, aerosol dynamics, and gas chemistry in complex urban environments. A full description of the model's theoretical background and implementation is presented in our previous work (Wang and Zhang, 2009b; Wang et al., 2011b; Steffens et al., 2012; Tong et al., 2012; Steffens et al., 2013; Wang et al., 2013a; Tong and Zhang, 2015). In particular, a similar methodology was applied to simulate plume dispersion of a diesel backup generator plume in New York City (Tong and Zhang, 2015). LES is employed to resolve the unsteady turbulent flow field. In LES, a low-pass filtering operation is performed so that the resulting velocity field can be resolved on a relatively coarse grid. A dynamic subgrid model is chosen, which allows the Smagorinsky constant to vary in space and time (Germano et al., 1991). The constant is dynamically computed based on the information provided by the resolved scales of motion. Logarithmic wall function is applied to the near-wall region as it is computationally impractical to resolve every viscous sublayer in a large domain (Launder and Spalding, 1974). The size of the modeling domain is roughly  $473 \times 372 \times 168\text{m}$  (Figure 5.2). It is meshed with 3.8 million unstructured elements with prism layers near the wall. Grid

independency study is conducted to ensure the results are independent of the mesh resolution.

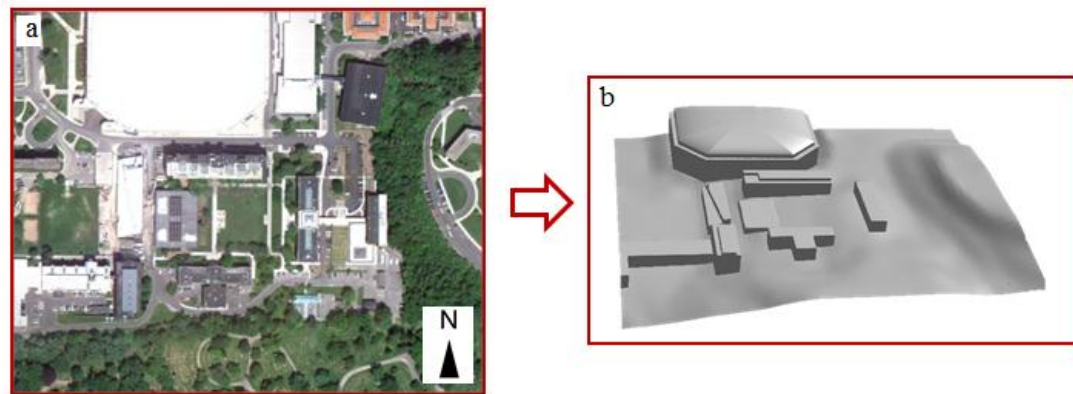


Figure 5.2: a) Satellite image of the Modeling area b) The corresponding geometry generated for simulation

Boundary conditions such as vertical wind and temperature profiles are critical inputs to micro-environmental modeling. The quality of micro-environmental simulation relies on those profiles specified at the boundaries. However, those profiles are usually unavailable for most cities including, Syracuse, NY where the biomass CHP is located. In this study, we employed a semi-empirical methodology to create site-specific inflow profile based on on-site flow measurement. Depending on the wind direction, two sets of boundary condition are developed in combination with on-site measurement. During the period when the wind was from the South to the Carrier Dome station, we constrained the wind data to match the measurement on the roof level of the Gateway station. During the period when the wind was from the West to the Illick station, the wind data collected at the upwind anemometer station was employed to match the wind profile obtained from the meteorology processor as the inflow boundary condition. Atmospheric stability is computed by AERMET, which is

based on meteorology data from the nearby airport. Symmetry boundary condition is applied on the top of the domain as slip walls with zero-shear. At the flow outlet (vary with wind direction), zero diffusion flux of all flow variables is specified. In the model, we treat primary  $PM_{2.5}$  as a tracer species, i.e., assuming that gas/particle partitioning near stacks will not significantly change the primary  $PM_{2.5}$  mass near the sources. The biomass CHP is treated as the only source, and background  $PM_{2.5}$  is determined from measurement.

### **5.3.1 Stack Parameters**

The biomass CHP is installed in the basement of the Gateway building. A list of stack parameters is shown in Table 1 (RSG Inc., 2011). The  $PM_{2.5}$  emission factor is derived based on stack measurement (EPA Method 5/202). The PM control efficiency is calculated based on upstream and downstream measurement of the ESP at full load. It should be noted that the emission factor measured in the stack test appears to be much greater than data measured at other sites according to NESCAUM, which is due to the non-optimized CHP system. In the following chapters, the fuel-based emission factor is employed for model evaluation as it is derived from the same air quality instrument. The AP-42 emission factor is used for the design scenarios presented in chapter 4.2 to 4.5 as it is more widely used in the permitting process.

Table 5.1: Stack Parameters

Parameter	Value	Reference
Exhaust Flow Rate [m <sup>3</sup> /s]	1.8	Permit Application
Exhaust Temperature [K]	350	On-site Measurement
Stack Diameter [m]	0.4	Permit Application
Stack Height <sup>a</sup> [m]	16.7	Permit Application
PM <sub>2.5</sub> Emission Factor [g kWh <sup>-1</sup> ]	0.11	AP-42
PM <sub>2.5</sub> Emission Factor [g kWh <sup>-1</sup> ]	0.18	Emission test
PM <sub>2.5</sub> Emission Factor [g kWh <sup>-1</sup> ]	0.29	Fuel-based
ESP Efficiency (Full load)	85.1%	Stack Test
Fuel Consumption Rate [kg/s]	0.16	Permit Application

<sup>a</sup> Stack height is measured from the ground level of the building

### 5.3.2 Fuel-based Emission Factor

The fuel-based emission factor is derived based on near-source measurement, which is defined as the mass of pollutant emitted per mass of fuel consumed. Carbon balance calculations are based on the fuel combustion process, relating the emission of carbon-containing species from vehicle exhaust to fuel consumption (Stedman, 1989; W. Kirchstetter et al., 1999; Wang et al., 2012a). We consider CO<sub>2</sub> and CO as the carbonaceous products during the combustion process since gas-phase carbonaceous products are usually dominated by CO<sub>2</sub> and CO (Wang et al., 2009; Westerdahl et al., 2009). The emission factor is calculated as following:

$$EF_P = \frac{\Delta[PM_{2.5}]}{\Delta[CO_2] \times \frac{MW_C}{MW_{CO_2}} + \Delta[CO] \times \frac{MW_C}{MW_{CO}}} \times w_c \quad (31)$$

where  $\Delta[PM_{2.5}]$ ,  $\Delta[CO_2]$ , and  $\Delta[CO]$  represent the increase of PM<sub>2.5</sub> and CO<sub>2</sub> over the background respectively.  $w_c$  is the mass fraction of carbon in the fuel. For biomass fuel, i.e., wood pellets,  $w_c$  is chosen as 50% (Oberberger and Thek, 2004).  $EF_P$  is

converted to emission rate [kg/s] by multiplying the fuel consumption rate  $Q$ .

### 5.3.3 Uncertainties

The uncertainty involved in the air quality study can be divided into both experimental and numerical components. In the experimental component, the main uncertainty is attributed to sampling error, which can be split into fixed and random error (Moffat, 1988). The fixed error is associated with the instrument (e.g. accuracy, resolution), and the random error arises from many sources (e.g. background noise, convergence error). The instrument accuracy and resolution are presented in Table 5.2. The random error is computed with a bootstrap algorithm, which is a method to directly estimate the probability density function of any statistic we can imagine that can be calculated from the measurement (Efron and Tibshirani, 1994). For the random error, we computed the 95% confidence intervals of the mean wind speeds and wind directions. As for the  $PM_{2.5}$  concentration, the random error is not quantifiable because we focused on single spike measurements and our instruments were not able to run in triplicate. Therefore, only fixed error is computed for  $PM_{2.5}$  data. Then, we estimated the total measurement error of the wind data using the root sum square technique shown in Eqn 32 below. The calculated error bars for the total measurement error are presented in Figure 5.4 and Figure 5.5.

$$\delta_{total} = \sqrt{\delta_{fixed}^2 + \delta_{random}^2} \quad (32)$$

In contrast with the experimental error, the numerical component is generally much greater than that of experimental component, which arises from model physics and

model inputs (Hanna, 1988). These uncertainties are dominant but difficult to quantify. Therefore, we only discuss the likely causes in this section. As for the model physics, building simplification and turbulence modeling involves certain degree of uncertainties. Emission factors, meteorology-based boundary condition are major sources of the uncertainty for the model inputs. Although there are uncertainties in the air quality model, we were able to present the data with confidence by evaluating the performance with measurement which has fewer uncertainties. However, any specific number is not encouraged to be quoted as the goal of this study is to identify the overall trend for policy-makers.

Table 5.2: Fixed and random error for different sampling instruments. The range of random error for the sonic anemometers is listed.

<b>Sampling Instrument</b>	<b>Fixed Error</b>	<b>Random Error</b>
<b>Sonic Anemometer (Gill, 1561-PK-020)</b>	Direction: $\pm 2$ degree Speed: $\pm 1.5\%$	Direction: $\pm 1.6$ to $\pm 8.6$ degree Speed: $\pm 0.02$ to $\pm 0.09$ m/s
<b>PM<sub>2.5</sub> Personal DataRam (Thermo Scientific, pDR-1200)</b>	1%	N/A
<b>CO<sub>2</sub> sensor (MI70, VAISALA)</b>	1.5%	N/A
<b>CO sensor (TSI Model 7545)</b>	3%	N/A

## 5.4. Results

### 5.4.1 Model Evaluation

The data on March 19, 2015 was selected for simulation purpose as there was a noticeable shift in wind direction from the South to the West while the load of biomass boiler was steady. This allowed us to detect biomass at both stations and employ the fueled-based emission factor computed on the Illick Hall to predict the concentration

at the rooftop of Carrier Dome station. Three concurrent biomass plume spike were identified on the rooftop of Illick Hall by synchronizing the CO<sub>2</sub> and PM<sub>2.5</sub> concentrations (Figure 5.3, a, b, c). Another three spikes were observed on the rooftop of Carrier Dome (Figure 5.3, d e f).

Figure 5.4 presents a comparison between simulated and measured wind speed and direction. In general, a good agreement between predicted and on-site measurement is observed for flow fields. This demonstrated that our model is capable of capturing the flow field under the influence of complex nearby buildings, which is essential for plume dispersion modeling. The comparison between simulated and measured PM<sub>2.5</sub> concentration in the plume is displayed in Figure 5.5. A satisfactory agreement is shown. The predictions at the Illick Hall station agrees better than that at the Carrier Dome as expected, because the emission rate is derived based the measurement on the Illick station. Slight discrepancies observed are likely due to simplified geometry and uncertainties in the fuel-based emission rate.

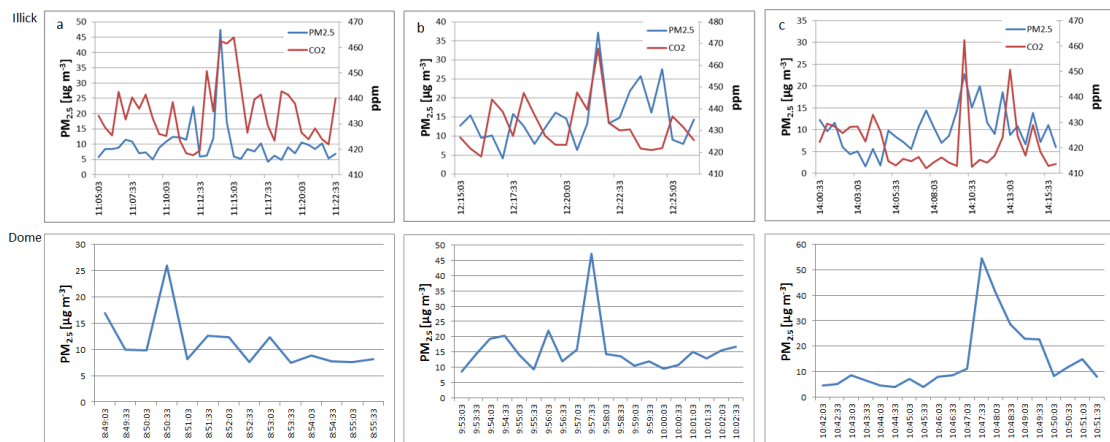


Figure 5.3: a, b, c ) Synchronized spikes observed on the Illick station; d, e, f) spikes observed on the Carrier Dome station.

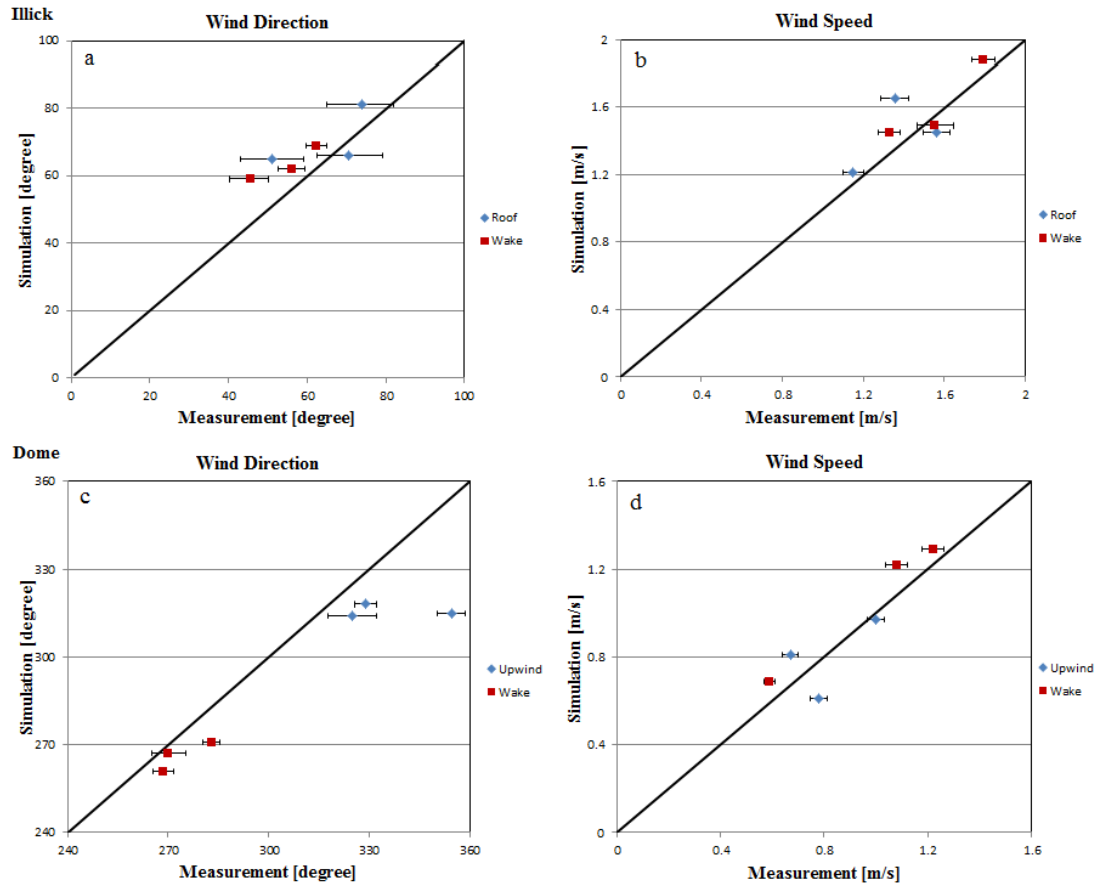


Figure 5.4: Comparison between simulated and measured wind speed and direction. a and b are under the boundary condition where wind is from the West to Illick Hall. c and d are under the boundary condition where the wind is from the South to the Dome. Error bars of the total measurement error are added on each data point.

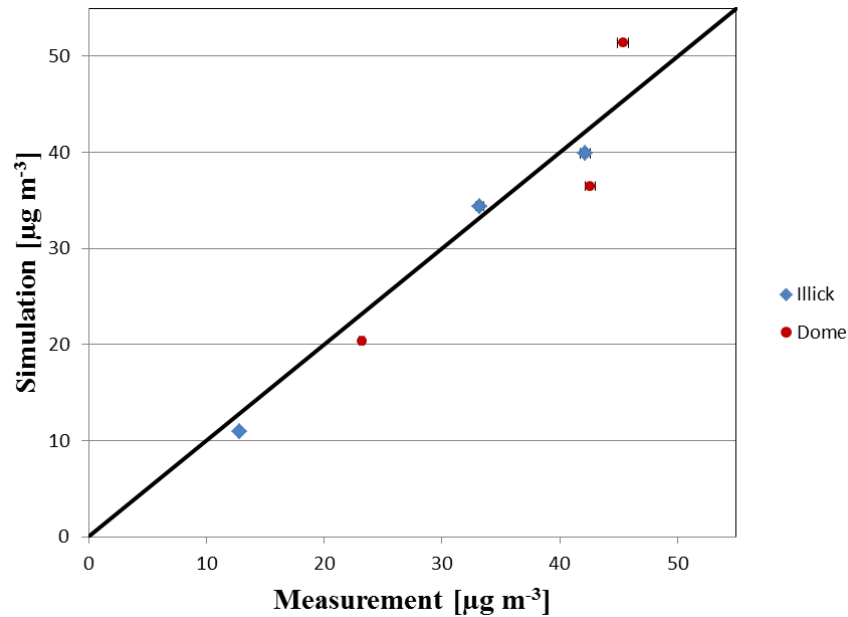


Figure 5.5: Comparison between simulated and measured  $\text{PM}_{2.5}$  concentration. Error bars (fixed error only) are applied on the measurement data. However, they may not seem visible as the error range is small.

#### 5.4.2. With and Without Emission Control

The emission factor in the absence of the ESP is derived based on the control efficiency measured in the stack test (Table 1). A comparison of the  $\text{PM}_{2.5}$  concentration in the surrounding environment with and without ESP is displayed in Figure 6. Our analysis shows a significant increase in near-ground  $\text{PM}_{2.5}$ . The maximum concentration is discovered in the wake zone behind Illick Hall exceeding  $30 \mu\text{g m}^{-3}$ . This is almost 7 times the concentration with ESP control. The concentration all around the building adjacent to Illick hall reached over  $100 \mu\text{g m}^{-3}$ . This could lead to increased exposure to air pollution for students in the building as particles are able to transport indoor through windows or HVAC system as well as students who live in dormitory buildings on the hill downwind to the stack.

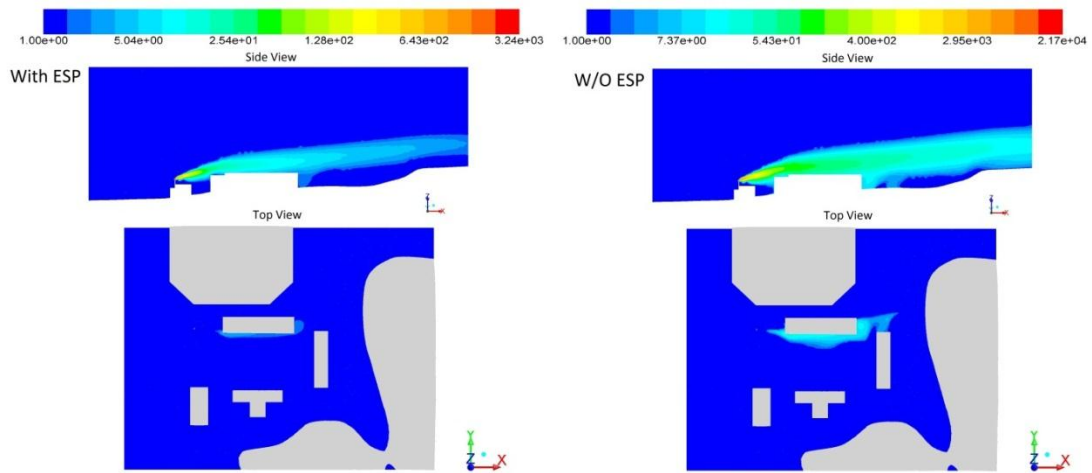


Figure 5.6: A comparison of the PM<sub>2.5</sub> concentration [ $\mu\text{g m}^{-3}$ ] contour plot (side and top views) in the surrounding environment with and without ESP

### 5.4.3 Ambient Wind Speed

In this section, the influence of several physical parameters including stack temperature, ambient wind, and surrounding structures is explored. The impact of the ambient wind speed is first tested. It is evident from the simulation that increasing wind speed reduces the downwind vertical mixing and effective stack height of the plume, and therefore elevates the ground-level concentration both in the adjacent street canyon and wake of Illick Hall (Figure 5.7).

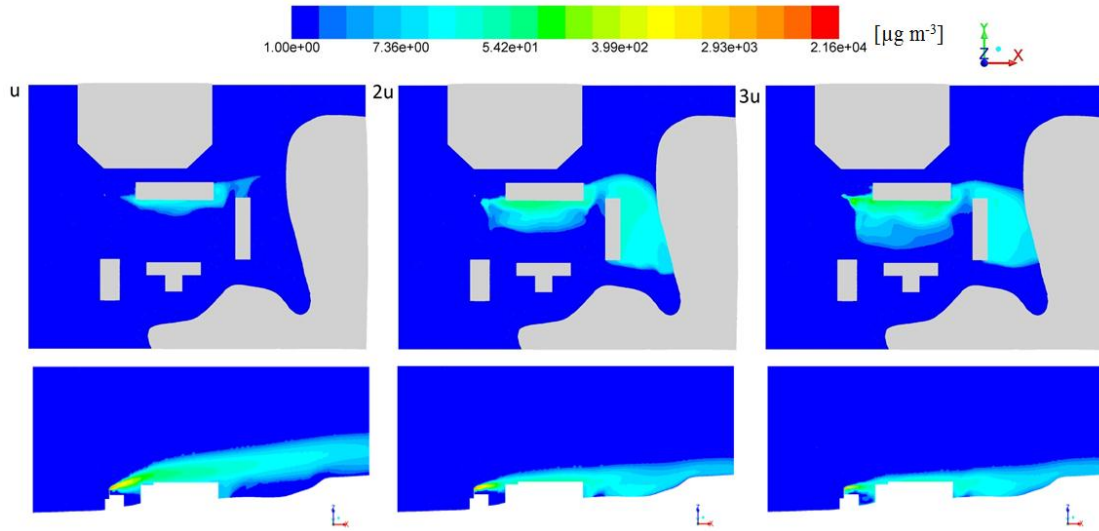


Figure 5.7: Contour plot of the  $PM_{2.5}$  concentration in side view at three ambient wind speeds.  $u$  is the baseline wind speed at 2 m/s.

#### 5.4.4 Stack Temperature

The effect of stack temperature is also investigated. The plume rise due to buoyance is dependent on the stack temperature. For many boilers, stack economizers are often installed to recover waste heat from the hot exhaust gas and therefore improves boiler efficiency (DOE, 2010). It is shown in the industry that the boiler efficiency can be increased by 1% by every 40 degree °F reduction of exhaust temperature (DOE, 2012). Therefore, we varied the stack temperature by  $\pm 100$  degree from the baseline to investigate its impact on near-source environment. The resulting contour plot of  $PM_{2.5}$  concentration is displayed in Figure 5.8. Raising the stack temperature creates more air buoyance and causes the plume to travel higher from the ground (Figure 5.8). As a result, the near-ground concentration decreases with increasing stack temperature. In addition, it is worth noting that  $PM_{2.5}$  concentration at the roof top level remain more or less the same regardless the stack temperature. This implies the dominant role of nearby building on stack plume dispersion.

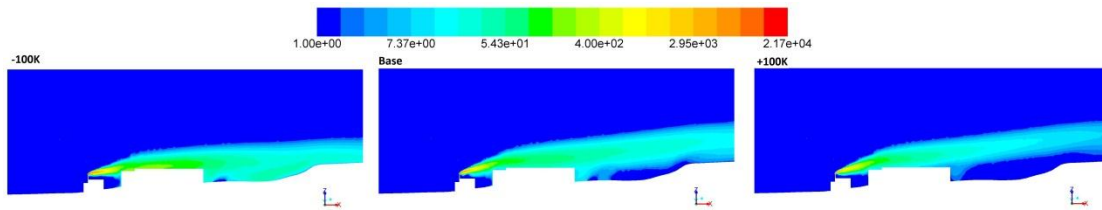


Figure 5.8: Contour plot of the PM<sub>2.5</sub> concentration [ $\mu\text{g m}^{-3}$ ] at three stack temperatures.

The biomass facility is adjacent to a large stadium, which could impact the plume dispersion under certain wind directions. We simulated the case where the dome is upwind to the stack and compared against the case without the dome. The contour plot of PM<sub>2.5</sub> concentration with and without dome is shown in both side and top views (Figure 5.9). A considerably different plume trajectory is observed. The presence of the dome creates a building downwash effect, which draws the plume sideways and increases the concentration near the stack. In contrast, less plume rise is observed as horizontal wind is stronger in the absence of the upwind building. The plume is able to travel closely along the prevailing wind direction and the near-stack area is sufficiently diluted.

#### 5.4.5 Removing Carrier Dome

The biomass facility is adjacent to a large stadium, which could impact the plume dispersion under certain wind directions. We simulated the case where the Carrier Dome is upwind to the stack and compared against the case without the Carrier Dome. The contour plot of PM<sub>2.5</sub> concentration with and without Carrier Dome is shown in both side and top views (Figure 5.9). A considerably different plume trajectory is observed. The presence of the Carrier Dome creates a building downwash effect, which draws the plume sideways and increases the concentration near the stack.

In contrast, less plume rise is observed as horizontal wind is stronger in the absence of the upwind building. The plume is able to travel closely along the prevailing wind direction and the near-stack area is sufficiently diluted.

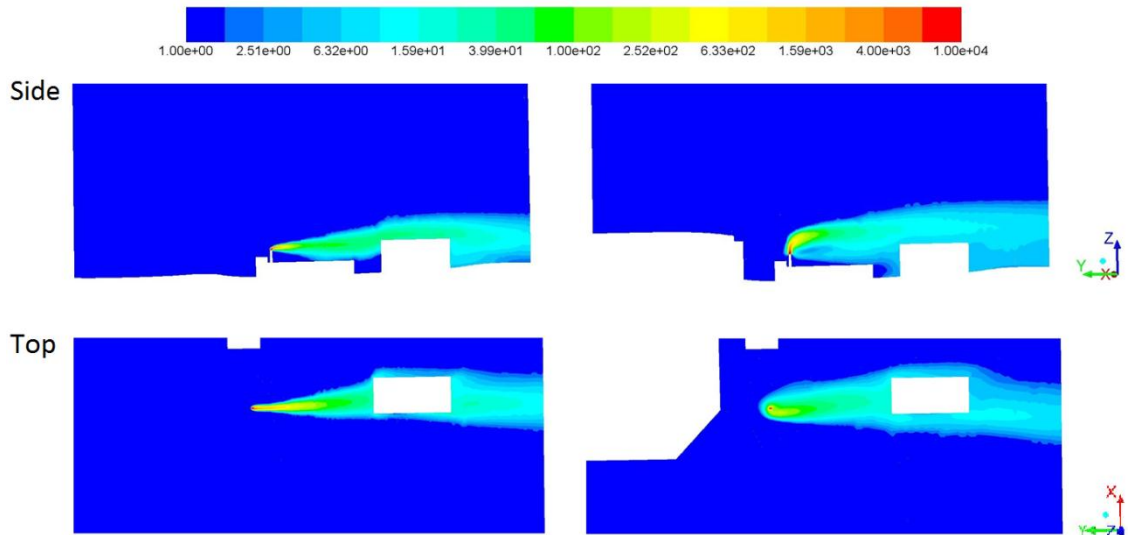


Figure 5.9: Contour plot of the PM<sub>2.5</sub> concentration [ $\mu\text{g m}^{-3}$ ] with and without Carrier Dome in side and top views

## 5.5. Conclusion

In this study, we investigated the spatial variation of PM<sub>2.5</sub> in a micro-environment near a stack of biomass CHP facility. ESP upstream and downstream emission factors are derived based on in-stack measurement (EPA Method 5/202). A CFD-based micro-environmental model was developed to capture surrounding buildings and the hilly terrain with complex meshing technique. A good agreement between predicted and on-site measurement is observed for both flow fields and plume dispersion. Our numerical analysis shows an almost 7 times increase of PM<sub>2.5</sub> concentration in the surrounding environment without ESP emission control. The maximum near-ground concentration exceeds  $30 \mu\text{g m}^{-3}$ , and the concentration on rooftop reached over  $100 \mu\text{g m}^{-3}$ . This could be a serious health threat to people living

inside the building as particles are able to transport indoor through windows or HVAC system. This demonstrates the importance of emission control for biomass combustion system.

Sensitivity studies on various design scenarios are conducted. Our study first shows presence of either tall upwind or downwind building can deteriorate the air quality in the near-stack street canyons, largely due to the building downwash effect. Second, we found that strategies that are often used to improve boiler efficiency, i.e., stack economizer, could elevate the near-ground  $PM_{2.5}$  concentration by reducing the plume rise. This is a tradeoff between near-source environment and boiler efficiency. Therefore, simply targeting on high energy efficiencies may deteriorate the air quality of surrounding environment as an unintended consequence.

# Chapter 6

## Major Contribution

Rapid urbanization has resulted in increasing urban air pollution in major cities, especially in developing countries. Studies have shown that people who live, work, or go to school near roadways are at risk for a various health problems, including respiratory and cardiovascular problems, birth and developmental defects, and cancer, due to exposure to harmful traffic-related air pollutants. This dissertation presents the effort in understanding and mitigating the near-source air pollution in urban microenvironments.

Four unique projects have been conducted to investigate various near-source air quality problems in several major cities such as New York City, Syracuse, NY, Rochester, NY and Chapel Hill, NC. The CFD-based air quality model was developed to capture the impact of complex building structure and topography with advanced meshing strategy as well as site-specific micrometeorology condition that plays a critical role on plume dispersion. The model has been evaluated with several datasets from both near-source field studies and wind tunnel experiments, and agrees adequately with the measurement. Some of the major findings have already been published in top ranked journals in the area of air quality research. The findings presented in the dissertation will assist urban planning and landscape design with quantitative design options to mitigate the risk of human exposure to hazardous air pollutants. Due to the high complexity in the urban environment, this dissertation also

encourages urban planners to conduct site-specific studies in order to accurately determine the air quality impact of many emission sources.

In my first project, a CFD-based air quality model was developed to simulate the transport of Black Carbon (BC) from Highway I-87 next to an urban school in South Bronx, NYC. The model was evaluated against and agrees adequately with the measurements of wind speed, wind directions and BC concentrations. Our analysis suggests that the BC concentration at the measurement point of the urban school could decrease by 43-54% if roadside buildings were absent. Furthermore, we characterize two generalized conditions in a highway-building environment, i.e., highway-building canyon and highway viaduct-building. The former refers to the canyon between solid highway embankment and roadside buildings, where the spatial profiles of BC depend on the equivalent canyon aspect ratio and flow recirculation. The latter refers to the area between a highway viaduct (i.e., elevated highway with open space underneath) and roadside buildings, where strong flow recirculation is absent and the spatial profiles of BC are determined by the relative heights of the highway and buildings. This study demonstrates the importance of incorporating highway-building interaction into the assessment of human exposure to near-road air pollution. It also calls for active roles of building and highway designs in mitigating near-road exposure of urban population.

In the second project, I explored a variety of roadside barriers design to mitigate near-road air pollution. Roadside vegetation barriers have shown the potential to reduce near-road air pollution concentrations; however, the characteristics of these barriers needed to ensure pollution reductions are not well understood. I first modified

Large Eddy Simulation (LES) to capture the effects of vegetation barriers on near-road air quality. Its performance was evaluated against a field dataset collected at Chapel Hill, NC. Next, the model was employed to explore the effects of eight conceptual roadside vegetation/solid barrier configurations on near-road size-resolved particle concentrations, governed by dispersion and deposition. My analysis indicated that the effects of vegetation barriers can be categorized into three general regimes: on-road, immediate barrier vicinity and near-road. My analysis further revealed two potentially viable design options: a) a wide vegetation barrier with high leaf area density which reduces downwind particle concentrations significantly, while resulting in a moderate increase in on-road concentrations, and b) vegetation-solid barrier combinations, i.e., planting trees next to a solid barrier, leads to the greatest reduction in downwind particle concentrations among all configurations and a large increase in on-road concentrations at the same time. The findings presented in the study will assist urban planning and forestry organizations with evaluating different green infrastructure design options.

In the third project, the focus was on diesel backup generators that participate in demand response (DR) programs in metropolitan areas. We improved the micro-environmental air quality simulations by employing a meteorology processor, AERMET, to generate site-specific boundary layer parameters for the Large Eddy Simulation (LES). The modeling structure was employed to evaluate the environmental impacts of diesel backup generators in near-source microenvironments. I found that the presence of either tall upwind or downwind building can deteriorate the air quality in the near-stack street canyons, largely due to the recirculation zones

generated by the tall buildings, reducing the near-stack dispersion. Decreasing exhaust momentum ratio (stack exit velocity/ambient wind velocity) draws more exhaust into the recirculation zone, and reduces the effective stack height, which results in elevated near-ground concentrations inside downwind street canyons. The near-ground  $\text{PM}_{2.5}$  concentration for the worst scenarios could well exceed  $100 \mu\text{g m}^{-3}$ , posing potential health risk to people living and working nearby. My study implies that the siting of diesel backup generators stacks should consider not only the interactions of fresh air intake and exhaust outlet for the building housing the backup generators, but also the dispersion of exhaust plumes in the surrounding environment.

In the last project, I investigated the micro-environmental air quality impact of a biomass-fueled combined heat and power system equipped with an electrostatic precipitator (ESP) in Syracuse, NY. This study combines both field experiment and numerical simulation. Two rooftop stations with  $\text{PM}_{2.5}$  and  $\text{CO}_2$  analyzers were set up in the way that one can capture the plume while the other one serves as the background in comparison depending on the wind direction. Four sonic anemometers were deployed around the stack to quantify highly spatially and temporally resolved local wind pattern. A computational fluid dynamic-based micro-environmental model was applied to simulate the experimental conditions, and a good agreement between predicted and on-site measurement is observed for both flow fields and plume dispersion. My analysis shows that the absence of ESP could lead to an almost 7 times increase in near-ground  $\text{PM}_{2.5}$  concentrations with a maximum concentration  $>50 \mu\text{g m}^{-3}$  in the surrounding environment. This result demonstrates the critical role of air pollution controls for biomass combustion systems. In addition, we explored various

physical parameters including stack temperature/height, ambient wind, and surrounding structures to provide recommendations for siting biomass-fueled heating equipment in order to minimize local air pollution.

## BIBLIOGRAPHY

- Abdul-Khalek, I., Kittelson, D., Brear, F., 1999. The influence of dilution conditions on diesel exhaust particle size distribution measurements. SAE Technical paper.
- Al-Dabbous, A.N., Kumar, P., 2014. The influence of roadside vegetation barriers on airborne nanoparticles and pedestrians exposure under varying wind conditions. *Atmospheric Environment* 90, 113-124.
- Arya, P.S., 2001. Introduction to micrometeorology. Academic press.
- ASHRAE, 2003. Application Handbook. Chapter 44.
- Baldauf, R., Jackson, L., Hagler, G., Vlad, I., McPherson, G., Nowak, D., Cahill, T., Zhang, M., Cook, R., Bailey, C., 2011. The role of vegetation in mitigating air quality impacts from traffic emissions.
- Baldauf, R., Thoma, E., Khlystov, A., Isakov, V., Bowker, G., Long, T., Snow, R., 2008. Impacts of noise barriers on near-road air quality. *Atmospheric Environment* 42, 7502-7507.
- Blocken, B., Stathopoulos, T., Saathoff, P., Wang, X., 2008. Numerical evaluation of pollutant dispersion in the built environment: comparisons between models and experiments. *Journal of Wind Engineering and Industrial Aerodynamics* 96, 1817-1831.
- Boarnet, M.G., Houston, D., Edwards, R., Princevac, M., Ferguson, G., Pan, H., Bartolome, C., 2011. Fine particulate concentrations on sidewalks in five Southern California cities. *Atmospheric Environment* 45, 4025-4033.
- Boman, B.C., Forsberg, A.B., Järholm, B.G., 2003. Adverse health effects from ambient air pollution in relation to residential wood combustion in modern society. *Scandinavian Journal of Work, Environment & Health* 29, 251-260.
- Bowker, G.E., Baldauf, R., Isakov, V., Khlystov, A., Petersen, W., 2007. The effects of roadside structures on the transport and dispersion of ultrafine particles from highways. *Atmospheric Environment* 41, 8128-8139.
- Boylan, J.W., Russell, A.G., 2006. PM and light extinction model performance metrics, goals, and criteria for three-dimensional air quality models. *Atmospheric Environment* 40, 4946-4959.
- Brantley, H.L., Hagler, G.S.W., J. Deshmukh, P., Baldauf, R.W., 2014. Field assessment of the effects of roadside vegetation on near-road black carbon and particulate matter. *Science of The Total Environment* 468-469, 120-129.
- Businger, J.A., Wyngaard, J.C., Izumi, Y., Bradley, E.F., 1971. Flux-Profile

Relationships in the Atmospheric Surface Layer. *Journal of the Atmospheric Sciences* 28, 181-189.

Carreras-Sospedra, M., Vutukuru, S., Brouwer, J., Dabdub, D., 2010. Central power generation versus distributed generation – An air quality assessment in the South Coast Air Basin of California. *Atmospheric Environment* 44, 3215-3223.

Carter, J.J., Petersen, R.L., Cochran, B., 2005. Designing Exhaust Systems to minimize energy costs. *ASHRAE journal* 47.

Cassiani, M., Katul, G.G., Albertson, J.D., 2008. The Effects of Canopy Leaf Area Index on Airflow Across Forest Edges: Large-eddy Simulation and Analytical Results. *Boundary-Layer Meteorol* 126, 433-460.

Caterpillar, Technical Data Diesel Generator Set CAT 3512B-1500.

Chan, T.L., Dong, G., Leung, C.W., Cheung, C.S., Hung, W.T., 2002. Validation of a two-dimensional pollutant dispersion model in an isolated street canyon. *Atmospheric Environment* 36, 861-872.

Chow, J.C., Watson, J.G., Doraiswamy, P., Chen, L.-W.A., Sodeman, D.A., Lowenthal, D.H., Park, K., Arnott, W.P., Motallebi, N., 2009. Aerosol light absorption, black carbon, and elemental carbon at the Fresno Supersite, California. *Atmospheric Research* 93, 874-887.

Cimorelli, A.J., Perry, S.G., Venkatram, A., Weil, J.C., Paine, R.J., Wilson, R.B., Lee, R.F., Peters, W.D., Brode, R.W., 2005. AERMOD: A dispersion model for industrial source applications. Part I: General model formulation and boundary layer characterization. *Journal of Applied Meteorology* 44, 682-693.

Dockery, D.W., Pope, C.A., Xu, X., Spengler, J.D., Ware, J.H., Fay, M.E., Ferris, B.G., Speizer, F.E., 1993. An Association between Air Pollution and Mortality in Six U.S. Cities. *New England Journal of Medicine* 329, 1753-1759.

DOE, 2010. Steam Generation Efficiency Module, Efficiency Definition Section.

DOE, 2012. Use Feedwater Economizers for Waster Heat Recovery.

Dupont, S., Brunet, Y., 2008. Influence of foliar density profile on canopy flow: a large-eddy simulation study. *Agricultural and Forest Meteorology* 148, 976-990.

Efron, B., Tibshirani, R.J., 1994. An introduction to the bootstrap. CRC press.

Finlayson, E.U., Gadgil, A.J., Thatcher, T.L., Sextro, R.G., 2004. Pollutant dispersion in a large indoor space. Part 2: Computational fluid dynamics predictions and comparison with a scale model experiment for isothermal flow. *Indoor Air* 14, 272-283.

- Finn, D., Clawson, K.L., Carter, R.G., Rich, J.D., Eckman, R.M., Perry, S.G., Isakov, V., Heist, D.K., 2010. Tracer studies to characterize the effects of roadside noise barriers on near-road pollutant dispersion under varying atmospheric stability conditions. *Atmospheric Environment* 44, 204-214.
- Fuller, M., Bai, S., Eisinger, D., Niemeier, D., 2009. Practical mitigation measures for diesel particulate matter: near-road vegetation barriers. Contract AQ-04-01: developing effective and quantifiable air quality mitigation measures. University of California, Davis.
- Garg, R., Karpati, A., Leighton, J., Perrin, M., Shah, M., 2003. *Asthma Facts*, Second Edition.
- Gerashchenko, S., Good, G., Warhaft, Z., 2011. Entrainment and mixing of water droplets across a shearless turbulent interface with and without gravitational effects. *J Fluid Mech* 668, 293-303.
- Germano, M., Piomelli, U., Moin, P., Cabot, W.H., 1991. A dynamic subgrid-scale eddy viscosity model. *Physics of Fluids A: Fluid Dynamics (1989-1993)* 3, 1760-1765.
- Gilmore, E.A., Adams, P.J., Lave, L.B., 2010. Using Backup Generators for Meeting Peak Electricity Demand: A Sensitivity Analysis on Emission Controls, Location, and Health Endpoints. *Journal of the Air & Waste Management Association* 60, 523-531.
- Gilmore, E.A., Lave, L.B., Adams, P.J., 2006. The costs, air quality, and human health effects of meeting peak electricity demand with installed backup generators. *Environmental Science & Technology* 40, 6887-6893.
- Gong, J., Zhu, T., Kipen, H., Wang, G., Hu, M., Ohman-Strickland, P., Lu, S., Zhang, L., Wang, Y., Zhu, P., Rich, D., Diehl, S., Huang, W., Zhang, J., 2013. Malondialdehyde in exhaled breath condensate and urine as a biomarker of air pollution induced oxidative stress. *J Expo Sci Environ Epidemiol* 23, 322 - 327.
- Gousseau, P., Blocken, B., Stathopoulos, T., van Heijst, G.J.F., 2011. CFD simulation of near-field pollutant dispersion on a high-resolution grid: A case study by LES and RANS for a building group in downtown Montreal. *Atmospheric Environment* 45, 428-438.
- Greene, N., Hammerschlag, R., 2000. Small and Clean Is Beautiful: Exploring the Emissions of Distributed Generation and Pollution Prevention Policies. *The Electricity Journal* 13, 50-60.
- Hagler, G.S., Lin, M.-Y., Khlystov, A., Baldauf, R.W., Isakov, V., Faircloth, J., Jackson, L.E., 2012. Field investigation of roadside vegetative and structural barrier impact on near-road ultrafine particle concentrations under a variety of wind conditions. *Science of The Total Environment* 419, 7-15.

Hagler, G.S.W., Tang, W., Freeman, M.J., Heist, D.K., Perry, S.G., Vette, A.F., 2011. Model evaluation of roadside barrier impact on near-road air pollution. *Atmospheric Environment* 45, 2522-2530.

Hanna, S.R., 1988. Air Quality Model Evaluation and Uncertainty. *JAPCA* 38, 406-412.

Hanna, S.R., Chang, J.C., 1993. Hybrid plume dispersion model (HPDM) improvements and testing at three field sites. *Atmospheric Environment. Part A. General Topics* 27, 1491-1508.

Heath, G.A., Granvold, P.W., Hoats, A.S., W Nazaroff, W., 2006. Intake fraction assessment of the air pollutant exposure implications of a shift toward distributed electricity generation. *Atmospheric Environment* 40, 7164-7177.

HEI, 2010. *Traffic-Related Air Pollution: A Critical Review of the Literature on Emissions, Exposure, and Health Effects.*

Heist, D.K., Perry, S.G., Brixey, L.A., 2009. A wind tunnel study of the effect of roadway configurations on the dispersion of traffic-related pollution. *Atmospheric Environment* 43, 5101-5111.

Horvath, H., 1993. Atmospheric light absorption--A review. *Atmospheric Environment. Part A. General Topics* 27, 293-317.

Hoydysh, W.G., Dabberdt, W.F., 1988. Kinematics and dispersion characteristics of flows in asymmetric street canyons. *Atmospheric Environment (1967)* 22, 2677-2689.

Huang, C.H., 1979. A theory of dispersion in turbulent shear flow. *Atmospheric Environment (1967)* 13, 453-463.

Jansen, K.L., Larson, T.V., Koenig, J.Q., Mar, T.F., Fields, C., Stewart, J., Lippmann, M., 2005. Associations between Health Effects and Particulate Matter and Black Carbon in Subjects with Respiratory Disease. *Environ Health Perspect* 113, 1741-1746.

Jeong, C.-H., Hopke, P.K., Kim, E., Lee, D.-W., 2004. The comparison between thermal-optical transmittance elemental carbon and Aethalometer black carbon measured at multiple monitoring sites. *Atmospheric Environment* 38, 5193-5204.

Jing, Q., Venkatram, A., 2011. The relative impacts of distributed and centralized generation of electricity on local air quality in the South Coast Air Basin of California. *Energy Policy* 39, 4999-5007.

Kim Oanh, N.T., Thiansathit, W., Bond, T.C., Subramanian, R., Winijkul, E., Pawarmart, I., 2010. Compositional characterization of PM<sub>2.5</sub> emitted from in-use diesel vehicles. *Atmospheric Environment* 44, 15-22.

Launder, B.E., Spalding, D.B., 1974. The numerical computation of turbulent flows. *Computer Methods in Applied Mechanics and Engineering*, 3(2):269-289.

Lena, T.S., Ochieng, V., Carter, M., Holguin-Veral, J., P.L., a.K., 2002. Elemental carbon and PM<sub>2.5</sub> levels in an urban community heavily impacted by truck traffic. *Environ Health Perspect*, 10009–10015.

Lioussse, C., Cachier, H., Jennings, S.G., 1993. Optical and thermal measurements of black carbon aerosol content in different environments: Variation of the specific attenuation cross-section, sigma ( $[\sigma]$ ). *Atmospheric Environment. Part A. General Topics* 27, 1203-1211.

Litschke, T., Kuttler, W., 2008. On the reduction of urban particle concentration by vegetation—a review. *Meteorologische Zeitschrift* 17, 229-240.

Lomas, K.J., 2007. Architectural design of an advanced naturally ventilated building form. *Energy and Buildings* 39, 166-181.

Lovett, G.M., 1994. Atmospheric Deposition of Nutrients and Pollutants in North America: An Ecological Perspective. *Ecological Applications* 4, 630-650.

Martinuzzi, R., Tropea, C., 1993. The Flow Around Surface-Mounted, Prismatic Obstacles Placed in a Fully Developed Channel Flow (Data Bank Contribution). *Journal of Fluids Engineering* 115, 85-92.

Mathey, F., Cokljat, D., Bertoglio, J.P., Sergent, E., 2006. Assessment of the vortex method for large eddy simulation inlet conditions. *Progress in Computational Fluid Dynamics, An International Journal* 6, 58-67.

McDonald, A.G., Bealey, W.J., Fowler, D., Dragosits, U., Skiba, U., Smith, R.I., Donovan, R.G., Brett, H.E., Hewitt, C.N., Nemitz, E., 2007. Quantifying the effect of urban tree planting on concentrations and depositions of PM<sub>10</sub> in two UK conurbations. *Atmospheric Environment* 41, 8455-8467.

Moffat, R.J., 1988. Describing the uncertainties in experimental results. *Experimental Thermal and Fluid Science* 1, 3-17.

Monin, A.S., Obukhov, A.M., 1954. Basic Laws of Turbulent Mixing in the Ground Layer of the Atmosphere. *Trans. Geophys. Inst. Akad. Nauk* 24, 163-187.

Mordukhovich, I., Wilker, E., Suh, H., Wright, R., Sparrow, D., Vokonas, P.S., Schwartz, J., 2009. Black Carbon Exposure, Oxidative Stress Genes, and Blood Pressure in a Repeated-Measures Study. *Environ Health Perspect* 117.

Ndiema, C.K.W., Mpendazoe, F.M., Williams, A., 1998. Emission of pollutants from a biomass stove. *Energy Conversion and Management* 39, 1357-1367.

- NESCAUM, 2003. Stationary Diesel Engines in the Northeast: An Initial assessment of the Regional Population, Control Technology Options and Air Quality Policy Issues. Northeast States for Coordinated Air Use Management.
- NESCAUM, 2012. Air Quality, Electricity, and Back-up Stationary Diesel Engines in the Northeast. Northeast States for Coordinated Air Use Management.
- NYISO, 2013. Annual Report to the Federal Energy Regulatory Commission on the NYISO Demand Side Management Programs.
- NYS DOT, 2008. PM Emission Factor Table C for all the counties in NYSDOT Region 10 and 11 and Rockland and Westchester counties in NYSDOT Region 8.
- NYSERDA, 2008. Assessment of Carbonaceous PM<sub>2.5</sub> for New York and the Region. Final Report 08-01, Volume 2.
- Obernberger, I., Thek, G., 2004. Physical characterisation and chemical composition of densified biomass fuels with regard to their combustion behaviour. *Biomass and Bioenergy* 27, 653-669.
- Oke, T.R., 1988. Street design and urban canopy layer climate. *Energy and Buildings* 11, 103-113.
- Patel, M.M., Chillrud, S.N., Correa, J.C., Feinberg, M., Hazi, Y., Deepti, K.C., Prakash, S., Ross, J.M., Levy, D., Kinney, P.L., 2009. Spatial and temporal variations in traffic-related particulate matter at New York City high schools. *Atmospheric Environment* 43, 4975-4981.
- Patel, M.M., Chillrud, S.N., Correa, J.C., Hazi, Y., Feinberg, M., Kc, D., Prakash, S., Ross, J.M., Levy, D., Kinney, P.L., 2010. Traffic-Related Particulate Matter and Acute Respiratory Symptoms among New York City Area Adolescents. *Environ Health Perspect* 118.
- Pepermans, G., Driesen, J., Haeseldonckx, D., Belmans, R., D'haeseleer, W., 2005. Distributed generation: definition, benefits and issues. *Energy Policy* 33, 787-798.
- Perry, S.G., 1992. CTDMPLUS: A dispersion model for sources near complex topography. Part I: Technical formulations. *Journal of Applied Meteorology* 31, 633-645.
- Petersen, R.L., Cochran, B.C., LeCompte, J.W., 2002. Specifying exhaust systems that avoid fume reentry and adverse health effects. *Transactions-American Society of Heating Refrigerating and Air Conditioning Engineers* 108, 1039-1052.
- Petroff, A., Zhang, L., 2010. Development and validation of a size-resolved particle dry deposition scheme for application in aerosol transport models. *Geoscientific Model Development* 3, 753-769.

Petroff, A., Zhang, L., Pryor, S.C., Belot, Y., 2009. An extended dry deposition model for aerosols onto broadleaf canopies. *Journal of Aerosol Science* 40, 218-240.

Pope, S.B., 2000. *Turbulent flows*. Cambridge University Press.

Porter, C.J., 2006. Determining Stack Height to Prevent Contaminant Re-Entry through Building Intakes. *Chicago Electronic Proceedings*.

Rattigan, O.V., Dirk Felton, H., Bae, M.-S., Schwab, J.J., Demerjian, K.L., 2010. Multi-year hourly PM<sub>2.5</sub> carbon measurements in New York: Diurnal, day of week and seasonal patterns. *Atmospheric Environment* 44, 2043-2053.

Richards, P.J., Hoxey, R.P., 1993. Appropriate boundary conditions for computational wind engineering models using the  $k-\epsilon$  turbulence model. *Journal of Wind Engineering and Industrial Aerodynamics* 46-47, 145-153.

Robins, A.G., Castro, I.P., 1977. A wind tunnel investigation of plume dispersion in the vicinity of a surface mounted cube—II. The concentration field. *Atmospheric Environment (1967)* 11, 299-311.

RSG Inc., 2011. Combined Heat and Power Plant Permit Application for SUNY College of Environmental Science and Forestry

Shah, S.D., Cocker III, D.R., Johnson, K.C., Lee, J.M., Soriano, B.L., Wayne Miller, J., 2006. Emissions of regulated pollutants from in-use diesel back-up generators. *Atmospheric Environment* 40, 4199-4209.

Shaw, R.H., Schumann, U., 1992. Large-eddy simulation of turbulent flow above and within a forest. *Boundary-Layer Meteorol* 61, 47-64.

Shaw, R.H., Zhang, X.J., 1992. Evidence of pressure-forced turbulent flow in a forest. *Boundary-Layer Meteorol* 58, 273-288.

Sini, J.-F., Anquetin, S., Mestayer, P.G., 1996. Pollutant dispersion and thermal effects in urban street canyons. *Atmospheric Environment* 30, 2659-2677.

Spira-Cohen, A., Chen, L.C., Kendall, M., Lall, R., Thurston, G.D., 2011. Personal Exposures to Traffic-Related Air Pollution and Acute Respiratory Health among Bronx Schoolchildren with Asthma. *Environ Health Perspect* 119.

Spira-Cohen, A., Chen, L.C., Kendall, M., Sheesley, R., Thurston, G.D., 2010. Personal exposures to traffic-related particle pollution among children with asthma in the South Bronx, NY. *Journal of Exposure Science and Environmental Epidemiology* 20, 446-456.

Stedman, D.H., 1989. Automobile carbon monoxide emission. *Environmental Science & Technology* 23, 147-149.

- Steffens, J.T., Heist, D.K., Perry, S.G., Isakov, V., Baldauf, R.W., Zhang, K.M., 2014. Effects of roadway configurations on near-road air quality and the implications on roadway designs. *Atmospheric Environment* 94, 74-85.
- Steffens, J.T., Heist, D.K., Perry, S.G., Zhang, K.M., 2013. Modeling the effects of a solid barrier on pollutant dispersion under various atmospheric stability conditions. *Atmospheric Environment* 69, 76-85.
- Steffens, J.T., Wang, Y.J., Zhang, K.M., 2012. Exploration of effects of a vegetation barrier on particle size distributions in a near-road environment. *Atmospheric Environment* 50, 120-128.
- Stein, A.F., Isakov, V., Godowitch, J., Draxler, R.R., 2007. A hybrid modeling approach to resolve pollutant concentrations in an urban area. *Atmospheric Environment* 41, 9410-9426.
- Strachan, N., Farrell, A., 2006. Emissions from distributed vs. centralized generation: The importance of system performance. *Energy Policy* 34, 2677-2689.
- Stull, R.B., 1988. *An introduction to boundary layer meteorology*. Springer Science & Business Media.
- Su, H.-B., Shaw, R., Paw, K., Moeng, C.-H., Sullivan, P., 1998. Turbulent Statistics of Neutrally Stratified Flow Within and Above a Sparse Forest from Large-Eddy Simulation and Field Observations. *Boundary-Layer Meteorol* 88, 363-397.
- Tamura, T., 2008. Towards practical use of LES in wind engineering. *Journal of Wind Engineering and Industrial Aerodynamics* 96, 1451-1471.
- Thom, A., 1972. Momentum, mass and heat exchange of vegetation. *Quarterly Journal of the Royal Meteorological Society* 98, 124-134.
- Thompson, R.S., 1993. Building amplification factors for sources near buildings: A wind-tunnel study. *Atmospheric Environment. Part A. General Topics* 27, 2313-2325.
- Tominaga, Y., Mochida, A., Yoshie, R., Kataoka, H., Nozu, T., Yoshikawa, M., Shirasawa, T., 2008. AIJ guidelines for practical applications of CFD to pedestrian wind environment around buildings. *Journal of Wind Engineering and Industrial Aerodynamics* 96, 1749-1761.
- Tong, Z., Wang, Y.J., Patel, M., Kinney, P., Chrillrud, S., Zhang, K.M., 2012. Modeling Spatial Variations of Black Carbon Particles in an Urban Highway-Building Environment. *Environmental Science & Technology* 46, 312-319.
- Tong, Z., Zhang, K.M., 2015. The near-source impacts of diesel backup generators in urban environments. *Atmospheric Environment* 109, 262-271.

- Tseng, Y.-H., Meneveau, C., Parlange, M.B., 2006. Modeling flow around bluff bodies and predicting urban dispersion using large eddy simulation. *Environmental Science & Technology* 40, 2653-2662.
- USEPA, 2004a. Summary and Analysis of Comments: Control of Emissions from Nonroad Diesel Engines. U.S. Environmental Protection Agency.
- USEPA, 2004b. User's guide for the AERMOD Meteorological Preprocessor (AERMET). U.S. Environmental Protection Agency.
- USEPA, 2006. AP-42, Compilation of Air Pollution Emission Factors. U.S. Environmental Protection Agency.
- USEPA, 2008. AERSURFACE User's Guide. U.S. Environmental Protection Agency.
- Vardoulakisa, S., Fisherb, B.E.A., Pericleous, K., Gonzalez-Flescac, N., 2003. Modelling air quality in street canyons: a review. *Atmospheric Environment* 37, 155-182.
- W. Kirchstetter, T., Harley, R.A., Kreisberg, N.M., Stolzenburg, M.R., Hering, S.V., 1999. On-road measurement of fine particle and nitrogen oxide emissions from light- and heavy-duty motor vehicles. *Atmospheric Environment* 33, 2955-2968.
- Wang, X., Westerdahl, D., Chen, L.C., Wu, Y., Hao, J., Pan, X., Guo, X., Zhang, K.M., 2009. Evaluating the air quality impacts of the 2008 Beijing Olympic Games: On-road emission factors and black carbon profiles. *Atmospheric Environment* 43, 4535-4543.
- Wang, X., Westerdahl, D., Hu, J., Wu, Y., Yin, H., Pan, X., Max Zhang, K., 2012a. On-road diesel vehicle emission factors for nitrogen oxides and black carbon in two Chinese cities. *Atmospheric Environment* 46, 45-55.
- Wang, Y., Hopke, P.K., Rattigan, O.V., Xia, X., Chalupa, D.C., Utell, M.J., 2011a. Characterization of Residential Wood Combustion Particles Using the Two-Wavelength Aethalometer. *Environmental Science & Technology* 45, 7387-7393.
- Wang, Y.J., DenBleyker, A., McDonald-Buller, E., Allen, D., Zhang, K.M., 2011b. Modeling the chemical evolution of nitrogen oxides near roadways. *Atmospheric Environment* 45, 43-52.
- Wang, Y.J., Nguyen, M.T., Steffens, J.T., Tong, Z., Wang, Y., Hopke, P.K., Zhang, K.M., 2013a. Modeling multi-scale aerosol dynamics and micro-environmental air quality near a large highway intersection using the CTAG model. *Science of The Total Environment* 443, 375-386.
- Wang, Y.J., Yang, B., Lipsky, E.M., Robinson, A.L., Zhang, K.M., 2012b. Analyses of Turbulent Flow Fields and Aerosol Dynamics of Diesel Engine Exhaust Inside Two

- Dilution Sampling Tunnels Using the CTAG Model. *Environmental Science & Technology* 47, 889-898.
- Wang, Y.J., Yang, B., Lipsky, E.M., Robinson, A.L., Zhang, K.M., 2013b. Analyses of Turbulent Flow Fields and Aerosol Dynamics of Diesel Engine Exhaust Inside Two Dilution Sampling Tunnels Using the CTAG Model. *Environmental Science & Technology* 47, 889-898.
- Wang, Y.J., Zhang, K.M., 2009a. Modeling Near-Road Air Quality Using a Computational Fluid Dynamics Model. *Environ.Sci.Technol* 43, 7778–7783.
- Wang, Y.J., Zhang, K.M., 2009b. Modeling Near-Road Air Quality Using a Computational Fluid Dynamics Model, CFD-VIT-RIT. *Environmental Science & Technology* 43, 7778-7783.
- Wang, Y.J., Zhang, K.M., 2011. Study of roadway air quality issues – Development of Cornell Turbulent Aerosol Dynamics and Gas Chemistry Model. *Atmospheric Environment*.
- Wang, Y.J., Zhang, K.M., 2012. Coupled turbulence and aerosol dynamics modeling of vehicle exhaust plumes using the CTAG model. *Atmospheric Environment* 59, 284-293.
- Watanabe, T., 2004. Large-eddy simulation of coherent turbulence structures associated with scalar ramps over plant canopies. *Boundary-Layer Meteorol* 112, 307-341.
- Watson, J.G.C., J. C.; and Chen, L.-W. A., 2005. Summary of organic and elemental carbon/black carbon analysis methods and intercomparisons. *Aerosol Air Qual. Res.* 5, 65-102.
- Westerdahl, D., Wang, X., Pan, X., Zhang, K.M., 2009. Characterization of on-road vehicle emission factors and microenvironmental air quality in Beijing, China. *Atmospheric Environment* 43, 697-705.
- Wilson, N.R., Shaw, R.H., 1977. A Higher Order Closure Model for Canopy Flow. *Journal of Applied Meteorology* 16, 1197-1205.
- Wood, C.R., Jarvl, L., 2012. Urban climate observations in Helsinki. *Magzine of the Finnish Air Pollution Society*.
- Wroblewska, M., 2011. Emergency Generators- 10 second starting ePower News.
- Xie, X., Chun-Ho, L., Dennis, Y., C., Leung, 2007. Impact of Building Facades and Ground Heating on Wind Flow and Pollutant Transport in Street Canyons. *Atmospheric Environment* 41, 9030-9049.

- Xie, Z.-T., Castro, I.P., 2009. Large-eddy simulation for flow and dispersion in urban streets. *Atmospheric Environment* 43, 2174-2185.
- Xie, Z.-T., Coceal, O., Castro, I., 2008. Large-Eddy Simulation of Flows over Random Urban-like Obstacles. *Boundary-Layer Meteorol* 129, 1-23.
- Xie, Z.-T., Hayden, P., Wood, C.R., 2013. Large-eddy simulation of approaching-flow stratification on dispersion over arrays of buildings. *Atmospheric Environment* 71, 64-74.
- Xie, Z., Castro, I., 2006. LES and RANS for Turbulent Flow over Arrays of Wall-Mounted Obstacles. *Flow Turbulence Combust* 76, 291-312.
- Yan, B., Kennedy, D., Miller, R.L., Cowin, J.P., Jung, K.-h., Perzanowski, M., Balletta, M., Perera, F.P., Kinney, P.L., Chillrud, S.N., Validating a nondestructive optical method for apportioning colored particulate matter into black carbon and additional components. *Atmospheric Environment* In Press, Corrected Proof.
- Zhang, K.M., Wexler, A.S., 2002. Modeling the number distributions of urban and regional aerosols: theoretical foundations. *Atmospheric Environment* 36, 1863-1874.
- Zhang, L., Gong, S., Padro, J., Barrie, L., 2001. A size-segregated particle dry deposition scheme for an atmospheric aerosol module. *Atmospheric Environment* 35, 549-560.
- Zhang, X., Zhang, K.M., 2015. Demand Response, Behind-the-Meter Generation and Air Quality. *Environmental Science & Technology* 49, 1260-1267.